

Do the planets cause the sunspot cycle?

Lauri Jetsu ¹••

© The author(s) ••••

Abstract The mainstream dynamo models predict that the sunspot cycle is stochastic. The official Solar Cycle Prediction Panel forecasts only the ongoing sunspot cycle because any forecast beyond one cycle is considered impossible. We analyse the sunspot data using our Discrete Chi-square Method (DCM). This method can detect many periodic signals superimposed on an arbitrary trend. The DCM detects the extremely significant strong 10, 11, and 11.86 years signals. The Discrete Fourier Transform (DFT) cross-check confirms that these signals are certainly real. Our deterministic DCM model predictions are more accurate and longer than the official Solar Cycle Prediction Panel forecast. The DCM models can predict the past prolonged activity minima, like the Maunder minimum, although we do not have data from these periods. Better long-term solar activity predictions can improve the models of climate change on Earth. Better short-term predictions can forewarn us of the catastrophic geomagnetic storms, like the Carrington event in the year 1859. We connect the detected signals to the orbital periods of Mercury, Venus, the Earth and Jupiter. If the planets cause the sunspot cycle, the exoplanets may cause the starspot cycles observed in other chromospherically active stars.

Keywords: Solar cycle, Observations - Solar cycle, Models - Sunspots, Statistics

1. Introduction

Schwabe (1844) discovered the 10 years cycle in the number of sunspots. Wolf (1852) revised the cycle period to 11.1 years. This period is not constant but varies between 8 and 17 years (Lassen and Friis-Christensen, 1995). The amplitude of the sunspot number modulation follows a cycle of about 80 years (Gleissberg, 1945). All solar cycles have not been discovered from the sunspots, like the $P_{\text{Rieger}} = 154$ days Rieger cycle discovered from the solar flares (Rieger et al., 1984) and the 205 years Suess-de Vries cycle discovered from the terrestrial radiocarbon ^{14}C record (Wagner et al., 2001). These observations indicate that the sunspot data are multiperiodic. Multiple periods have been detected in the sunspot data with different time series analysis methods (Ohtomo et al., 1994; Zhu and Jia, 2018; Jayalekshmi, Pant, and Prince, 2022). There is no “phase-lock” in the observed sunspot cycle minimum and the maximum epochs (Weisshaar, Cameron, and Schüssler, 2023; Biswas et al., 2023). Such a “phase-lock” would not exist, if the sunspot data were multiperiodic.

L. JETSU
lauri.jetsu@helsinki.fi

¹ Department of Physics, P.O. Box 64, FI-00014 University of Helsinki, Finland

Table 1. Recent prolonged periods of weak sunspot activity.

Minimum	Duration	Reference
Dalton	1790 - 1830	Komitov and Kaftan (2004)
Maunder	1640 - 1720	Usoskin, Solanki, and Kovaltsov (2007)
Spörer	1390 - 1550	Usoskin, Solanki, and Kovaltsov (2007)
Wolf	1270 - 1340	Usoskin, Solanki, and Kovaltsov (2007)
Oort	1010 - 1070	Usoskin, Solanki, and Kovaltsov (2007)

The solar surface magnetic field is strongest in the sunspots. The polarity of this field is reversed at the beginning of each solar cycle. Therefore, the field geometry returns to its original state during the Hale cycle of about 22 years (Hale et al., 1919). One persistent solar cycle regularity has been the Gnevyshev–Ohl rule: every odd numbered sunspot cycle has had a higher amplitude than the preceding even numbered sunspot cycle (Gnevyshev and Ohl, 1948).

There have been prolonged periods when very few sunspots, or even none at all, were observed. The four most recent prolonged grand sunspot minima were identified by Usoskin, Solanki, and Kovaltsov (2007), who did not classify the Dalton minimum (Komitov and Kaftan, 2004) as a grand sunspot minimum. We give the epochs of these five most recent prolonged activity minima in our Table 1. The Earth’s climate temperature rises during strong solar activity (e.g. Van Geel et al., 1999). Thus, the current prolonged solar activity minimum helps us to cope with the human-induced climate change.

Parker (1955) presented the dynamo model, where the solar magnetic field arises from interaction between internal differential rotation and convection. Babcock (1961) and Leighton (1969) presented the first models of how this dynamo may generate the sunspot cycle. In his review of the current dynamo models of the solar cycles, Charbonneau (2010) stated that all physical mechanisms causing the solar cycles are not yet fully understood. He noted that the physical processes regulating the magnetic amplitude of the solar cycle are still unknown. It is also not known how the sunspot-forming magnetic flux ropes are produced by the dynamo-generated mean magnetic field. Very recently, Vasil et al. (2024) proposed that the solar magnetic cycles are caused by a dynamo resulting from near-surface magneto-rotational instability.

The official sunspot number forecast for the ongoing solar cycle 25 was made in the year 2019 by the Solar Cycle Prediction Panel, representing NOAA, NASA and the International Space Environmental Services (ISES). These forecasts are made only for one cycle at the time, because it is widely accepted that this stochastic variability is unpredictable beyond one solar cycle (Petrovay, 2020). Nevertheless, countless sunspot cycle predictions are constantly published (e.g. Asikainen and Mantere, 2023; Javaraiah, 2023; Krasheninnikov and Chumakov, 2023). The physical models for solar cycle prediction were recently reviewed by Bhowmik et al. (2023).

Wolf (1859) already argued that the variations in the sunspot cycle period may depend on Jupiter, Saturn, the Earth and Venus. There have been numerous attempts to find the connection between the planetary motions and the sunspot numbers (e.g. Schuster, 1911; Hantzsch, 1978). Recently, Stefani, Giesecke, and Weier (2019) formulated a solar-dynamo model, where planetary tidal forcing causes the sunspot cycle. Scafetta and Bianchini (2022) showed that the planetary tidal forces may alter the solar structure and cause the sunspot cycle. Charbonneau (2022) argued that the weak periodic tidal interaction signal of planets requires constant amplification because internal solar dynamo mechanisms can otherwise mask this signal.

The problem with the deterministic “planetary-influence-theory” is that long-term sunspot cycle predictions fail. At the moment, in the year 2024, the “solar-dynamo-theory” of a stochastic sunspot cycle is mainstream, while the “planetary-influence-theory” of a deterministic sunspot

cycle is not. Here, we present successful deterministic sunspot number predictions, which are more accurate and extend over longer time intervals than the official Solar Cycle Prediction Panel forecast.

Section 2 describes the sunspot data. Section 3 introduces the Discrete Chi-square Method (DCM). Section 4 presents the results of our statistical DCM time series analysis of the sunspot data. We publish all details of this analysis in our DCM-manual.¹ Section 5 describes our Discrete Fourier Transform (DFT) cross-check for the DCM signal detections. We confirm that the DCM and the DFT detect the same extremely significant signals. Section 6 describes the predictability of sunspot data. We discuss our results in Section 7 and draw our conclusions in Section 8. The identification of integer multiples of planetary orbital periods is discussed in our Appendix.

2. Data

We retrieved the sunspot data from the Solar Influences Data Analysis Center² in December 2022. The monthly mean total sunspot number data begin in January 1749 and end to November 2022 (Table 2: $n = 3287$). After January 1818, the monthly mean standard deviation (S_i) of the input sunspot numbers from individual stations are available, as well as the total number of observations (N_i).

The yearly mean total sunspot number data begin in the year 1700 and end to 2021 (Table 3: $n = 322$). The S_i and N_i estimates are available after 1818.

The standard errors

$$\sigma_i = S_i / \sqrt{N_i} \quad (1)$$

for these data give the weights $w_i = \sigma_i^{-2}$. The normalised weights are

$$w_{\text{nor},i} = nw_i / \sum_{i=1}^n w_i. \quad (2)$$

If all errors were equal, the normalised weight $w_{\text{nor},i}$ for every observation would be one. For all monthly data, the normalised weights show that one observation out of $n = 2458$ observations has the largest weight $w_{\text{nor},\text{max}} = 381$ (Table 4, Line 1). The four most accurate, $N_{1/2} = 4$, observations influence the modeling more than the remaining $n - 4 = 2454$ observations. These monthly data statistics improve slightly if the more accurate data after the year 2000 are removed, which gives $N_{1/2} = 64$ for sample size $n = 2183$. All yearly data show an extreme case, $N_{1/2} = 1$, where the weight $w_{\text{nor},\text{max}} = 135$ of one observation exceeds the weight of all other $n - 1 = 203$ observations. Again, the statistics improve slightly if the more accurate data after the year 2000 are removed.

For these biased normalised weights, the period and the amplitude error estimates for the weighted data signals would be dramatically larger than the respective errors for the non-weighted data signals. For example, the bootstrap reshuffling (see Equation 25) of the four $N_{1/2} = 4$ most accurate monthly values, or the one $N_{1/2} = 1$ most accurate yearly value, resembles Russian roulette, where the majority of remaining other data values do not seem to need to fit to the model at all. We emphasise that the weighted data itself causes this bias, not our period analysis method.

¹All analysed data and the DCM Python code are available in <https://zenodo.org/uploads/11503698>. Our DCM-manual gives detailed instructions for repeating the whole DCM analysis.

²Source: WDC SILSO, Royal Observatory of Belgium, Brussels

Table 2. Times t_i of monthly mean total sunspot numbers y_i ($n = 3287$). The standard deviation (S_i) and the total number of estimates (N_i) are available from January 1818 onward. Values -1 indicate cases having no S_i and N_i estimate. This table shows only the first and the last lines, because all data is available in electronic form.

t_i (y)	y_i (-)	S_i (-)	N_i (-)
1749.042	96.7	-1	-1
...
2022.873	77.6	14.1	881

Table 3. Yearly mean total sunspot numbers ($n = 322$), otherwise as in Table 2

t_i (y)	y_i (-)	S_i (-)	N_i (-)
1700.5	8.3	-1	-1
...
2021.5	29.6	7.9	15233

Table 4. Normalised weights $w_{\text{nor},i}$ for Equation 2. (1) Sample. (2) Sample size. (3,4) Maximum and minimum $w_{\text{nor},i}$. (5) Number of largest $w_{\text{nor},i}$ having a sum exceeding $n/2$.

(1) Sample	(2) n (-)	(3) $w_{\text{nor},\text{max}}$ (-)	(4) $w_{\text{nor},\text{min}}$ (-)	(5) $N_{1/2}$ (-)
Monthly data				
All	2458	381	2.02×10^{-5}	4
Before 2000	2183	48.9	1.83×10^{-3}	64
Yearly data				
All	204	135	1.08×10^{-3}	1
Before 2000	182	21.6	1.11×10^{-2}	6

Table 5. Eight sunspot data samples. (1) Table from where sample is drawn. (2) Sample name. (3-4) Sample first and last observing time. (5) Sample time span. (6) Sample size. (7) Sample electronic file name.

(1) Table	(2) Name	(3) t_1 (y)	(4) t_n (y)	(5) ΔT (y)	(6) n (-)	(7) File
Table 2	Rmonthly	1749.0	2022.8	273.8	3287	Rmonthly.dat
Table 2	Rmonthly2000	1749.0	1999.9	250.9	3012	Rmonthly2000.dat
Table 2	Cmonthly	1818.0	2022.8	204.8	2458	Cmonthly.dat
Table 2	Cmonthly2000	1818.0	1999.9	181.9	2182	Cmonthly2000.dat
Table 3	Ryearly	1700.5	2021.5	321.0	322	Ryearly.dat
Table 3	Ryearly2000	1700.5	1999.5	299.0	300	Ryearly2000.dat
Table 3	Cyearly	1818.5	2021.5	203.0	204	Cyearly.dat
Table 3	Cyearly2000	1818.5	1995.5	181.0	182	Cyearly2000.dat

We solve this statistical bias of errors σ_i by using the Sigma-cutoff weights

$$\begin{cases} w'_i = 1, & \text{if } \sigma_i \leq K\bar{\sigma} \\ w'_i = (K\bar{\sigma}/\sigma_i)^x, & \text{if } \sigma_i > K\bar{\sigma}, \end{cases} \quad (3)$$

where $\bar{\sigma}$ is the mean of all σ_i , and the K and x values can be freely chosen (Handler, 2003; Breger et al., 2002). We use the same $K = 1$ and $x = 2$ values as Rodríguez et al. (2003), which gives

$$\begin{cases} \sigma'_i = 1, & \text{if } \sigma_i \leq \bar{\sigma} \\ \sigma'_i = \sigma_i/\bar{\sigma} > 1, & \text{if } \sigma_i > \bar{\sigma}. \end{cases} \quad (4)$$

Our chosen K and x values are reasonable, because they give 55 percent of monthly data having full weight 1, and 25 percent having weight below 1/2. The respective values for the yearly data are 53 and 24 percent.

There are four exceptional cases. We use the sigma cutoff weights $w'_i = 1$ for the three exceptional cases $y_i = 0$, $S_i = 0$ and $N_i > 0$, which solves the infinite weight $w_i = \sigma_i^{-2} = 0^{-2} = \infty$ problem. Finally, we compute no error estimate for the one exceptional case, $S_i > 0$ and $N_i = 0$.

We analyse eight samples. The first four samples are monthly sunspot data drawn from Table 2. The last four samples are yearly sunspot data drawn from Table 3. All eight samples are published only in electronic form. We summarise the sample contents and sample naming abbreviations in Table 5.

2.1. Rmonthly and Rmonthly2000

Rmonthly is our largest sample ($n = 3287$, $\Delta T = 274^y$). It contains all t_i and y_i values from Table 2. Since the error estimates σ_i are unknown before January 1818, we use an arbitrary error $\sigma_i = 1$ for all data in this sample. We perform a non-weighted period analysis, which is based on the sum of squared residuals (Equation 11: R). Hence, the chosen $\sigma_i = 1$ value has no effect to our analysis results, because every observation has an equal weight. The particular file name **Rmonthly** is used because the period analysis is based on a non-weighted R test statistic.

Rmonthly2000 contains observations from **Rmonthly**, which were made before the year 2000 ($n = 3012$, $\Delta T = 251^y$). Number “2000” refers to the omitted data after the year 2000.

2.2. Cmonthly and Cmonthly2000

Cmonthly contains all t_i and y_i observations having an error estimate σ'_i computed from Equation 4 ($n = 2458$, $\Delta T = 205^y$). For this sample, we apply the weighted period analysis, which utilises the error σ'_i information (Equation 12: χ^2). The sample name begins with letter “C”, because our analysis is based on the weighted Chi-square test statistic (Equation 18).

Cmonthly2000 contains those Cmonthly observations, which were made before the year 2000 ($n = 2182$, $\Delta T = 182^y$). We refer to the omitted data after the year 2000 by using the number “2000”.

2.3. Ryearly and Ryearly2000

Ryearly is our longest sample ($\Delta T = 321^y$) containing $n = 322$ yearly mean total sunspot number observations over more than three centuries. Since no error estimates are available for observations before 1818, the value $\sigma_i = 1$ is used for all data. We perform a non-weighted period analysis based on the R test statistic (Equation 11). Therefore, the sample name begins with the letter “R”.

Ryearly2000 contains observations from Ryearly that were made before the year 2000.

2.4. Cyearly and Cyearly2000

Cyearly is the smallest sample ($n = 204$, $\Delta T = 204^y$). It contains all yearly mean total sunspot numbers having an error estimate σ'_i (Equation 4). We perform a weighted period analysis based on the χ^2 test statistic (Equation 12). Therefore, the sample name begins with the letter “C”.

Cyearly2000 contains all Cyearly data before the year 2000.

3. Discrete Chi-Square Method (DCM)

In this section, we give a thorough description the Discrete Chi-Square Method (DCM), because this is essential for understanding the results of our sunspot data analysis. Jetsu (2020, Paper I) formulated this method. He used DCM to discover the periods of a third and a fourth body from the O-C data of the eclipsing binary XZ And. An improved DCM version revealed the presence of numerous new companion candidates in the eclipsing binary Algol (Jetsu, 2021, Paper II). DCM is designed for detecting many signals superimposed on an arbitrary trend.

The sunspot number data notations are observations $y_i = y(t_i) \pm \sigma_i$, where t_i are the observing times and σ_i are the errors ($i = 1, 2, \dots, n$). The units are $[y_i] = \text{dimensionless}$, $[\sigma_i] = \text{dimensionless}$ and $[t_i] = \text{years}$. The time span of data is $\Delta T = t_n - t_1$. The mid point is $t_{\text{mid}} = t_1 + \Delta T/2$. Our notations for the mean and the standard deviation of all y_i values are m and s , respectively.

DCM model

$$g(t) = g(t, K_1, K_2, K_3) = h(t) + p(t). \quad (5)$$

is a sum of a periodic function

$$h(t) = h(t, K_1, K_2) = \sum_{i=1}^{K_1} h_i(t) \quad (6)$$

$$h_i(t) = \sum_{j=1}^{K_2} B_{i,j} \cos(2\pi j f_i t) + C_{i,j} \sin(2\pi j f_i t), \quad (7)$$

and an aperiodic function

$$p(t) = p(t, K_3) = \begin{cases} 0, & \text{if } K_3 = -1 \\ \sum_{k=0}^{K_3} p_k(t), & \text{if } K_3 = 0, 1, 2, \dots \end{cases} \quad (8)$$

where

$$p_k(t) = M_k \left[\frac{2(t - t_{\text{mid}})}{\Delta T} \right]^k. \quad (9)$$

The periodic $h(t)$ function is a sum of K_1 harmonic $h_i(t)$ signals having frequencies f_i .

The signal order is K_2 . For simplicity, we refer to $K_2 = 1$ order models as “pure sine” models, and to $K_2 = 2$ order models as “double wave” models. The former category of signal curves are pure sines. The latter category of signal curves can deviate from a pure sine.

The $h_i(t)$ signals are superimposed on the aperiodic K_3 order polynomial trend $p(t)$. Function $h(t)$ repeats itself in time. Function $p(t)$ does not repeat itself, except when $p(t) = 0$ for $K_3 = -1$ or $p(t) = M_0 = \text{constant}$ for $K_3 = 0$.

DCM model residuals are

$$\epsilon_i = y(t_i) - g(t_i) = y_i - g_i. \quad (10)$$

Our notations for the mean and standard deviation of the residuals are m_ϵ and s_ϵ . The notations for the mean and maximum values of the absolute values of residuals are $|\epsilon|_{\text{mean}}$ and $|\epsilon|_{\text{max}}$. The residuals give the sum of squared residuals

$$R = \sum_{i=1}^n \epsilon_i^2, \quad (11)$$

and also the Chi-square

$$\chi^2 = \sum_{i=1}^n \frac{\epsilon_i^2}{\sigma_i^2}. \quad (12)$$

If the data errors σ_i are known, we use χ^2 to estimate the goodness of our model. For unknown errors σ_i , we use R .

Our notation for K_1 , K_2 and K_3 order DCM model $g(t)$ is “ $\mathcal{M}_{K_1, K_2, K_3, R}$ ” or “ $\mathcal{M}_{K_1, K_2, K_3, \chi^2}$ ”. The last subscripts “ R ” or “ χ^2 ” refer to the use of Equation 11 or 12 in estimating the goodness of our model, respectively.

The free parameters of model $g(t)$ are

$$\boldsymbol{\beta} = [\beta_1, \beta_2, \dots, \beta_\eta] = [B_{1,1}, C_{1,1}, f_1, \dots, B_{K_1, K_2}, C_{K_1, K_2}, f_{K_1}, M_0, \dots, M_{K_3}], \quad (13)$$

where

$$\eta = K_1 \times (2K_2 + 1) + K_3 + 1 \quad (14)$$

is the number of free parameters. We divide the free parameters $\boldsymbol{\beta}$ into two groups

$$\boldsymbol{\beta}_I = [f_1, \dots, f_{K_1}] \quad (15)$$

$$\boldsymbol{\beta}_{II} = [B_{1,1} C_{1,1}, \dots, B_{K_1, K_2}, C_{K_1, K_2}, M_0, \dots, M_{K_3}] \quad (16)$$

The first frequency group β_I makes the $g(t)$ model non-linear, because all free parameters are not eliminated from all partial derivatives $\partial g / \partial \beta_i$. If these β_I frequencies are fixed to the constant known tested numerical values, none of the partial derivatives $\partial g / \partial \beta_i$ contain any free parameters. In this case, the model becomes *linear*, and the solution for the second group of free parameters, β_{II} is *unambiguous*. Our concepts like “linear model” and “unambiguous result” refer to this type of models and their free parameter solutions.

For every tested frequency combination $\beta_I = [f_1, f_2, \dots, f_{K_1}]$, we compute the DCM test statistic

$$z = z(f_1, f_2, \dots, f_{K_1}) = \sqrt{R/n} \quad (17)$$

$$z = z(f_1, f_2, \dots, f_{K_1}) = \sqrt{\chi^2/n} \quad (18)$$

from a linear model least squares fit. We use Equation 17 or Equation 18, for unknown or known σ_i errors, respectively.

For two signal $K_1 = 2$ model, the sum $h(t)$ of signals $h_1(t)$ and $h_2(t)$ does not depend on the order in which these signals are added. This causes the symmetry $z(f_1, f_2) = z(f_2, f_1)$ for all tested frequency pairs f_1 and f_2 . The same symmetry applies to any other K_1 number of signals. Therefore, we compute z test statistic only for all combinations

$$f_{\max} \geq f_1 > f_2 > \dots > f_{K_1} \geq f_{\min}, \quad (19)$$

where f_{\min} and f_{\max} are the minimum and maximum tested frequencies, respectively. In the long search, we test an evenly spaced grid of n_L frequencies between f_{\min} and f_{\max} . This gives us the best frequency candidates $f_{1,\text{mid}}, \dots, f_{K_1,\text{mid}}$. In the short search, we test a denser grid of n_S frequencies within an interval

$$[f_{i,\text{mid}} - a, f_{i,\text{mid}} + a], \quad (20)$$

where $a = c(f_{\min} - f_{\max})/2$ and $i = 1, \dots, K_1$. In this study, we use $c = 0.05$ which means that the tested short search frequency interval represents 5% of the tested long search interval.

We search for periods between $P_{\min} = 1/f_{\max} = 5$ years and $P_{\max} = 1/f_{\min} = 200$ years. The reasons for not detecting periods below $P_{\min} = 5$ years are discussed in Appendix (Section A).

The best linear model for the data gives the global periodogram minimum

$$z_{\min} = z(f_{1,\text{best}}, f_{2,\text{best}}, \dots, f_{K_1,\text{best}}) \quad (21)$$

at the tested frequencies $f_{1,\text{best}}, f_{2,\text{best}}, \dots, f_{K_1,\text{best}}$.

The scalar z periodogram values are computed from K_1 frequency values. For example, $K_1 = 2$ two signal periodogram $z(f_1, f_2)$ could be plotted like a map, where f_1 and f_2 are the coordinates, and $z = z(f_1, f_2)$ is the height. For three or more signals, such a direct graphical presentation becomes impossible, because it requires more than three dimensions. We solve this problem by presenting only the following one-dimensional slices of the full periodogram

$$\begin{aligned} z_1(f_1) &= z(f_1, f_{2,\text{best}}, \dots, f_{K_1,\text{best}}) \\ z_2(f_2) &= z(f_{1,\text{best}}, f_2, f_{3,\text{best}}, \dots, f_{K_1,\text{best}}) \\ z_3(f_3) &= z(f_{1,\text{best}}, f_{2,\text{best}}, f_3, f_{4,\text{best}}, \dots, f_{K_1,\text{best}}) \\ z_4(f_4) &= z(f_{1,\text{best}}, f_{2,\text{best}}, f_{3,\text{best}}, f_4, f_{5,\text{best}}, f_{K_1,\text{best}}) \\ z_5(f_5) &= z(f_{1,\text{best}}, f_{2,\text{best}}, f_{3,\text{best}}, f_{4,\text{best}}, f_5, f_{K_1,\text{best}}) \\ z_6(f_6) &= z(f_{1,\text{best}}, f_{2,\text{best}}, f_{3,\text{best}}, f_{4,\text{best}}, f_{5,\text{best}}, f_6). \end{aligned} \quad (22)$$

Using the above $K_1 = 2$ map analogy, the slice $z_1(f_1)$ represents the height z at a f_1 coordinate when moving along the constant line $f_2 = f_{2,\text{best}}$ that crosses the global minimum z_{\min} (Equation 21) at the coordinate point $(f_{1,\text{best}}, f_{2,\text{best}})$.

The best frequencies detected in the short search give the initial values for the first group of free parameters $\beta_{\text{I,initial}} = [f_{1,\text{best}}, \dots, f_{K_1,\text{best}}]$ (Equation 15). The linear model with these constant $[f_{1,\text{best}}, \dots, f_{K_1,\text{best}}]$ frequency values gives the unambiguous initial values for the second group $\beta_{\text{II,initial}}$ of free parameters (Equation 16). The final non-linear iteration is performed from

$$\beta_{\text{initial}} = [\beta_{\text{I,initial}}, \beta_{\text{II,initial}}] \rightarrow \beta_{\text{final}}. \quad (23)$$

DCM determines the following parameters for $h_i(t)$ signals

- $P_i = 1/f_i$ = Period
- A_i = Peak to peak amplitude
- $t_{i,\min,1}$ = Deeper primary minimum epoch
- $t_{i,\min,2}$ = Secondary minimum epoch (if present)
- $t_{i,\max,1}$ = Higher primary maximum epoch
- $t_{i,\max,2}$ = Secondary maximum epoch (if present),

as well the M_k parameters of the $p(t)$ trend. For the sunspots, the most interesting parameters are the signal periods P_i , the signal amplitudes A_i , and signal primary minimum epochs $t_{\min,1}$ (DCM-manual: Tables 6-17).

The subtraction

$$y_{i,j} = y_i - [g(t_i) - h_j(t_i)] \quad (24)$$

shows how well all observations y_i are connected to any signal $h_j(t)$, where $j = 1, \dots, K_1$. In other words, the full model $g(t_i)$ is subtracted from the data y_i , except for the $h_j(t_i)$ signal itself. We show an example of this subtraction in our DCM-manual (Figure 3: right-hand panels). This subtraction resembles the Discrete Fourier Transform de-trending procedure (e.g. Murphy, 2012), but here we remove both the trend and all other signals, except for the $h_j(t_i)$ signal.

The DCM model parameter errors are determined with the bootstrap procedure (Efron and Tibshirani, 1986). We have previously used this same bootstrap procedure in our TSPA- and CPS-methods (Jetsu and Pelt, 1999; Lehtinen et al., 2011). A random sample ϵ^* is selected from the residuals ϵ of the DCM model (Equation 10). In this reshuffling of ϵ_i residuals, any ϵ_i can be chosen as many times as the random selection happens to favour it. This random sample of residuals gives the *artificial* bootstrap data sample

$$y_i^* = g_i + \epsilon_i^*. \quad (25)$$

We create numerous such \mathbf{y}^* random samples. The DCM model for each \mathbf{y}^* sample gives one estimate for every model parameter. The error estimate for each particular model parameter is the standard deviation of all estimates obtained from all \mathbf{y}^* bootstrap samples.

DCM models are nested. For example, a one signal model is a special case of a two signal model. DCM uses the Fisher-test to compare any pair of simple $g_1(t)$ and complex $g_2(t)$ models. Their number of free parameters are $\eta_1 < \eta_2$. Their sums of squared residuals (R_1, R_2) and Chi-squares (χ_1, χ_2) give the Fisher-test test statistic

$$F_R = \left(\frac{R_1}{R_2} - 1 \right) \left(\frac{n - \eta_2 - 1}{\eta_2 - \eta_1} \right) \quad (26)$$

$$F_\chi = \left(\frac{\chi_1^2}{\chi_2^2} - 1 \right) \left(\frac{n - \eta_2 - 1}{\eta_2 - \eta_1} \right). \quad (27)$$

The Fisher-test null hypothesis is

H_0 : “The complex model $g_2(t)$ does not provide a significantly better fit to the data than the simple model $g_1(t)$.”

Under H_0 , both test statistic parameters F_R and F_χ have an F distribution with (ν_1, ν_2) degrees of freedom, where $\nu_1 = \eta_2 - \eta_1$ and $\nu_2 = n - \eta_2$ (Draper and Smith, 1998). The probability for F_R or F_χ reaching values higher than F is called the critical level $Q_F = P(F_R \geq F)$ or $Q_F = P(F_\chi \geq F)$. We reject the H_0 hypothesis, if

$$Q_F < \gamma_F = 0.001, \quad (28)$$

where γ_F is the pre-assigned significance level. This γ_F represents the probability of falsely rejecting H_0 hypothesis when it is in fact true. If H_0 is rejected, we rate the complex $g_2(t)$ model better than the simple $g_1(t)$ model.

The basic idea of the Fisher-test is simple. The H_0 hypothesis rejection probability increases for larger F_R values having smaller Q_F critical levels. The complex model R_2 or χ^2_2 values decrease when the η_2 number of free parameters increases. This increases the first $(R_1/R_2 - 1)$ and $(\chi^2_1/\chi^2_2 - 1)$ terms in Equations 26 and 27. However, the second $(n - \eta_2 - 1)/(\eta_2 - \eta_1)$ penalty term decreases at the same time. This second penalty term prevents over-fitting, i.e. accepting complex models having too many η_2 free parameters.

The key ideas of DCM are based on the following robust, thoroughly tested statistical approaches

1. The DCM model $g(t)$ is *non-linear* (Equation 5). This model becomes *linear* when the frequencies $\beta_I = [f_1, \dots, f_{K_1}]$ (Equation 15) are fixed to their tested numerical values. This linear model gives *unambiguous* results for the other free parameters, β_{II} (Equation 16).
2. The short search $f_{1,\text{best}} > f_{2,\text{best}} > \dots > f_{K_1,\text{best}}$ grid combination that minimises the z test statistic gives the best initial β_{initial} values for the non-linear iteration of Equation 23.
3. DCM tests a dense grid of all possible frequency combinations $f_{\max} \geq f_1 > f_2 > \dots > f_{K_1} \geq f_{\min}$ (Equation 19). For every frequency combination, the *unambiguous linear* model least squares fit gives the test statistic $z = \sqrt{\chi^2/n}$ (errors σ_i known) or $z = \sqrt{R/n}$ (errors σ_i unknown).
4. All model parameter error estimates are determined with the bootstrap method (Equation 25).
5. The best model is identified using the Fisher-test, which compares all different tested K_1 , K_2 and K_3 order combinations for nested models (Draper and Smith, 1998; Allen, 2004).

DCM has the following restrictions

1. If the frequency grid $f_1 > f_2 > \dots > f_{K_1}$ contains n_L values in the long search, then the total number of all tested frequency combinations is

$$\binom{n_L}{K_1} = \frac{n_L!}{K_1!(n_L - K_1)!}. \quad (29)$$

For example, it took about two days for a cluster of processors to compute the four signal DCM model for the `Rmonthly2000` sample (DCM-manual: Figures 1-4).

2. An adequately dense tested frequency grid eliminates the possibility that the best frequency combination is missed. The restriction is that denser grids require more computation time. If the tested frequency grid is sufficiently dense, no abrupt periodogram jumps occur, because the z values for all close tested frequencies correlate. Hence, the frequencies of the minima of these periodograms are accurately determined. There is no need to test an even denser grid, because this would not alter the final result of the non-linear iteration of Equation 23.

3. Some DCM models are unstable. They are simply wrong models for the data, like a wrong $p(t)$ trend order K_3 or a search for too few or too many K_1 signals (e.g., Paper I: Figures 5-10). This causes model instability. We denote such unstable models with “UM” (DCM-manual: Tables 6-17). The signatures of such unstable models are

“IF” = Intersecting frequencies
 “AD” = Dispersing amplitudes
 “LP” = Leaking periods

Intersecting frequencies “IF” occur when the frequencies of two signals are very close to each other. For example, if frequency f_1 approaches frequency f_2 , the $h_1(t)$ and $h_2(t)$ signals become essentially one and the same signal. This ruins the least squares fit. It makes no sense to add the same signal twice.

Dispersing amplitudes “AD” also occur when two signal frequencies are close to each other, like in the above-mentioned “IF” cases. The least squares fit uses two high amplitude signals which cancel out. Hence, the sum of these two high amplitude signals is one low amplitude signal that fits to the data.

We take extra care to identify the suspected “IF” and ”AD” unstable model cases. The reshuffling of bootstrap ϵ^* residuals provides a good test for identifying such unstable models from the DCM analysis of numerous artificial bootstrap data samples \mathbf{y}^* (Equation 25). If we encounter any signs of instability, we test combinations $n_L = 100 \& c = 0.05$, $n_L = 100 \& c = 0.10$, $n_L = 120 \& c = 0.05$ and $n_L = 120 \& c = 0.10$. If there is instability in any of these combinations, we reject the model as unstable (“UM”). If there is no instability, we take the n_L and c combination that gives the lowest value for R (non-weighted data) or χ^2 (weighted data).

Leaking periods “LP” instability refers to the cases, where the detected frequency f is outside the tested frequency interval between f_{\min} and f_{\max} , or the period $P = 1/f$ of this frequency is longer than the time span ΔT of the data.

We use the DCM model $g(t_i, \beta)$ to predict the future and past data. The three samples used in these predictions are the predictive data, the predicted data and all data. We use the following notations for the time points, the observations and the errors of these three samples.

- Predictive data: n values of t_i , y_i and σ_i
- Predicted data: n' values of t'_i , y'_i and σ'_i
- All data: $n'' = n + n'$ values of t''_i , y''_i and σ''_i from predictive and predicted data

We also compute the monthly or yearly time points during past activity minima of Table 1. Our notations for these time points are

- Activity minimum data: n''' values of t'''_i

DCM gives the best free parameter β values for the predictive data model $g_i = g(t_i, \beta)$, where the “old” t_{mid} and ΔT values are computed from the predictive data time points t_i . These “old” predictive data t_{mid} and ΔT values are used to compute the predicted data model values

$$g'_i = g(t'_i, \beta)$$

In other words, we do not compute “new” t_{mid} and ΔT values from the predicted data time points t'_i . There is an obvious reason for this. The predictive data free parameter values β give the correct g'_i values only for the “old” predictive data t_{mid} and ΔT values. The residuals

$$\epsilon'_i = y'_i - g'_i$$

of the predicted data give the *predicted test statistic*

$$z_{\text{pred}} = z \text{ test statistic for predicted data (Equation 17 or 18),} \quad (30)$$

which measures how well the prediction obtained from the predictive data works.

The best DCM model $g(t_i'', \beta)$ for all data uses the “old” t_{mid} and ΔT values computed from t_i'' time points of all data. We use these “old” t_{mid} and ΔT values to compute the predicted model values

$$g_i''' = g(t_i'', \beta) \quad (31)$$

for the monthly or yearly time points t_i''' during the chosen activity minimum of Table 1. These g_i''' values give the *predicted mean level*

$$m_{\text{pred}} = \frac{1}{n'''} \sum_{i=1}^{n'''} g_i''' \quad (32)$$

during the selected activity minimum of Table 1.

It is essential to understand how and why the above two predictive parameters of Equations 30 and 32 are computed. The former parameter, z_{pred} , is computed from the *known* t_i' , y_i' and σ_i' values of the predicted data. If our predictions are correct, the following regularities should occur

- z_{pred} decreases, if DCM detects real new signals in the predictive data
- z_{pred} increases, if DCM detects unreal new signals in the predictive data

For the latter m_{pred} parameter, the t_i''', y_i''' or σ_i''' data values during the past activity minima are *unknown*, but we can create the n''' monthly or yearly t_i''' time points during these minima of Table 1. We can then compute the g_i''' values from these t_i''' values (Equation 31). This gives us the mean m_{pred} value (Equation 32) that can be compared to the mean level m for all data. If our predictions for the past activity minima of Table 1 are correct, the following regularities should occur

- m_{pred} falls below m , if DCM detects real new signals in all data
- m_{pred} decreases, if DCM detects real new signals in all data
- m_{pred} increases, if DCM detects unreal new signals in all data

Our model is non-linear (Equations 5 - 9). We find a unique solution for this ill-posed problem. The stages of finding this solution are

1. We fix the numerical values of the tested frequencies β_I (Equation 15). The model becomes linear and the solution for the other free parameters β_{II} is unique (Equation 16).
2. We test all possible β_I frequency combinations (Equation 19). The linear model for every tested frequency combination β_I gives a unique value for the test statistic z (Equations 17 and 18). We select the best frequency combination $\beta_{I,\text{best}}$ that minimises z . The model for this best frequency combination is unique and the free parameter values $\beta_{\text{initial}} = [\beta_{I,\text{best}}, \beta_{II,\text{best}}]$ of this model are unique.
3. These unique initial free parameter values β_{initial} are used in the non-linear iteration (Equation 23) that gives the unique final free parameter values β_{final} . This solution is unique.
4. We use the Fisher-test to compare many different non-linear models against each other. The selection criterion for the best model is unique (Equation 28).

After the selection of the tested non-linear models, these four stages give a unique the solution for this ill-posed problem.

4. DCM period detections

4.1. Periods between 5 and 200 years

We must introduce the “double sinusoid” concept before comparing the consistency of our DCM period detections in different samples. The shape of these double sinusoid signals resembles that of a pure sinusoid (Figures 1a-g). All seven double sinusoids are highlighted with the notation “ $2\times$ ” in Table 6. For example, we detect only one signal for the double wave $K_2 = 2$ model of **Cmonthly** sample (Table 6: Column 9, Figure 1a). The period of this signal is $P = 21.667 \pm 0.014 = 2 \times (10.834 \pm 0.007)$ years. The period of this double sinusoid signal is about two times longer than the ~ 11 years signal periods detected in all other eleven samples. In other words, including the **Cmonthly** sample, DCM detects this same ~ 11 years signal in all twelve samples.

We analyse twelve samples³ and detect only nine signals in the period range between 5 and 200 years (DCM-manual: Tables 6-17). This leaves very little room for inconsistency. The periods and the amplitudes of the nine signals are summarised in Table 6, where we introduce the following signal abbreviations S_{11y} , S_{10y} , $S_{11.y86}$, S_{110y} , $S_{10.y6}$, $S_{8.y4}$, S_{53y} , S_{8y} and S_{66y} . The numerical values in the subscripts of our signal abbreviations refer to the signal period in Earth years. These signals are arranged into the order of decreasing strength, or equivalently, of decreasing amplitude. We use the signal ranking based on the signal amplitudes in the first analysed sample (Table 6: **Rmonthly2000**), because this order for signal amplitudes varies slightly in different samples. For each particular sample, we give the exact signal ranking order in Table 6. Our DCM detects the same signals for

- Monthly and yearly data
- Non-weighted and weighted data
- Pure sine and double wave models
- All data samples and their subsets: predictive data samples

The S_{11y} signal is detected first in every sample. The critical levels for the all other signal detections⁴ are $Q_F < 10^{-16}$ (DCM-manual: Tables 6-17). Therefore, all DCM signal detections are extremely significant, unless the S_{11y} signal itself is an artefact. The two strongest detected signals in all samples are the S_{11y} and S_{10y} signals, and always in this order.

4.2. Periods between 0.1 and 5 years

The orbital and synodic periods of inner planets are shorter than 5 years. We can not search for these short periods in the yearly sunspot data, because their numerical values are close to, or below, the one-year window period. However, the monthly sunspot data can be used to search for these shorter planetary periods. Our DCM analysis in the period range between 0.1 and 5 years reveals no signs of these inner planet orbital or synodic periods (DCM-manual: Section 4.2.).

³All analysed data and the DCM Python code are available in <https://zenodo.org/uploads/11503698>. Our DCM-manual gives detailed instructions for repeating the whole DCM analysis.

⁴The highest achievable accuracy for the computational f.cdf subroutine in `scipy.optimize` python library is 10^{-16} .

Table 6.: Signals in monthly and yearly sunspot numbers. (1) Signal abbreviation. (2) Rmonthly2000 sample results for pure sines (DCM-manual: Table 6). All six detected signals are given in order of decreasing peak to peak amplitude A . (3-13) Results for other samples with chosen K_2 values. Double sinusoid signals are denoted with “ $\times 2$ ”. Notes below give an example of how to read this table.

	(1)	(2)	(3)	(4)	(5)	(6)	(7)	(8)	(9)	(10)	(11)	(12)	(13)
Signal	Rmonthly2000	Rmonthly	Rmonthly2000	Rmonthly	Monthly2000	Monthly	Monthly	Monthly	Ryearly2000	Ryearly	Cyearly2000	Cyearly	
	$K_2 = 1$	$K_2 = 1$	$K_2 = 1$	$K_2 = 2$	$K_2 = 1$	$K_2 = 1$	$K_2 = 2$	$K_2 = 2$	$K_2 = 1$	$K_2 = 1$	$K_2 = 1$	$K_2 = 1$	
	Rank (-)	Rank (-)	Rank (-)	Rank (-)	Rank (-)	Rank (-)	Rank (-)	Rank (-)	Rank (-)	Rank (-)	Rank (-)	Rank (-)	
	$P(y)$	$P(y)$	$P(y)$	$P(y)$	$P(y)$	$P(y)$	$P(y)$	$P(y)$	$P(y)$	$P(y)$	$P(y)$	$P(y)$	
	$A(-)$	$A(-)$	$A(-)$	$A(-)$	$A(-)$	$A(-)$	$A(-)$	$A(-)$	$A(-)$	$A(-)$	$A(-)$	$A(-)$	
S_{11y}	(1) 11.0324±0.0048	(1) 11.0033±0.0064	(1) 11.0234±0.0068	(1) 10.9878±0.0051	(1) 10.8054±0.013	(1) 10.8585±0.0048	(1) 10.8074±0.012	(1) 21.6674±0.014 $\times 2$	(1) 11.0064±0.017	(1) 10.9814±0.020	(1) 10.8134±0.029	(1) 10.8634±0.022	
	98.8±2.6	101.5±2.5	102.9±2.7	104.6±2.3	118.2±3.7	117.5±2.9	123.5±3.0	132.6±3.4	90.4±4.7	98.3±7.8	119.2±8.5	119.3±7.5	
S_{10y}	(2) 9.9842±0.0075	(2) 10.0001±0.0081	(2) 9.9882±0.0061	(2) 20.0062±0.0088 $\times 2$	(2) 10.1964±0.027	(2) 10.0658±0.0077	(2) 10.1964±0.017	(2) 9.9804±0.016	(2) 9.9754±0.017	(2) 10.1844±0.064	(2) 10.0584±0.026		
	77.4±2.2	65.5±2.1	78.6±2.6	75.2±2.7	61.9±3.9	59.3±2.8	62.1±3.7	64.6±7.6	62.8±6.1	62.3±6.8	61.0±9.6		
	(3) 11.8464±0.012	(3) 11.8074±0.012	(3) 23.6864±0.0182 \times	(3) 11.7704±0.011	(3) 11.8634±0.021	(3) 11.8624±0.034	(3) 11.8204±0.027	(3) 11.8624±0.034	(3) 11.8204±0.027	(3) 11.8564±0.068	(3) 11.8564±0.068		
	60.0±2.2	56.4±2.4	69.4±2.7	62.7±2.6	43.3±2.0	42.6±4.1	40.5±3.3					43.8±7.9	
S_{11oy}	(4) 96.2±1.0	(4) 99.9±2.0	(4) 104.16±0.59	(4) 104.23±0.68	(4) 116.7±1.3	(4) 100.3±2.1	(4) 101.4±2.4	(4) 100.3±2.1	(4) 101.4±2.4	(4) 115.6±3.6	(4) 115.6±3.6		
	50.1±2.8	51.8±2.3	70.4±3.6	68.1±2.7	52.9±2.5	52.4±6.3	51.7±4.9					53.8±5.2	
$S_{10,y6}$	(5) 10.5414±0.014	(5) 10.5694±0.020	(5) 10.5372±0.0075	(5) 10.5407±0.0060	(5) 10.6204±0.033	(5) 10.6594±0.031	(5) 10.6204±0.033	(5) 10.6594±0.031	(5) 10.6204±0.033	(5) 10.6594±0.031	(5) 10.6204±0.033	(5) 10.6594±0.031	
	45.0±1.8	51.0±1.8	51.2±1.8	55.6±2.3									
$S_{8,y4}$	(6) 16.7814±0.0342 \times	(6) 16.7534±0.0272 \times	(6) 44.9±4.0	(6) 41.2±3.1	(7) 8.4604±0.027	(7) 8.4664±0.016	(7) 33.0±4.4	(7) 31.1±4.8	(7) 33.0±4.4	(7) 31.1±4.8	(7) 33.0±4.4	(7) 31.1±4.8	
	52.6±0.27	33.9±2.0			(6) 53.24±0.78	(6) 53.83±0.76	(6) 35.3±6.3	(6) 34.3±3.6	(6) 35.3±6.3	(6) 34.3±3.6	(6) 35.3±6.3	(6) 34.3±3.6	
S_{53y}	(6) 8.1054±0.0084	(7) 8.1087±0.0076	(8) 8.1730±0.011	(8) 8.1694±0.014	(5) 8.0094±0.017	(5) 8.0054±0.058	(5) 8.0054±0.058						
	36.5±1.7	33.6±1.6	37.6±4.8	35.5±3.3	25.6±2.5	24.0±7.0							
S_{66y}	(7) 136.43±0.992 \times	(7) 143.39±0.992 \times	(7) 42.3±2.2	(7) 37.3±2.7	(8) 65.4±1.3	(8) 66.7±1.4	(8) 29.0±4.7	(8) 26.7±4.4	(8) 29.0±4.7	(8) 26.7±4.4	(8) 29.0±4.7	(8) 26.7±4.4	

Notes. For example, signal S_{11y} is detected in sample Rmonthly2000 (Column 2). Rank=“(1)” means that this S_{11y} signal is strongest of all six signals (DCM-manual: Table 6). Signal S_{11y} has period $P = 11.0324 \pm 0.0048$ and peak to peak amplitude $A = 98.8 \pm 2.6$.

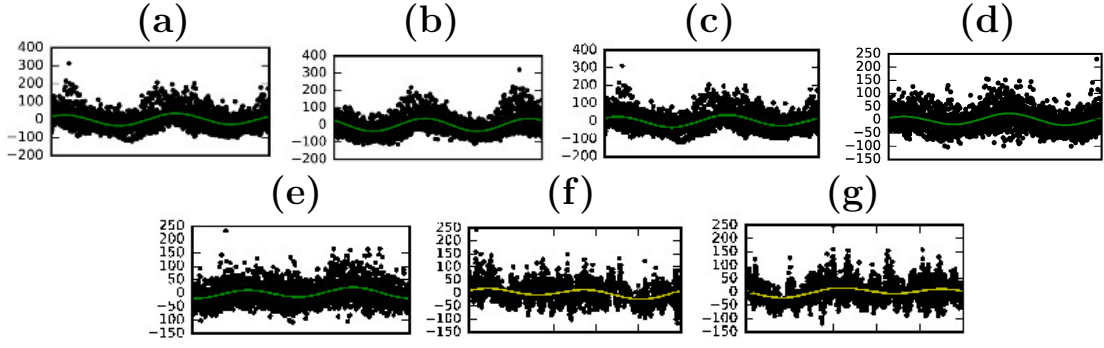


Figure 1. Double sinusoids $^{2\times}$ (Table 6). (a) $\text{C}_{\text{monthly}}$: S_{11y} signal period $21.667 \pm 0.014 = 2 \times (10.834 \pm 0.007)$. (b) $\text{R}_{\text{monthly}}$: S_{10y} signal period $20.0062 \pm 0.0088 = 2 \times (10.0031 \pm 0.0044)$. (c) $\text{R}_{\text{monthly2000}}$: $S_{11,y86}$ signal period $23.686 \pm 0.018 = 2 \times (11.843 \pm 0.009)$. (d) $\text{R}_{\text{monthly2000}}$: $S_{8,y4}$ signal period $16.781 \pm 0.034 = 2 \times (8.390 \pm 0.017)$. (e) $\text{R}_{\text{monthly}}$: $S_{8,y4}$ signal period $16.753 \pm 0.027 = 2 \times (8.376 \pm 0.014)$. (f) $\text{R}_{\text{monthly2000}}$: S_{66y} signal period $136.43 \pm 0.99 = 2 \times (68.22 \pm 0.50)$. (g) $\text{R}_{\text{monthly}}$: S_{66y} signal period $143.39 \pm 0.99 = 2 \times (71.70 \pm 0.50)$. Numbers and labels for x-axis phases ϕ between 0 and 1 are missing, because these figures are extracts from larger figures, like Figure 3 in the DCM-manual. Period units are years. Figure units are x-axis $[\phi]$ = dimensionless and y-axis $[y]$ = dimensionless.

5. Discrete Fourier Transform (DFT) cross-check

Zhu and Jia (2018) applied the Discrete Fourier Transform (DFT) to the daily sunspot number data from WDC SILSO (Royal Observatory of Belgium, Brussels). They used the DFT version formulated by Horne and Baliunas (1986). DFT searches for the best pure sine model for the data. Here, we cross-check if a similar DFT analysis of our monthly sunspot number sample $\text{R}_{\text{monthly}}$ gives the same results as our pure sine model DCM analysis (Table 6: Column 3). Before our cross-check, we perform DCM and DFT analysis of simulated data.

5.1. DFT detection of two pure sine signals

In these simulations, we compare the performance of DFT and DCM. Let us assume that the data contains the sum signal $s(t) = s_1(t) + s_2(t)$ of two pure sine signals

$$s_1(t) = a_1 \sin(2\pi f_1 t) \quad (33)$$

$$s_2(t) = a_2 \sin(2\pi f_2 t), \quad (34)$$

where the frequencies fulfil $f_1 \approx f_2$. DFT can detect both of the $s_1(t)$ and $s_2(t)$ signals, if

$$\Delta f = |f_2 - f_1| \gtrsim f_0, \quad (35)$$

where $f_0 = 1/\Delta T$ is the distance between independent frequencies (Loumos and Deeming, 1978). We give the $f/f_0 = \Delta T/P$ ratios for the S_{11y} , S_{10y} , $S_{10,y6}$ and $S_{11,y86}$ signals in Table 7. The S_{10y} and $S_{10,y6}$ signal frequencies fulfil the criterion of Equation 35 only in the two longest R_{yearly} and $\text{R}_{\text{yearly2000}}$ samples. This criterion is not fulfilled in our DFT cross-check $\text{R}_{\text{monthly}}$ sample (Table 7). Furthermore, many pairs of S_{11y} , S_{10y} , $S_{10,y6}$ and $S_{11,y86}$ signals detected in this sample $\text{R}_{\text{monthly}}$ have frequency differences Δf close to $1 \times f_0$.

The interference pattern of the sum $s(t)$ of the two signals $s_1(t)$ and $s_2(t)$ is repeated during the beat period $P_{\text{beat}} = |P_1^{-1} - P_2^{-1}|^{-1} = |f_1 - f_2|^{-1}$. The solutions for the frequency, the amplitude and the phase of this sum signal $s(t)$ are quite complex (Feth, 1974; Aguilar et al., 2012; Rutkowski, 2014; Schwär, Müller, and Schlecht, 2023). For the purposes of our DFT cross-check, it suffices to discuss the frequency $f(t)$ and the phase ϕ changes of the sum signal $s(t)$.

Table 7. Independent frequency limitation (Equation 35). Ratios $f/f_0 = \Delta T/P$ in order of decreasing sample time interval ΔT . Arrows above numerical values indicate cases where $\Delta f < f_0$.

Sample	ΔT (y)	S_{10y} $\Delta T/P$ (-)	$S_{10,y6}$ $\Delta T/P$ (-)	S_{11y} $\Delta T/P$ (-)	$S_{11,y86}$ $\Delta T/P$ (-)
Ryearly	321.0	32.10	30.28	29.18	27.07
Ryearly2000	299.0	29.90	28.21	27.18	25.21
Rmonthly	273.8	27.38	25.83	24.89	23.09
Rmonthly2000	250.9	25.09	23.67	22.81	21.16
Cmonthly	204.8	20.48	19.32	18.62	17.27
Cyearly	203.0	20.30	19.15	18.45	17.12
Cmonthly2000	181.9	18.19	17.16	16.54	15.34
Cyearly2000	181.0	18.10	17.07	16.45	15.25

The frequency $f(t)$ of the $s(t)$ sum signal is constant

$$f(t) = (f_1 + f_2)/2, \text{ if } a_1 = a_2. \quad (36)$$

This frequency $f(t)$ varies between the lower and upper limits given below

$$f_2 - \frac{a_1(f_1 - f_2)}{a_2 + a_1} \leq f(t) \leq f_2 + \frac{a_1(f_1 - f_2)}{a_2 + a_1}, \text{ if } a_2 > a_1. \quad (37)$$

In this case, the $f(t)$ frequency changes are dominated by the stronger f_2 signal.

The sum signal $s(t)$ amplitude a_s is constantly changing. An abrupt instantaneous phase shift

$$\Delta\phi = [\arcsin(a_1/a_2)]/\pi \quad (38)$$

occurs at the epoch of a_s amplitude minimum. This abrupt phase shift is the largest, $\Delta\phi = 0.5$, for equal amplitudes $a_1 = a_2$.

The limitation of Equation 35 can *prevent* the DFT detection of both f_1 and f_2 values. The effects of Equations 36, 37 and 38 can *mislead* the DFT detection of the correct f_1 and f_2 values.

The units of time intervals and periods in all our simulations are years. The amplitude unit is dimensionless. These units are therefore no longer mentioned in the simulations below. We simulate y_i^* data, where the monthly sunspot number time points t_i^* are computed for four alternative time intervals of $\Delta T = 70, 90, 110$ and 274 . These time intervals begin from the year 1749 at the beginning of sample Rmonthly. The longest $\Delta T = 274$ simulation has the same time span and the same time points as Rmonthly. The $s_1(t_i^*)$ and $s_2(t_i^*)$ signal periods are $P_1 = 1/f_1 = 10$, $P_2 = 1/f_2 = 11$. They are equal to the periods of the two strongest S_{10y} and S_{11y} signals detected in sample Rmonthly. This gives the beat period $P_{\text{beat}} = 110$. We simulate data for two alternative amplitude combinations $a_1 = a_2 = 50 \Rightarrow f(t) = \text{constant}$ (Equation 36) and $a_1 = 25 < a_2 = 50 \Rightarrow f(t) = \text{variable}$ (Equation 37). Hence, the total number of simulated samples is $4 \times 2 = 8$. The tested period interval between 5 and 200 years is the same as in our earlier DCM analysis of Rmonthly sample.

For the Rmonthly sample, the DCM five pure sine signal $\mathcal{M}=5$ model gives the residuals ϵ_i , which have a standard deviation $s_\epsilon = 42$. We assume that after the detection of these five pure

sine signals, these remaining ϵ_i residuals represent the noise in the original data. Therefore, the errors σ_i^* for the simulated data are drawn from a Gaussian distribution having a mean $m = 0$ and a standard deviation $s = s_\epsilon = 42$. The simulated data are

$$y_i^* = m^* + s_1(t_i^*) + s_2(t_i^*) + \sigma_i^*, \quad (39)$$

where $m^* = 81.6$ is the mean of all y_i values in `Rmonthly`. The selected m^* value has no impact on our results, because it is subtracted from the simulated y_i^* data before the computation of DFT periodogram. The DCM two sine wave model $\mathcal{M}_{2,1,0,R}$ solves this $M_0 = m^*$ value.

We analyse the $2 \times 4 = 8$ simulated data samples using the same DFT approach as Zhu and Jia (2018). They used the pre-whitening technique, where DFT detects one signal at the time (Scargle, 1982; Reegen, 2007). We apply DFT to the original simulated data. This gives us the first P_1 period. The least squares fit is then made to the original simulated data, where the pure sine model has the P_1 period. This “first DFT model” gives the first sample of residuals. DFT is applied to this first sample of residuals, which gives the second P_2 period. The next least squares fit is made to the first sample of residuals using a pure sine model having a period P_2 . The model for this sample is called “the second DFT model”. This gives the second sample of residuals.

The DFT pre-whitening technique has its limitations. The DFT *can only* be used to cross-check the DCM pure sine model analysis results for non-weighted data. DFT *can not* be used to cross-check the DCM double wave model analysis results, nor the DCM weighted data analysis results.

In the next Sections 5.2 and 5.3, we perform the DCM and DFT analyses of the $2 \times 4 = 8$ simulated data samples, and compare the results. The results for each individual simulated sample are presented in one vertical column of Figures 2 and 3, where the dashed vertical lines intersecting the periodograms denote the *simulated frequencies* $1/P_1 = 1/10$ and $1/P_2 = 1/11$. The diamonds at the DFT periodogram maxima and the DCM periodogram minima denote the *detected frequencies*. Hence, the vertical dashed lines intersect the diamonds only if the method detects the correct frequencies.

5.2. Results for two equal amplitude signals

We present the results for equal amplitudes $a_1 = a_2 = 50$ in Figure 2.

The results for the shortest simulated time interval, $\Delta T = 70$, are shown in Figures 2a-2f. The DFT periodogram $z_{\text{DFT}}(f)$ shows only one peak at $P_1 = 10.44$ (Figure 2a). The limitation of Equation 35 prevents the detection of two peaks. The effect $[(f_1 + f_2)/2]^{-1} = 10.48$ (Equation 36) explains the detected wrong period $P_1 = 10.44$ value. The first DFT model residuals have a standard deviation $s_\epsilon = 50$, and show regular periodic variation (Figure 2b). The DFT periodogram for these residuals shows the highest peak at $P_2 = 11.50$ (Figure 2c). The second DFT model residuals have a standard deviation of $s_\epsilon = 45$ and show some regular periodic variation (Figure 2d). DCM detects the $P_1 = 9.99$ and $P_2 = 11.12$ periods, which are close to, but not exactly equal to the simulated 10 and 11 values (Figure 2e). The DCM model residuals show no periodic variation and follow a straight line (Figure 2f). This residual distribution resembles a random distribution. The DCM model residuals $s_\epsilon = 41$ standard deviation is much smaller than the DFT model residuals $s_\epsilon = 45$ standard deviation. In this $\Delta T = 70$ simulation, DFT fails and DCM succeeds.

Both DFT periodograms are double-peaked in the longer $\Delta T = 90$ simulation (Figures 2g and 2i). DFT detects the $P_1 = 11.16$ and $P_2 = 9.90$ periods, which are closer to the simulated values. The residuals of both DFT models show periodic variability (Figures 2h and 2j). The mean residual $s_\epsilon = 59$ and 54 values are larger than in the earlier shorter $\Delta T = 70$ simulation, because there is a $\Delta\phi = 0.5$ phase shift (Equation 38) in the simulated y_i^* data at the year 1804.

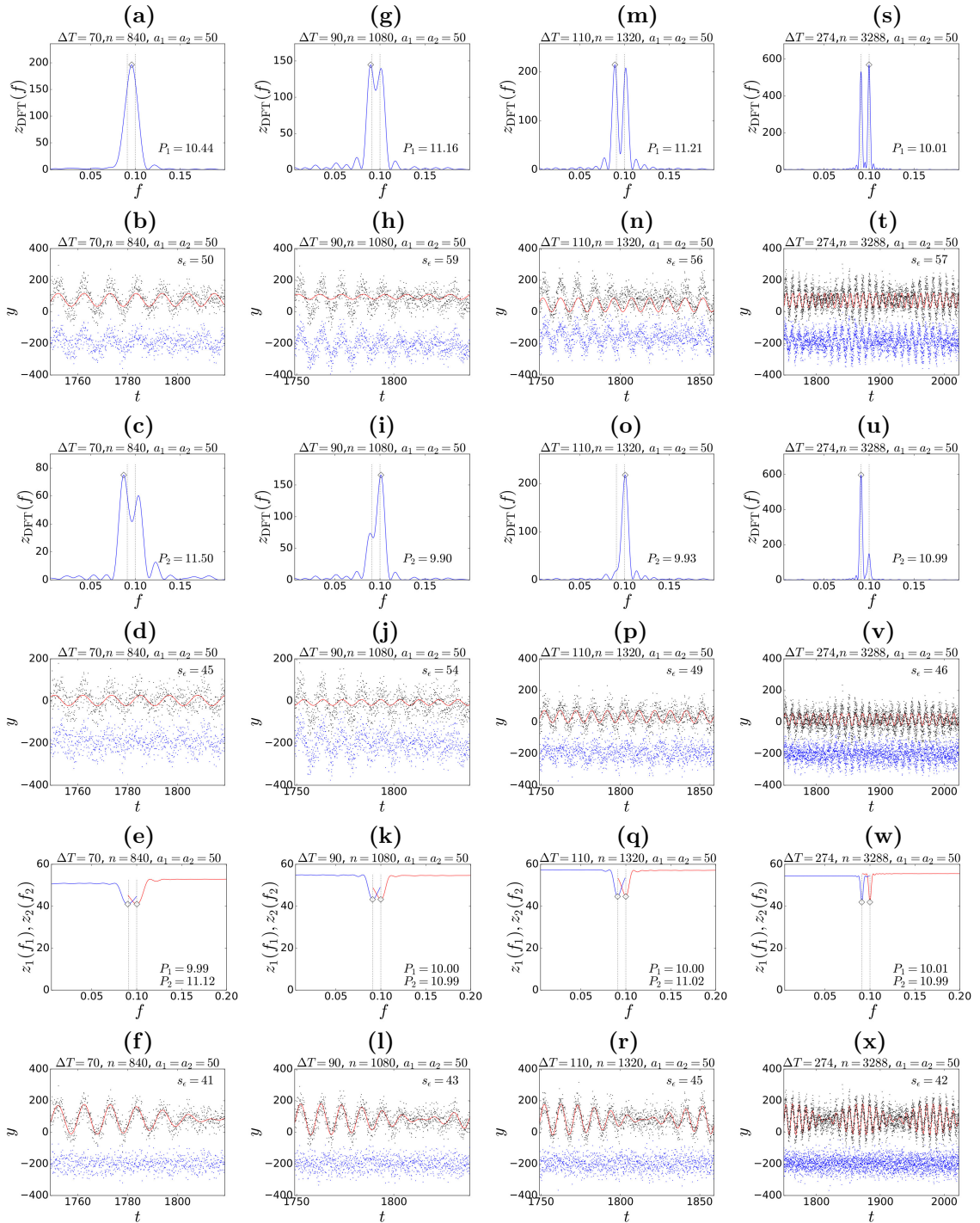


Figure 2. Equal amplitude $a_1 = a_2 = 50$ simulations for signal periods $P_1 = 10$ and $P_2 = 11$ (Equations 33 and 34). (a) DFT periodogram $z_{\text{DFT}}(f)$. Period $P_1 = 10.44$ is detected from y_i^* data simulated with $n = 840$, $\Delta T = 70$, $P_1 = 10$, $a_1 = 50$, $P_2 = 11$ and $a_2 = 50$. Units are $[f] = 1/y$ and $[z_{\text{DFT}}] = \text{dimensionless}$. Vertical dashed black lines denote locations of simulated frequencies $f_1 = 1/P_1$ and $f_2 = 1/P_2$. Diamond denotes location of detected frequency. (b) Model for simulated data. Black dots denote simulated y_i^* data. Red curve denotes pure sine model having period $P_1 = 10.44$. Black dots denote ϵ_i residuals offset to level -200. Standard deviation of residuals is $s_\epsilon = 50$. Units are $[t] = \text{year}$ and $[y] = [\epsilon] = \text{dimensionless}$. (c-d) DFT results for first sample of residuals. Otherwise as in a-b. (e) DCM periodograms $z_1(f_1)$ and $z_2(f_2)$. Periods $P_1 = 9.99$ and $P_2 = 11.12$ are detected from y_i^* data simulated with $n = 840$, $\Delta T = 70$, $P_1 = 10$, $a_1 = 50$, $P_2 = 11$ and $a_2 = 50$. Diamonds denote locations of detected frequencies. Units are $[f] = 1/y$ and $[z_1] = [z_2] = \text{dimensionless}$. (f) Model for simulated data. Black dots denote simulated y_i^* data. Red curve shows two pure sine signal DCM model. Blue dots denote ϵ_i residuals offset to level -200. Standard deviation of residuals is $s_\epsilon = 41$. Units are $[t] = \text{year}$ and $[y] = [\epsilon] = \text{dimensionless}$. (g-l) Data simulated for longer time interval $\Delta T = 90$. Otherwise as in a-f. (m-r) Data simulated for longer time interval $\Delta T = 110$. Otherwise as in a-f. (s-x) Data simulated for longer time interval $\Delta T = 274$. Otherwise as in a-f.

DCM detects the correct $P_1 = 10.00$ and $P_2 = 10.99$ periods (Figure 2k). The distribution of DCM model residuals resembles that of a random distribution, and there is no periodic variability (Figure 2l). The $s_\epsilon = 43$ value of DCM model is much smaller than the $s_\epsilon = 54$ value of DFT model, because the DCM can handle the $\Delta\phi = 0.5$ phase shift (Equation 38). Again, DCM performs better than DFT.

In the next $\Delta T = 110$ simulation, the criterion of Equation 35 is fulfilled, and therefore the first DFT periodogram is clearly double-peaked (Figure 2m). DFT detects the $P_1 = 11.21$ and $P_2 = 9.93$ periods, which differ from the simulated periods. Both DFT model $s_\epsilon = 56$ and 49 mean residual values are large (Figures 2n and 2p). These DFT residuals show periodic variability. DCM detects the correct $P_1 = 10.00$ and $P_2 = 11.02$ periods (Figure 2q). The distribution of DCM model residuals appears random, and its standard deviation is $s_\epsilon = 45$ (Figure 2r). The abrupt phase shift in the simulated y_i^* data (Equation 38) at the year 1804 misleads DFT, but it does not mislead DCM.

Two abrupt phase shifts, in the years 1804 and 1914, occur in the last $\Delta T = 274$ simulation (Equation 38). Finally, DFT succeeds in finding the correct $P_1 = 10.01$ and $P_2 = 10.99$ periods (Figures 2s and 2u). However, the residuals of both DFT models still show periodic variability (Figures 2t and 2v). DCM detects the correct $P_1 = 10.01$ and $P_2 = 10.99$ periods (Figures 2w). The DCM model residuals show no periodic variability, and their distribution resembles a random distribution (Figures 2x). The standard deviation $s_\epsilon = 46$ of the DFT model clearly exceeds the $s_\epsilon = 42$ value of DCM model. In short, DCM performs better than DFT.

5.3. Results for two unequal amplitude signals

We present the results for unequal amplitudes $a_1 = 25$ and $a_2 = 50$ in Figure 3.

All details are not discussed, as in the case of Figure 2. We concentrate only on the general results in Figure 3, because they are the same for all $\Delta T = 70, 90, 110$ and 274 simulations.

If the relation of Equation 35 is not fulfilled, DFT can not detect the correct period values, but DCM can. If this relation is fulfilled, DFT can also succeed.

The relation of Equation 37 predicts that the frequency $f_2 = 1/P_2 = 1/11$ of the stronger signal dominates in the frequency $f(t)$ of the $s(t)$. Therefore, DFT always detects this $P_2 = 11$ period signal first. DCM detects both signals simultaneously, neither one of them being “the first”.

DFT can not model the amplitude changes or the abrupt phase shifts (Equation 38). For this reason, the DFT model residuals always show periodic variability, while the DCM model residuals do not. DCM residuals have a random distribution concentrated on a straight line, which is a signature of a good model. DFT model s_ϵ values are always larger than DCM model s_ϵ values. This means that some information is always lost at every DFT pre-whitening stage, where one pure sine signal is detected at the time. Both methods reach s_ϵ levels that are close to the standard deviation $s = 42$ of the random errors σ_i^* , which are added as noise to the simulated data (Equation 39). This means that both methods can also detect the second, weaker $P_1 = 10$ signal, which has the peak to peak amplitude $A_1 = 2a_1 = 50$ that has the same order of magnitude as $s = 42$. However, only DCM can reach this $\sigma_\epsilon \approx s = 42$ level for all $2 \times 4 = 8$ simulations.

5.4. Discrete Fourier Transform (DFT) analysis of Rmonthly

We simulate data arising from the interference between two sine waves having frequencies $f_1 \approx f_2$ (Equation 39). Our DFT and DCM analyses of these simulated data reveal the performance differences between these two methods. We encounter the same five DFT drawbacks for equal and unequal amplitude sine waves (Sections 5.2 and 5.3).

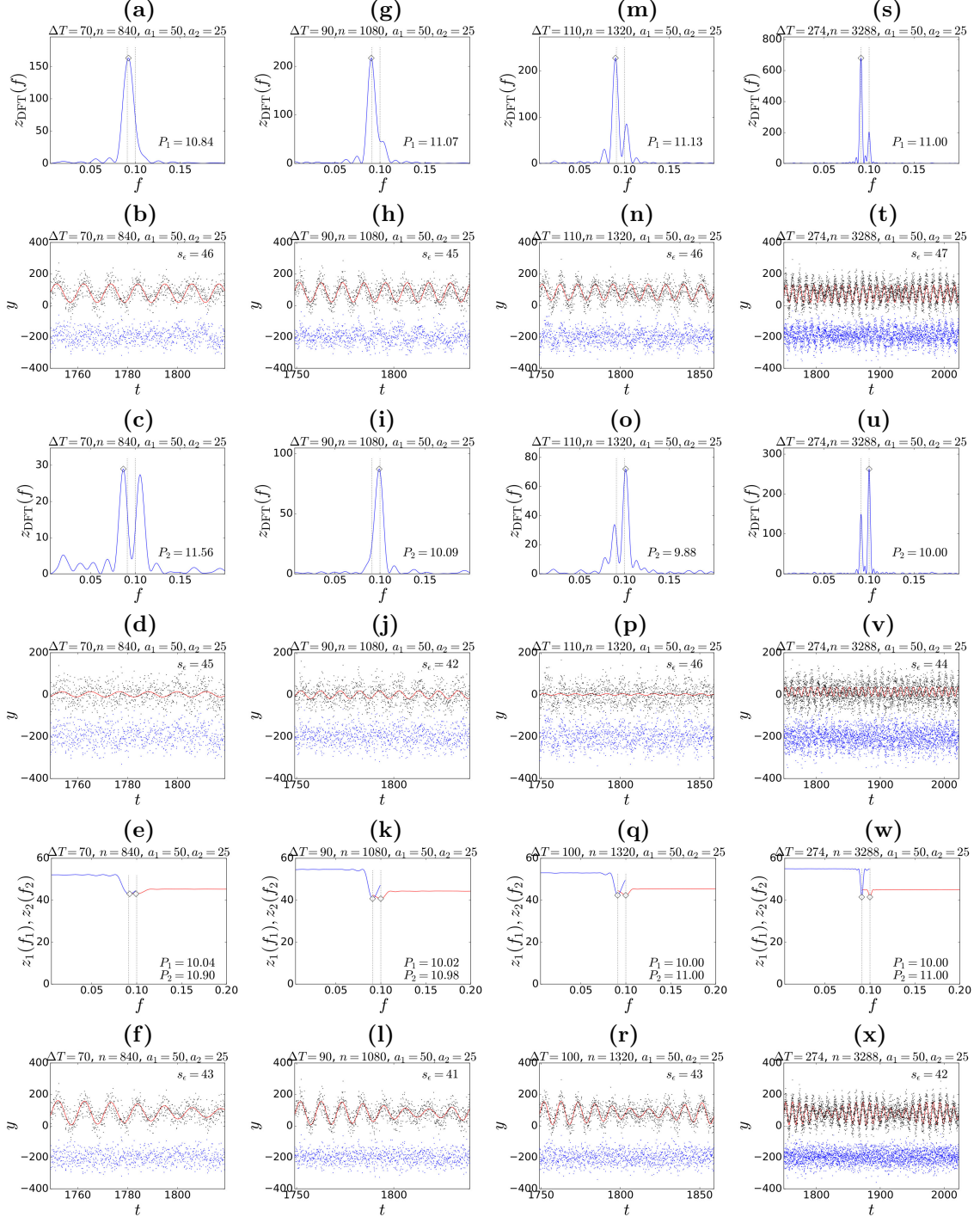


Figure 3. Unequal amplitude $a_1 = 25$ and $a_2 = 50$ simulations for signal periods $P_1 = 10$ and $P_2 = 11$ (Equations 33 and 34). Otherwise as in Figure 2.

Table 8. Synodic period connections. (1) P_1 period. (2-5) P_2 period. Next lines: P_{\pm} periods for P_1 and P_2 combinations (Equation 40). Signals S_{10y} and S_{11y} connect to signal S_{110y} . Signals $S_{11,y86}$ and S_{110y} connect to signal $S_{10,y6}$. Signal $S_{10,y6}$ has no direct connection to signals S_{10y} or S_{11y} .

(1)	(2)	(3)	(4)	(5)
	$P_2 = S_{10,y6}$	$P_2 = S_{11y}$	$P_2 = S_{11,y86}$	$P_2 = S_{110y}$
$P_1 = S_{10y}$	$P_- = 177$ $P_+ = 5.15$	$P_- = 110$ $P_+ = 5.24$	$P_- = 63.8$ $P_+ = 5.42$	$P_- = 11.0$ $P_+ = 9.17$
$P_1 = S_{10,y6}$		$P_- = 292$ $P_+ = 5.40$	$P_- = 99.8$ $P_+ = 5.60$	$P_- = 11.7$ $P_+ = 9.67$
$P_1 = S_{11y}$			$P_- = 152$ $P_+ = 5.71$	$P_- = 12.2$ $P_+ = 10.0$
$P_1 = S_{11,y86}$				$P_- = 13.3$ $P_+ = 10.7$

1. Detection of close frequencies: DFT suffers from the limitation of Equation 35, but DCM does not.
2. Wrong frequency detection: DFT suffers from the misleading effects of Equations 36 and 37, but DCM does not.
3. Abrupt phase shifts: DFT can not model the abrupt phase shifts of Equation 38, but DCM can.
4. Biased residuals: DFT pre-whitening model residuals do not have a random distribution, but DCM model residuals do. The mean residual s_{ϵ} values of DFT models are always larger than those of DFT models, which means that some information is lost at every DFT pre-whitening stage.
5. Detection accuracy: The difference between the detected and the simulated period values is larger for DFT than for DCM. This difference decreases as the samples become longer. For real data, this means that DCM detects the correct period values more probably than DFT.

When DFT analysis fails, DCM analysis can succeed. We can safely state that DCM performs better than DFT. The two strongest S_{11y} and S_{10y} signals in the real data sample R_{monthly} are exactly the same as in our simulations. When we use DFT pre-whitening to search for more than two signals in this real data sample R_{monthly} , it is logical to assume that the above-mentioned five DFT drawbacks become more pronounced.

The DFT pre-whitening results for the sample R_{monthly} are shown in Figure 4. The first five S_{11y} , S_{10y} , $S_{11,y86}$, S_{110y} and $S_{10,y6}$ signals detected using DFT pre-whitening (Figure 4 a-j) are the same as those detected using the five pure sine signal DCM model (Table 6: Column 3). The only minor difference is that DCM detects signal $S_{10,y6}$ before signal S_{110y} . Both methods give nearly the same amplitudes for these five strongest signals. The sixth-strongest detected signals are different: the S_{53y} signal for DCM (Table 6: Column 3) and the $S_{8,y4}$ signal for DFT (Figure 4 k-l). The seventh-strongest detected signals are also different, the S_{8y} signal for DCM and the S_{53y} signal for DFT. DCM detects only seven signals from sample R_{monthly} , because the unstable $M=8$ model is rejected (DCM-manual: Table 7, “UM”). DCM analysis of predictive data sample $R_{\text{monthly2000}}$, which is a subsample of all data sample R_{monthly} , indicates that the correct number of real signals is six (Section 6.2.2: Figure 6). We conclude that DCM and DFT detect the same five strongest signals from sample R_{monthly} .

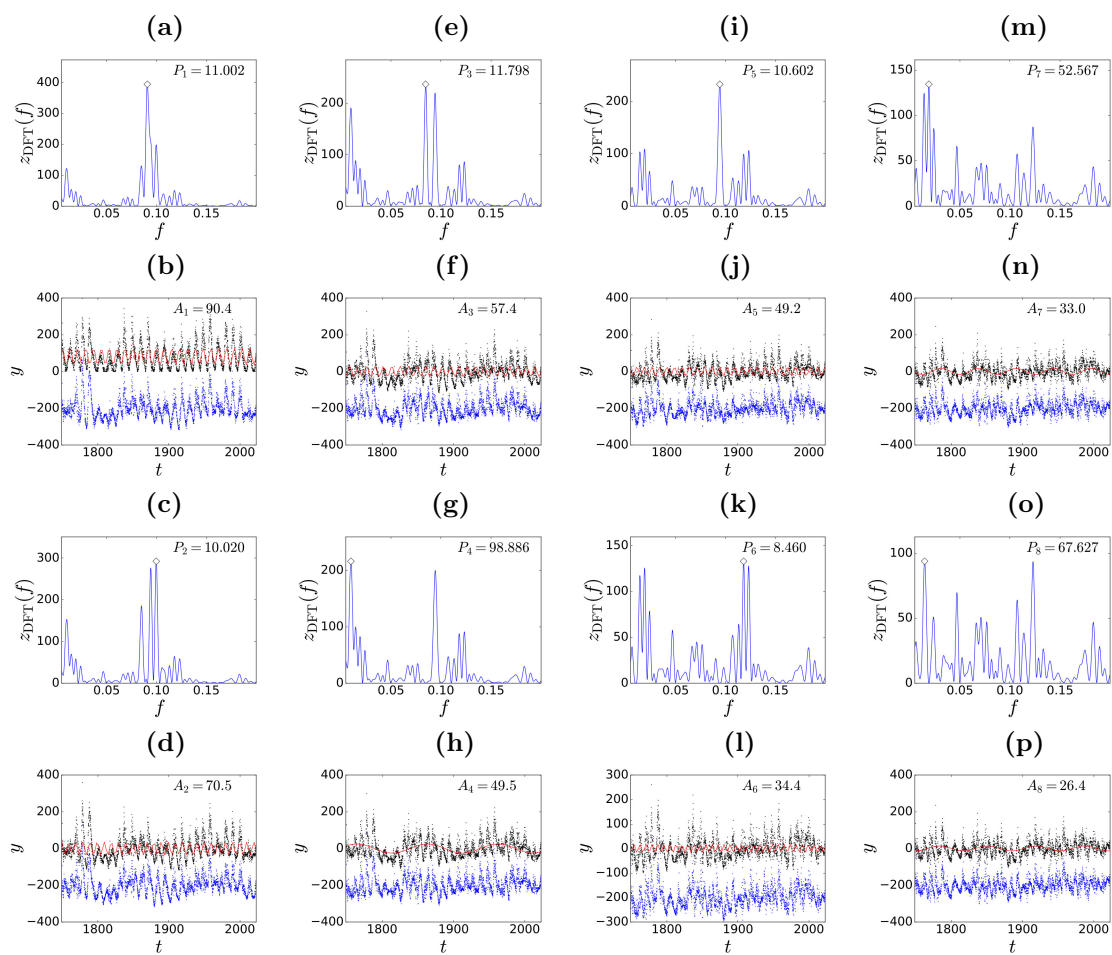


Figure 4. DFT pre-whitening analysis results for Rmonthly sample. (a) DFT periodogram for original data. Diamond denotes peak of periodogram at frequency of best period $P_1 = 11.002$ years. Units are $[f] = 1/y$ and $[z_{\text{DFT}}] = \text{dimensionless}$. (b) Pure sine model for original data. Black dots denote original y_i data. Red curve denotes sine model with period $P_1 = 11.002$. Its peak to peak amplitude is $A_1 = 90.4$. Blue dots denote residuals ϵ_i offset to level -200. Units are $[t] = \text{years}$ and $[y] = [\epsilon] = [A] = \text{dimensionless}$. (c-d) Second signal detected from first sample of residuals. (e-f) Third signal detected from second sample of residuals. (g-h) Fourth signal detected from next sample of residuals. (i-j) Fifth signal. (k-l) Sixth signal. (m-n) Seventh signal. (o-p) Eighth signal. Notations for all panel pairs from “c-d” to “o-p” are same as in panel pair “a-b”.

These five strongest signals are clearly connected to each other (Table 8). Their ± 1 round synodic period difference connections

$$P_{\pm} = [P_1^{-1} \pm P_2^{-1}]^{-1} \quad (40)$$

are given in Table 8. These five strongest signals can, and inevitably do, interact through these one round differences. This means that the interference of these five signals is repeated indefinitely.

It is essential to understand, why the DFT pre-whitening analysis of Rmonthly sample does succeed, regardless of all five DFT drawbacks discussed above? The limitation of Equation 35 is encountered, because the difference between the $S_{10,y6}$ and $S_{11,y}$ signal frequencies is smaller than f_0 (Table 7). All four $S_{10,y}$, $S_{10,y6}$, $S_{11,y}$ and $S_{11,y86}$ signal frequencies are closely packed within an interval of $(27.38 - 23.09)f_0 = 4.29f_0$ independent frequencies. The interference of these four

Table 9. Significance estimates for DCM and DFT period detections from **Rmonthly** sample. (1) Detection order. (2) DCM period P . (3) DCM critical level Q_F (Equation 28). (4) DFT period P . (5) DFT term E_{DFT} (Equation 41). (6) DFT false alarm probability Q_{DFT} (Horne and Baliunas, 1986, their Equation 22).. Note that DCM model for period 8.456 is unstable (“UM”).

(1)	DCM		DFT		
	P	Q_F	P	E_{DFT}	Q_{DFT}
	(2)	(3)	(4)	(5)	(6)
1	11.0324	–	11.002	1.8×10^{-162}	0
2	10.0001	$< 10^{-16}$	10.020	5.5×10^{-128}	0
3	11.807	$< 10^{-16}$	11.798	1.7×10^{-103}	0
4	99.92	$< 10^{-16}$	98.886	1.7×10^{-90}	0
5	10.569	$< 10^{-16}$	10.602	4.0×10^{-102}	0
6	52.66	$< 10^{-16}$	8.460	2.2×10^{-58}	0
7	8.1087	$< 10^{-16}$	52.567	8.9×10^{-59}	0
8	8.456 UM	$< 10^{-16}$	67.627	4.0×10^{-41}	0

signals enhances the misleading effects of Equations 36 and 37. The amplitudes of S_{10y} , $S_{10,y6}$ and $S_{11,y86}$ signals are nearly equal. This causes many abrupt large $\Delta\phi \approx 0.5$ phase shifts during $\Delta T = 274$ (Equation 38). Nevertheless, the DFT pre-whitening analysis succeeds, because signal S_{11y} amplitude $A_1 = 90.4$ is crucially larger than signal S_{10y} , $S_{10,y6}$ and $S_{11,y86}$ amplitudes. As predicted by Equation 37, this S_{11y} signal is detected first. After the pre-whitening subtraction of this strongest signal, the remaining S_{10y} , $S_{10,y6}$ and $S_{11,y86}$ signals no longer suffer from the f_0 limitation of Equation 35. The two highest amplitude $A_2 = 70.5$ and $A_3 = 57.4$ signals S_{10y} and $S_{11,y86}$ are now “comfortably separated” by $(27.38 - 23.09)f_0 = 4.29f_0$ independent frequencies. As predicted by the relation of Equation 37, these two signals are detected next (Figure 4c-f). The frequency difference between the remaining $S_{10,y6}$ and S_{110y} signals is so large that DFT can easily detect them. Our DFT pre-whitening analysis of sample **Rmonthly** succeeds, because one strong S_{11y} signal dominates, and the remaining signals are detected in a suitable order. This successful DFT analysis also confirms that the data does not contain any misleading long-term trends.

Our Table 9 gives the significance estimates for the DCM and DFT period detections from the **Rmonthly** sample. The DCM gives no direct significance estimate for the first detected strongest 11.032 year period. After Wolf (1852) discovered this S_{11y} signal, it has been re-detected perhaps more than a million times. If this 11.032 year signal is not an artefact, the DCM detections for the next six periods are extremely significant because the Fisher-test always rejects the H_0 hypothesis at critical levels $Q_F < 10^{-16}$ (Equation 28). The DCM model for the eighth strongest 8.456 year period is unstable (DCM-manual: Table 7, $M=8$).

For the DFT analysis, our Table 9 gives the values for the term

$$E_{DFT} = e^{-(n/2)(1+\xi^{-1})^{-1}}, \quad (41)$$

where $\xi = (A/2)^2/(2s_e^2)$, A is the sine peak to peak amplitude and s_e is the standard deviation residuals (variance of noise). This E_{DFT} parameter is used to compute the false alarm probability Q_{DFT} (Horne and Baliunas, 1986, their Equation 22). All E_{DFT} values are so close to zero that all false alarm probabilities Q_{DFT} are practically equal to zero. This means that all DFT period detections are extremely significant.

In short, all DCM and DFT period detections in Table 9 are absolutely certain, if the data contain only white noise. One could argue that our significance estimates can be unreliable because we do not consider the possibility that the data contains red noise (Vaughan, 2005). We test the H_0 hypothesis in our DCM analysis with the Fisher-method (Equation 28). If the data contained red noise, it would influence both the simple model and the complex model of the Fisher-test. Hence, our the DCM analysis results are correct with or without the red noise. We admit that the red noise could contaminate our DFT analysis significance estimates, but then again we detect the same periods with the DCM and the DFT. For some reason, the extreme significance estimates for the DFT period detections from the sunspot data have not caught the attention that they would have deserved in the earlier studies (e.g. Zhu and Jia, 2018).

Finally, we repeat the daily sunspot data DFT pre-whitening analysis in Zhu and Jia (2018). They did not detect the S_{110y} signal because they searched for periods between 2 and 18 years. For our tested period interval between 5 and 200 years, DFT detects the five strongest 10.87, 10.14, 110.6, 12.00, and 7.99 year signals. These five periods are closest to the five best periods that DCM detects in the weighted data (Table 6: Columns 7 and 13). The probable cause for the minor numerical value differences is that DFT tends to detect less accurate real period values than DCM (Sections 5.2 and 5.3). Our DFT detection of the 110.6 signal from these daily sunspot data removes the two weak 8.92 and 5.44 year signals detected by Zhu and Jia (2018). We do not apply DCM to the daily sunspot data for a simple reason. For a cluster of parallel computation processors, it takes about two days to compute the four signal DCM model for one monthly sunspot data sample. For one daily sunspot data sample, this four signal DCM model computation would take months, and the computations of many samples would take years.

We conclude that the DCM and DFT detect the same strictly periodic signals from the sunspot data. Both methods give extreme significance estimates for these signals. These period detections are absolutely certain. In earlier studies, the DFT, like all other methods that search for one period at the time, has failed to detect the exact correct numerical period values. The DCM does not fail, as illustrated in Figures 2 and 3, where the vertical dashed lines (simulated periods) intersect the diamonds (detected periods) much more often for DCM than for DFT.

6. Predictions

The two alternative theories for the origin of the sunspot cycle are the stochastic solar-dynamo-theory and the deterministic planetary-influence-theory. The easiest way to refer to these two alternative theories is to formulate these hypotheses:

H_{Dynamo} : “*The solar dynamo is a stochastic process. Therefore, deterministic sunspot number predictions longer than one solar cycle fail.*”

H_{Planet} : “*Planetary motions are deterministic. Therefore, deterministic sunspot number predictions longer than one solar cycle can succeed.*”

6.1. Solar Cycle Prediction Panel prediction

It is crucial to check what level of predictability has already been reached. In the year 2019, the Solar Cycle Prediction Panel representing NOAA, NASA and the International Space Environmental Services (ISES) made the official forecast for solar cycle 25. The red curve in Figure 5 shows the synthesis of about 50 different forecasts received from the scientific community. During the current sunspot cycle 25, the maximum difference between the observed y_{13} and the predicted g_{13} smoothed thirteen month mean has been

$$s_{\text{ISES}} = |y_{13} - g_{13}|_{\text{max}} = |\epsilon|_{\text{max}} = 52.0 \quad (42)$$

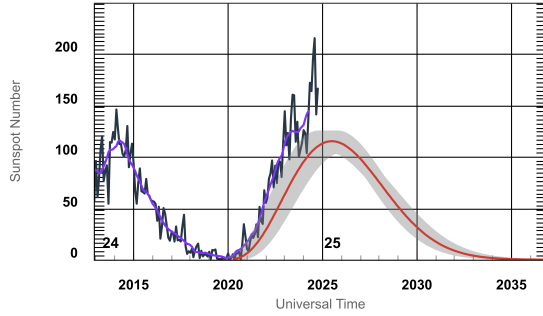


Figure 5. Solar Cycle Prediction Panel forecast for solar cycle 25. Red curve shows predicted monthly sunspot numbers after December 2019. Grey shaded area shows prediction error. Black curve denotes observed monthly sunspot number up to October 2024. Blue line denotes observed smoothed 13 months mean y_{13} up to April 2024.

on March 2024.⁵ This gives an estimate for the accuracy that could be achieved in sunspot number predictions for the past five years after 2019. We do not argue that this is the best achievable accuracy, but this is the current best official published forecast. However, this accuracy would certainly be worse if this forecast covered more than one solar cycle. The s_{ISES} parameter of Equation 42 is hereafter referred to as the “five year ISES limit”. If our model prediction deviates less than s_{ISES} from the predicted observations, we state that the prediction is “within the ISES limit”. In such cases, our prediction $g(t)$ deviates less than s_{ISES} from y_{13} .

We evaluate predictivity z_{pred} for the six pairs of predictive and predicted data (Equation 30). The six all data samples are used to predict m_{pred} for the past prolonged activity minima (Equation 32). We use the red continuous and dotted lines to denote the model and the model errors, respectively. The sliding thirty years mean of this model and the sliding mean error are denoted with the green continuous and dotted curves. We will show many predictions extending to time intervals before and after the analysed samples (Figures 6, 7, 8, 9 and 10). The thirty years sliding mean predictions are always more accurate than the model predictions (Figures 6-10: red curves). Therefore, the green curve errors (dotted green lines) are always smaller than the red curve errors (dotted red lines). The red model curve predictions are shown only for the first few cycles after the newest, most accurate sunspot data. Since the oldest sunspot data are sparse and inaccurate, we show no red curve predictions before these data. The thirty years sliding mean green curve predictions are shown for the time intervals before and after the sunspot data. To ensure easy readability of all Figures 6-10, we surround the realm of our predictions with black dash-dotted rectangles. We also use long black horizontal arrows to highlight the direction of these predictions in time. The dash-dotted cyan lines in all model residuals ϵ_i plots denote the five year ISES limits $\pm s_{\text{ISES}}$ (Equation 42).

6.2. Non-weighted monthly sunspot data

6.2.1. Pure sines

Sample `Rmonthly2000` contains the predictive data. The predicted data are the `Rmonthly` sample observations after the year 2000. The whole `Rmonthly` sample represents all data.

The smallest predicted test statistic z_{pred} (Equation 30) value is achieved for the five pure sines $\mathcal{M}=5$ model (Figure 6a). Predictability is better for one signal than for two signals. Then,

⁵Space Weather Prediction Center on November 21, 2024.

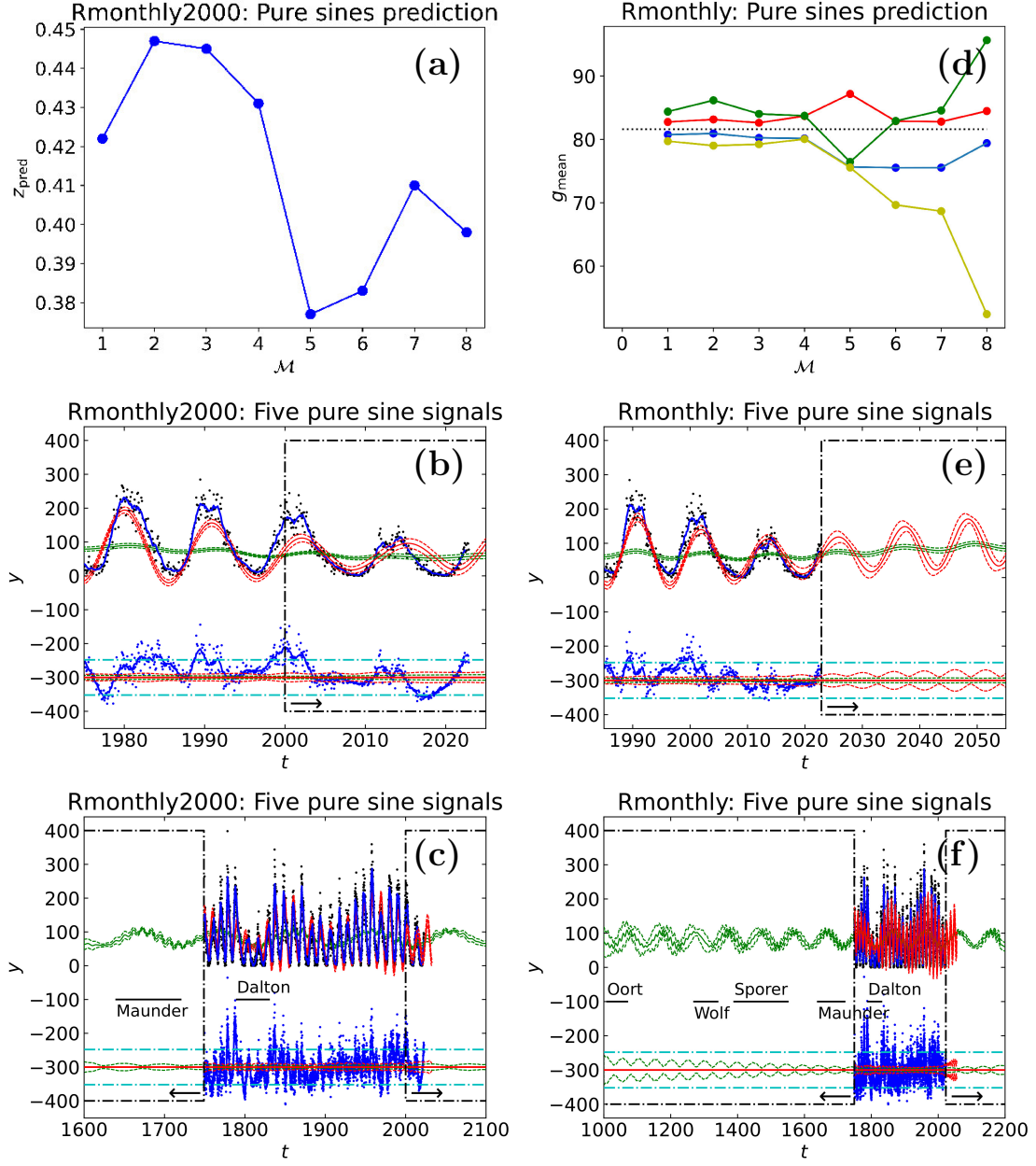


Figure 6. (a) Rmonthly2000 predictions for pure sines (DCM-manual: Table 6). (a) Predicted test statistic z_{pred} (Equation 30) for pure sine models $\mathcal{M}=1\text{--}8$. Best model $\mathcal{M}=5$ minimises z_{pred} . Units are x-axis $[\mathcal{M}]$ =dimensionless and y-axis $[z_{\text{pred}}]$ =dimensionless. (b) Black dots denote data y_i . Blue continuous line denotes 13 month smoothed data. Red continuous line denotes $g(t)$ model $\mathcal{M}=5$. Dotted red lines denote $\pm 3\sigma$ model error limits for $g(t)$. Green continuous line denotes model $g(t)$ thirty years sliding mean. Dotted green lines show $\pm 3\sigma$ error limits for this sliding mean. Predictive data ends at vertical dash-dotted black line. Predicted data, predicted model and predicted thirty years mean are surrounded by this black dash-dotted line. Black arrow shows prediction direction in time. Blue dots denote residuals ϵ_i offset to level -300, which is outlined with red continuous line. Dash-dotted cyan lines denote ISES prediction SIES error limit (Equation 42). Units are x-axis $[t]$ =years and y-axis $[y]$ =dimensionless. (c) Horizontal black continuous lines outline time intervals of Dalton and Maunder minima. Except for a longer time span, otherwise as in “b”. (d) Rmonthly predictions for pure sines (DCM-manual: Table 7): Predicted mean level m_{pred} (Equation 32) for pure sine $\mathcal{M}=1\text{--}8$ models during Maunder (red), Sporer (blue), Wolf (green) and Oort (yellow) minima. Dotted black line shows the mean $m = 81.6$ for all y_i data. Units are x-axis $[\mathcal{M}]$ =dimensionless and y-axis $[m_{\text{pred}}]$ =dimensionless. (e) $\mathcal{M}=5$ model for modern times and its prediction after year 2022. Otherwise as in “b”. (f) $\mathcal{M}=5$ model for long-term past and future. Otherwise as in “c”

this z_{pred} predictability improves for three, four and five signals. This z_{pred} improvement trend indicates that these five first signals are deterministic, not stochastic. Six signals give nearly the same predictability. For more than six signals, predictability becomes worse. Furthermore, the seven and eight signal models are unstable (DCM-manual: Table 6, “UM” models $\mathcal{M}=7$ and 8). We compute z_{pred} values also for these unstable models, just to verify, if predictability stops improving due to instability.

For the predictive `Rmonthly2000` data sample, the five signal prediction after 2000 succeeds quite well until a clear deviation from the data occurs in the year 2013 (Figure 6b). Most of the blue dots denoting the predictive model residuals are within the horizontal cyan dash dotted lines of ISES limit (Equation 42).

The five pure sines model can reproduce the Dalton minimum because it is inside the predictive data (Figure 6c). There is a dip at the end of the Maunder minimum, but the prediction for the duration of the Maunder minimum fails.

The DCM pure sine model analysis results for `Rmonthly` are given in the DCM-manual (Table 7). This all data sample gives the predicted mean level m_{pred} (Equation 32) values for the past activity minima. These predictions are not convincing (Figure 6d). Only the blue and yellow circles denoting Sporer and Oort minima are below the black horizontal dotted line denoting the mean level $m = 81.6$ of all sunspot numbers. `Rmonthly` sample pure sines prediction indicates that the current prolonged low solar activity level has just ended (Figure 6e: green curve). The long-term past and future predictions are shown in Figure 6f.

6.2.2. Double waves

The predictive data sample is `Rmonthly2000`. All data sample is `Rmonthly`. The `Rmonthly` sample values after the year 2000 are the predicted data.

The DCM double wave model results for `Rmonthly2000` and `Rmonthly` samples are given in the DCM-manual (Tables 8 and 9, respectively). For both samples, the periods and amplitudes of the eight strongest double wave signals are summarised in Table 6 (Columns 4 and 5).

The prediction test statistic z_{pred} (Equation 30) decreases until six signals are detected. Then, z_{pred} begins to increase for seven and eight signals (Figure 7a). This indicates that the first six detected signals are real, but the next seventh and eighth signals are not.

The prediction obtained from the predictive data `Rmonthly2000` sample begins after the black vertical dash-dotted line at the year 2000 (Figure 7b). For twenty years, the majority of predictive model residuals (blue dots) are within the ISES limit (Equation 42: cyan dash dotted lines). The six signal double wave DCM model can reproduce the Dalton minimum inside `Rmonthly2000`. The thirty years sliding mean shows a dip at the end of the Maunder minimum. This dip outside sample `Rmonthly2000` does not cover the whole Maunder minimum era (Figure 7c: green curve).

The predictive data `Rmonthly2000` sample z_{pred} (Equation 30) values indicate the presence of six signals (Figure 7a). The all data `Rmonthly` sample mean level prediction m_{mean} (Equation 32) for the Maunder minimum supports this result. The predicted mean level m_{mean} curve for the Maunder minimum shows an expected dip (Figure 7d: red curve). For the first three $\mathcal{M}=1-3$ signals, this red m_{pred} curve is above the all data mean level m denoted with dotted black line. For the next three $\mathcal{M}=4-6$ signals, the m_{pred} values fall below the m mean level. Finally, these m_{mean} values for $\mathcal{M}=7$ and 8 signals rise again above the mean level m .

The Maunder minimum is outside all data sample `Rmonthly`. It is the closest activity minimum before the beginning of this sample. This could explain why only this particular deterministic activity minimum prediction succeeds. The m_{pred} predictions fail for the other activity minima, probably because these minima are further away in the past than the Maunder minimum. The decreasing Oort minimum m_{mean} trend deserves to be mentioned (Figure 7d: yellow curve).

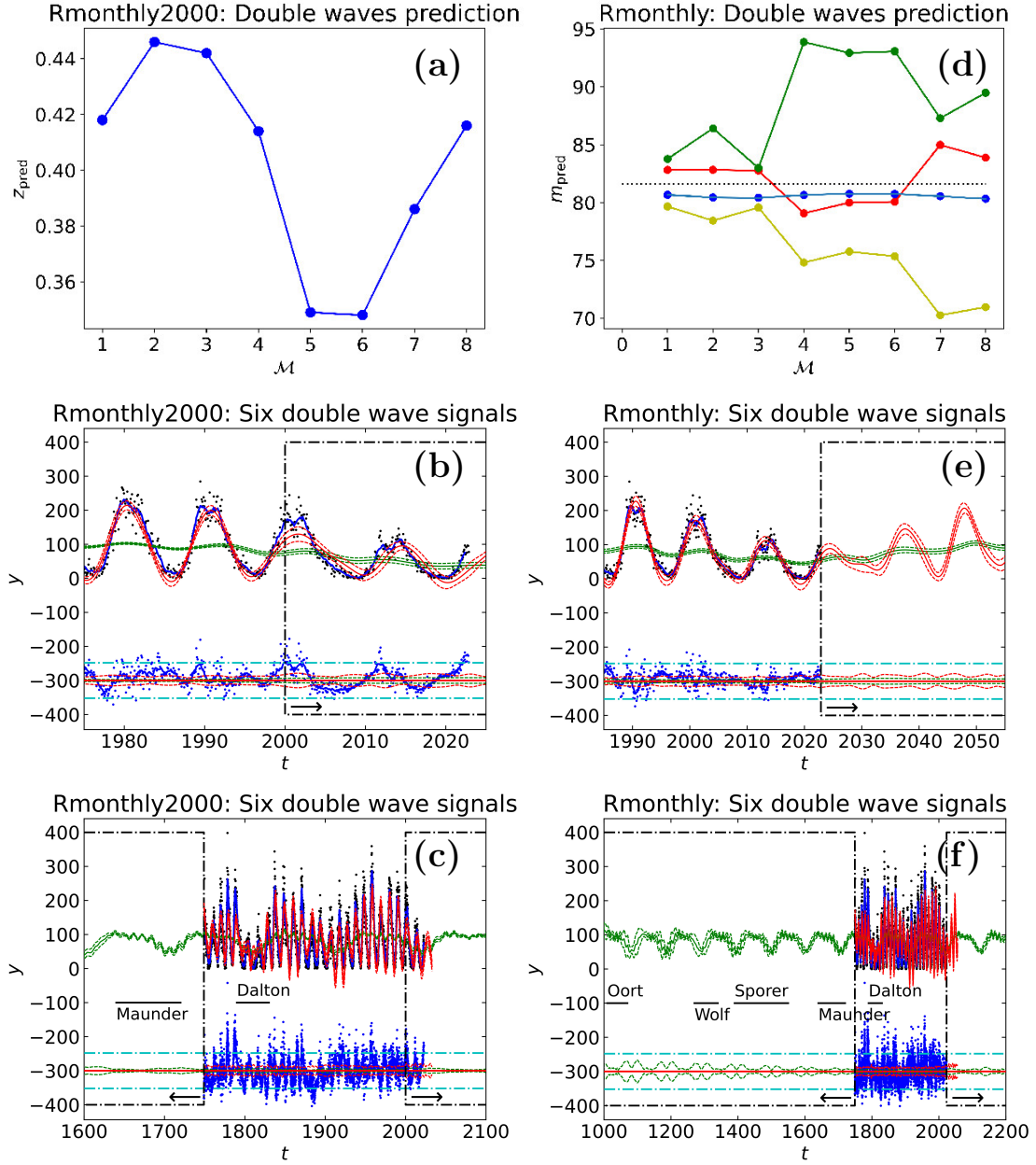


Figure 7. Rmonthly2000 predictions for double waves (DCM-manual: Table 8). (a-c) Best double wave model $M=6$ minimises z_{pred} (Equation 30). Otherwise as in Figures 6a-c. (d-f) Rmonthly predictions for double waves (DCM-manual: Table 9). Otherwise as in Figures 6d-f.

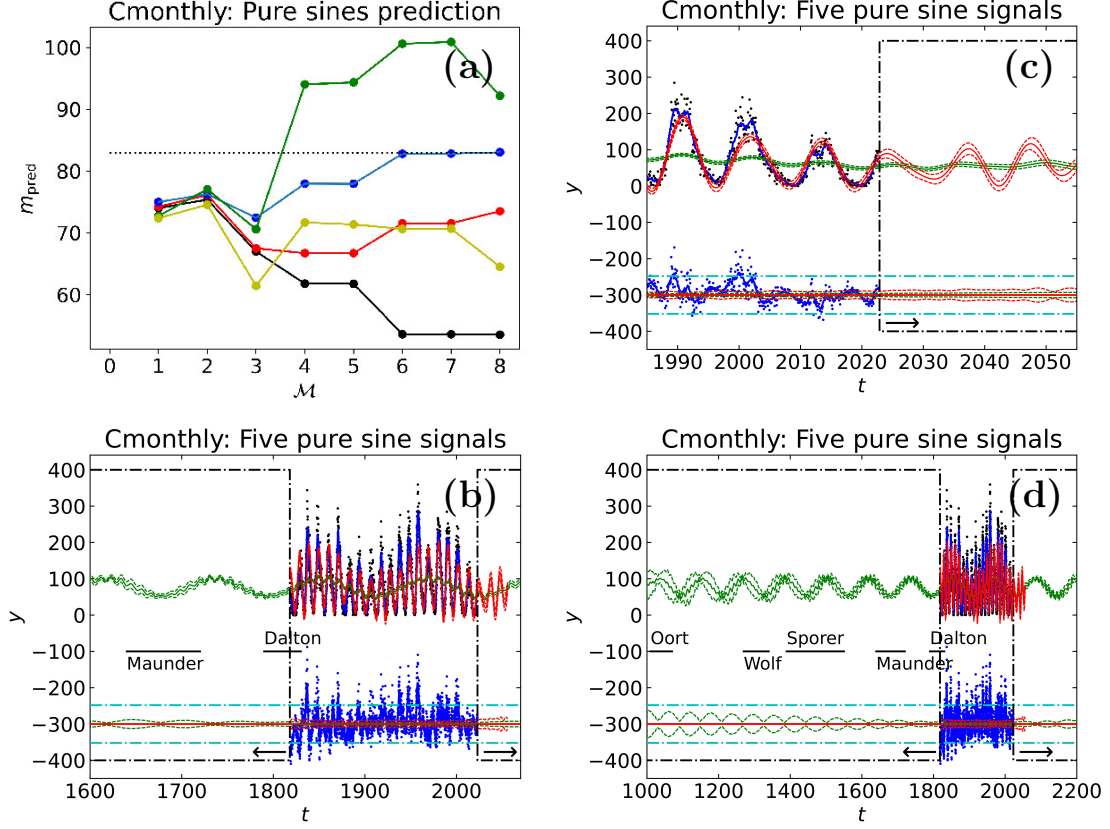


Figure 8. Cmonthly predictions for pure sines (DCM-manual: Table 11). (a) Pure sine $M=1-8$ model predictions for m_{pred} (Equation 32) during Dalton (black), Maunder (red), Sporer (blue), Wolf (green) and Oort (yellow) minima. Otherwise as in Figure 6d. (b) Model $M=5$ pure sine prediction for near past. Otherwise as in Figure 6c. (c) Model $M=5$ pure sine prediction for near future. Otherwise as in Figure 6e. (d) Model $M=5$ pure sine long-term predictions. Otherwise as in Figure 6f.

The six double wave DCM model for all data Rmonthly sample predicts that the mean level of solar activity begins to rise in the near future (Figure 7e: green curve). This model predicts a turning point at 2029, which does not necessarily represent the beginning of a new activity cycle (Figure 7e: red curve). The long-term thirty years sliding mean shows a clear dip during the end of Maunder minimum (Figure 7f: green curve).

6.3. Weighted monthly sunspot data

The Cmonthly2000 sample contains the predictive data. The Cmonthly sample contains all data, where the observations after the year 2000 are the predicted data.

For the predictive data Cmonthly2000 sample, both pure sine and double wave models are unstable for more than two signals (DCM-manual: Tables 10 and 12, “UM”). The detected signals are given in Table 6 (Columns 6 and 8). It is of no use to study predictivity for only two detected signals in sample Cmonthly2000.

For all data sample Cmonthly, all double wave models for two or more signals are unstable (DCM-manual: Table 13, “UM”). The only detected signal is given in Table 6 (Column 9). It would make no sense to study predictivity for only one signal detected in sample Cmonthly.

Fortunately, we can detect five pure sine signals in all data sample **Cmonthly** (DCM-manual: Table 11). These signals are given in Table 6 (Column 7). The predicted mean level m_{pred} (Equation 32) curves are promising (Figure 8a). The m_{pred} curves for all activity minima in Table 1 show a dip at model $M=3$. This dip is clearly below the dotted black line denoting the mean $m = 81.6$ of all monthly sunspot numbers. Except for the green Wolf minimum curve, all m_{pred} curves stay below this mean m . The predicted mean level m_{pred} curve for the Dalton minimum is convincing (Figure 8a: black curve), most probably because this activity minimum between 1790 and 1830 partly overlaps the **Cmonthly** sample between 1818 and 2022. Furthermore, the predicted mean level m_{pred} curve for the second closest Maunder minimum is good (Figure 8a: red curve).

The deterministic predictions for the Dalton and the Maunder minima are illustrated in Figure 8b (green curve). These curves can reproduce the duration of these activity minima, but not the low values of sunspots. The errors for the predicted model (red dotted lines) and the predicted sliding 30 years mean (green dotted lines) are far smaller than the ISES limit (Equation 42: dashed dotted cyan lines). This deterministic prediction is obtained for the two past centuries before the beginning of data. The time span of this successful prediction is about twenty times longer than the one sunspot cycle limit of stochastic H_{Dynamo} hypothesis predictions. Since this model can predict the time intervals of past weak activity, it should also be able to predict the time intervals of future weak activity. The same five pure sine signal prediction for the next decades is shown in Figure 8c (red curve). The long-term prediction confirms the result already obtained earlier for other samples: the activity level of the Sun increases during the next half a century (Figure 8d: green curve).

6.4. Non-weighted yearly sunspot data

The four and eight signal DCM double wave models have $\eta = 21$ and $\eta = 21 + 20$ free parameters, respectively. The yearly sunspot data sample **Ryearly2000** contains only $n = 300$ observations. To avoid over-fitting, we analyse these yearly data only with the four and eight signal DCM pure sine models having $\eta = 13$ and $\eta = 13 + 12$ free parameters.

The **Ryearly** sample contains all data, where observations after 2000 are the predicted data. The **Ryearly2000** sample observations are the predictive data.

The predictive data sample **Ryearly2000** DCM analysis gives the predicted test statistic z_{pred} (Equation 30) values shown in Figure 9a. The best six signal model gives the smallest z_{pred} value. The z_{pred} values for the seven and eight signal models are larger.

This six signal model gives an amazingly accurate prediction for the twenty years of predicted data after the year 2000 (Figure 9b: red curve after the vertical black dash-dotted line). All predicted data values are between the dotted red lines denoting $\pm 3\sigma$ prediction error limits. About half of these black dots denoting the predicted data overlap the continuous red line denoting the predicted model. All residuals of predicted data (blue dots) are significantly smaller than the ISES limit (Equation 42: cyan dash dotted lines). Had we been able to apply DCM to the **Ryearly2000** sample in the year 2000, we could have predicted the yearly sunspots number for the next two decades! The time span of this successful deterministic prediction is about two times longer than the stochastic one sunspot cycle prediction limit of H_{Dynamo} hypothesis.

For **Ryearly2000** sample, the six signal model can reproduce the Dalton minimum inside the predictive data, but not the Maunder minimum, which is outside this sample (Figure 9c: green curve).

The predicted mean levels m_{pred} (Equation 32) for the all data sample **Ryearly** are shown in Figure 9d. Even the red curve for the Maunder minimum, which is closest to the beginning of this **Ryearly** sample, stays above the mean level $m = 78.4$ of all data. These predicted mean

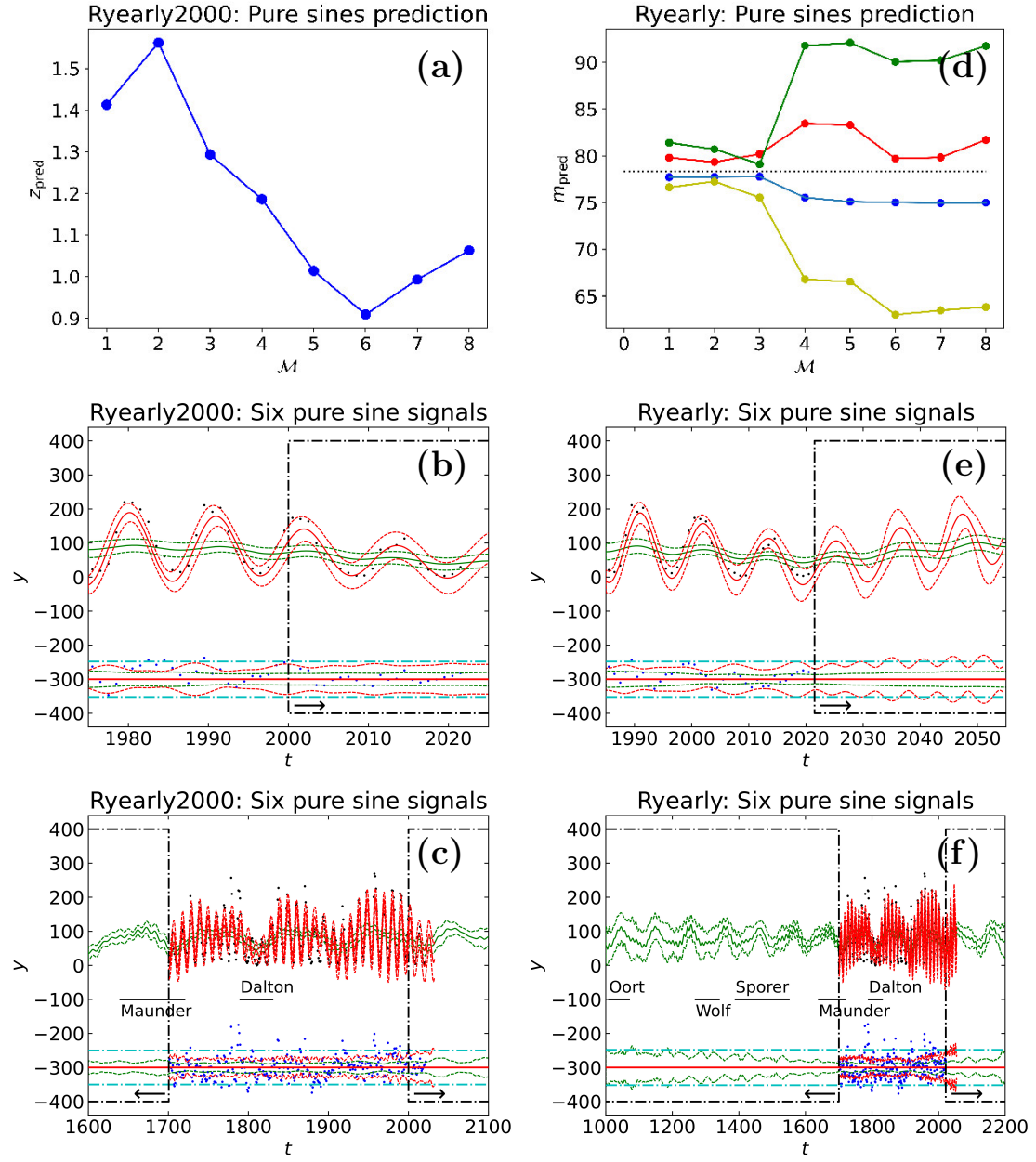


Figure 9. (a-c) Ryearly2000 predictions for pure sines (DCM-manual: Table 14). Otherwise as in Figure 6a-c. (d-f) Ryearly predictions for pure sines (DCM-manual: Table 15). Otherwise as in Figure 6d-f.

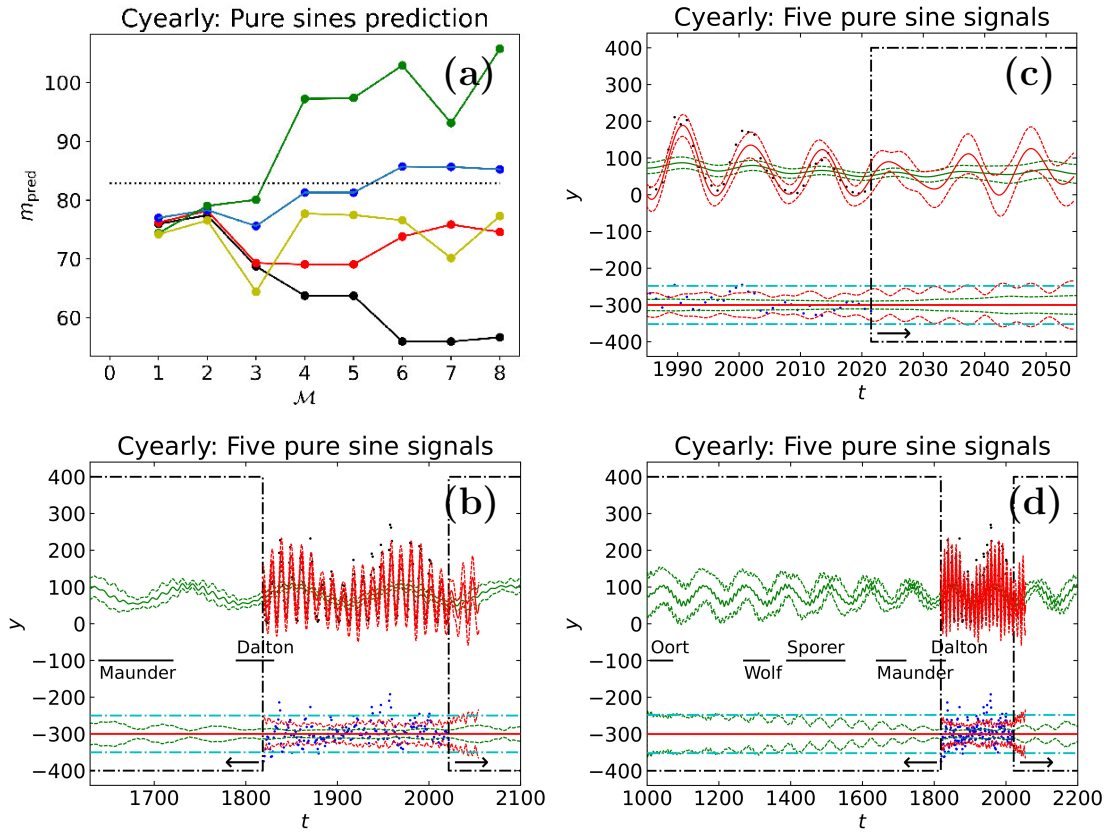


Figure 10. (a-d) Cyearly predictions (DCM-manual: Table 17). Otherwise as in Figure 8a-d.

level m_{pred} estimates for the past activity minima do not succeed. The six pure sine signal model for the next decades predicts rising solar activity (Figure 9e: green line).

6.5. Weighted yearly sunspot data

The predictive data sample is Cyearly2000. Sample Cyearly is all data, where the observations after the year 2000 are the predicted data. We study only the pure sine DCM models, because the Cyearly and Cyearly2000 samples are both too small ($n = 204$ and 182) for the DCM double wave model analysis.

We detect only two pure sine signals in the predictive data sample Cyearly2000. Additional signals give unstable models (DCM-manual: Table 16, “UM”). Therefore, no prediction is made.

Five pure sine signals are detected in all data sample Cyearly (DCM-manual: Table 17). We give the periods and amplitudes of these five signals in Table 6 (Column 13).

The pure sine signal DCM models $M=1$ -8 give the predicted mean level m_{pred} (Equation 32) values shown in Figure 10a. The black and red m_{pred} curves for the Dalton and the Maunder minima fall clearly below the mean level $m = 82.8$ of all yearly sunspot data. After this, these two curves also stay below this m level. These results are not unexpected because the Dalton and the Maunder minima are the closest activity minima before the beginning of the Cyearly sample.

The all data sample Cyearly prediction for the time intervals of the Dalton and the Maunder minima is excellent (Figure 10b: green curve). However, the prediction can not reproduce the low

Table 10. Predictions for next three sunspot cycles. (1) Sample: Figure showing predictions. (2-3) Maximum and minimum t and y of cycle 25. (4-5) Sunspot cycle 26. Otherwise as in “2-3”. (6-7) Sunspot cycle 27. Otherwise as in “2-3”. Line below each group of five estimates gives their weighted mean.

	(1)	(2)	(3)	(4)	(5)	(6)	(7)
Sample: Figure		Maximum 25		Maximum 26		Maximum 27	
		t (y)	y (-)	t (y)	y (-)	t (y)	y (-)
Rmonthly: Figure 6e	2025.86 \pm 0.16	118.4 \pm 5.9	2037.40 \pm 0.20	148.7 \pm 5.7	2048.41 \pm 0.22	170.9 \pm 5.4	
Rmonthly: Figure 7e	2024.42 \pm 0.20	88.6 \pm 4.8	2037.6 \pm 4.9	146 \pm 30	2047.9 \pm 5.1	207 \pm 18	
Cmonthly: Figure 8c	2024.07 \pm 0.19	89.4 \pm 4.1	2037.39 \pm 0.13	102.8 \pm 5.3	2047.48 \pm 0.15	116.6 \pm 5.4	
Ryearly: Figure 9e	2025.28 \pm 0.39	106 \pm 14	2036.62 \pm 0.41	145 \pm 16	2047.40 \pm 0.41	185 \pm 15	
Cyearly: Figure 10c	2024.36 \pm 0.78	90 \pm 10	2037.4 \pm 1.3	112 \pm 22	2047.5 \pm 2.0	126 \pm 21	
Weighted mean:	2024.94 \pm 0.79	95 \pm 12	2037.34 \pm 0.19	125 \pm 22	2047.72 \pm 0.41	148 \pm 30	
		Minimum 25		Minimum 26		Minimum 27	
Rmonthly: Figure 6e	2031.57 \pm 0.18	16.8 \pm 6.1	2042.82 \pm 0.20	22.4 \pm 5.5	2053.76 \pm 0.23	34.0 \pm 5.0	
Rmonthly: Figure 7e	2032.7 \pm 5.0	25 \pm 10	2043.4 \pm 5.0	6 \pm 15	2054.1 \pm 5.4	39.4 \pm 6.8	
Cmonthly: Figure 8c	2031.77 \pm 0.28	19.2 \pm 4.4	2042.35 \pm 0.14	0.3 \pm 4.4	2052.58 \pm 0.18	28.8 \pm 5.2	
Ryearly: Figure 9e	2030.77 \pm 0.38	-15 \pm 15	2041.79 \pm 0.38	16 \pm 16	2052.62 \pm 0.41	38 \pm 17	
Cyearly: Figure 10c	2031.8 \pm 1.1	16 \pm 13	2042.3 \pm 2.0	-1 \pm 19	2052.7 \pm 2.2	28 \pm 17	
Weighted mean:	2031.52 \pm 0.31	17.4 \pm 7.4	2042.44 \pm 0.29	9 \pm 10	2052.98 \pm 0.56	33.0 \pm 4.3	

number of sunspots during the Maunder minimum. The green dotted lines denoting the error of the predicted 30 years sliding mean stay well below the ISES limit denoted with cyan dash-dotted lines (Equation 42). This successful deterministic prediction for the Maunder minimum time interval covers two centuries backwards, before the beginning of the analysed data sample **Cyearly**. This time interval is about twenty times longer than the stochastic H_{Dynamo} hypothesis predictability limit of only one solar cycle. It is actually quite unexpected that only about 200 years of data can predict so well the activity mean level for the past 200 years without any data. This can succeed only if the model is correct and deterministic. It also means that our prediction for the future can be considered reliable. This **Cyearly** sample future prediction for the next decades is shown in Figure 10c. The long-term prediction indicates rising solar activity during the next half a century (Figure 10d).

Our best predictive models are very consistent because the number of signals in all models is either five (Figures 6a, 8a and 10a) or six (Figures 7a and 9a). We conclude that the results presented in Sections 6.2-6.5 confirm the predictability of sunspot numbers.

6.6. Future sunspot maxima and minima predictions

We give the predictions for the next three sunspot cycle maxima and minima in Table 10.

The lowest possible real sunspot number is zero. We can not prevent DCM from utilising negative model $g(t)$ values. For this reason, two predicted cycle minimum sunspot number estimates out of all fifteen estimates, $y = -15 \pm 15$ and $y = -1 \pm 19$, are negative (Table 10). However, in these two exceptional cases the sunspot number can be zero within $\pm 1\sigma$.

The ISES prediction for the cycle 25 maximum epoch was $t = \text{July } 2025 \pm 8.0 \text{ months} = 2025.54 \pm 0.67$. Their smoothed maximum sunspot number prediction was $y = 115$. Our predictions $t = \text{December } 2024 \pm 9.5 \text{ months} = 2024.94 \pm 0.79$ and $y = 95 \pm 12$ differ 0.76σ and 1.67σ from the ISES prediction.

Our prediction error $\pm 0.^y79$ for the cycle 25 maximum epoch is much larger than our prediction errors $\pm 0.^y19$ and $\pm 0.^y41$ for the next two maximum epochs (Table 10). This is a real statistical

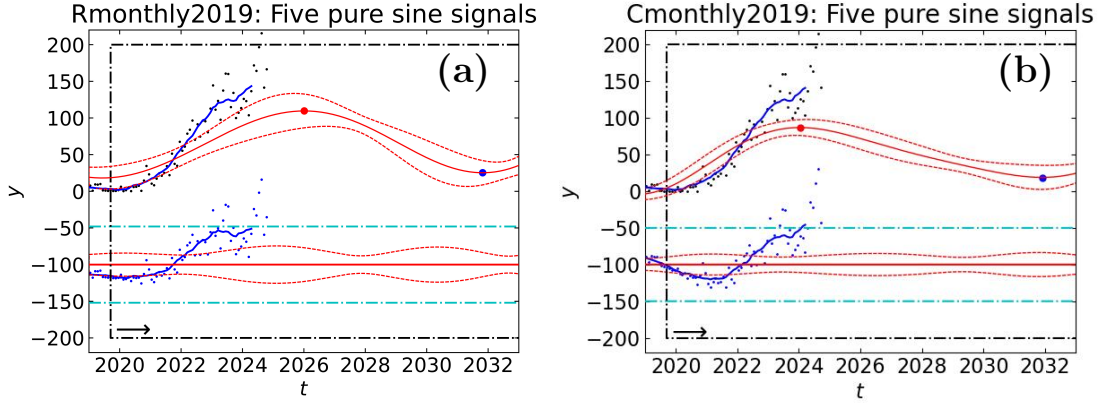


Figure 11. DCM predictions for cycle 25. (a) Nonweighted five pure sines prediction for sample Rmonthly2019 has maximum $y = 109.6 \pm 7.7$ at 2026.0 ± 0.3 (red circle) and minimum $y = 25.3 \pm 6.1$ at 2031.8 ± 4.8 (blue circle). Otherwise as in Figure 6. (b) Weighted five pure sines prediction for sample Cmonthly2019 has maximum $y = 86.9 \pm 3.8$ at $t = 2024.04 \pm 0.24$ and minimum $y = 18.9 \pm 5.3$ at $t = 2031.92 \pm 0.22$. Otherwise as in “a”.

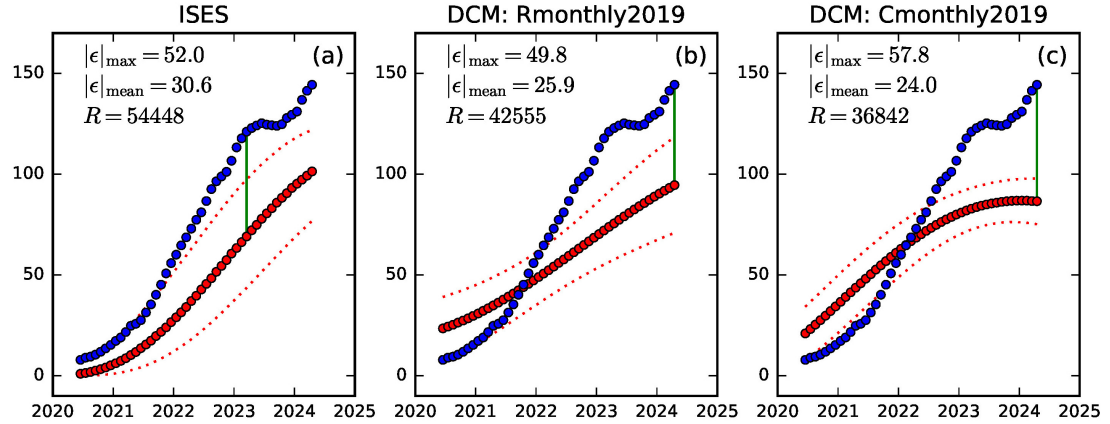


Figure 12. Comparison of predictions. (a) ISES prediction: Predicted g_{13} (red circles), observed y_{13} (blue circles) and prediction errors (red dotted curve). We give maximum of residual's absolute values ($|\epsilon|_{\max}$: green vertical line), mean of residual's absolute values ($|\epsilon|_{\text{mean}}$) and sum of squared residuals (R). (b) Rmonthly2019 prediction from Figure 11a, otherwise as in “a”. (b) Cmonthly2019 prediction from Figure 11b, otherwise as in “a”.

effect. The predicted peak of this next cycle 25 maximum is lower than, and not so sharp as, the predicted peaks of the next cycle 26 and 27 maxima (Figures 6e, 7e, 8c, 9e, and 10c).

The six double wave model predictions for the largest Rmonthly sample are not very accurate in Table 10 (Rmonthly: Figure 7e). The probable reason for this inaccuracy is the large number $\eta = 21 + 10$ of the free parameters (DCM-manual: Table 9, model $\mathcal{M}=6$). This is also the only model that has a turning point in the year 2029 (Figure 7e).

We predict that the mid-point of the next prolonged grand sunspot minimum is approximately in the year 2100 (Figures 6f, 7f, 8d, 9f and 10d: green curve).

6.7. Prediction for current sunspot cycle 25

After the analysis of all eight samples summarised in Table 5 was already completed, we were requested to give our own prediction for the ongoing cycle 25. We removed all data after September 2019 from the samples Rmonthly and Cmonthly. This gave us all data before the beginning

of cycle 25, samples $R_{\text{monthly}2019}$ and $C_{\text{monthly}2019}$. The results of the DCM analysis of these samples are presented in the DCM-manual (Tables 18 and 19).

Our DCM prediction for the $R_{\text{monthly}2019}$ sample of non-weighted monthly sunspot numbers is shown in Figure 11a. The predicted maximum and minimum epochs are January 2026 and September 2031, respectively. We show the DCM prediction for the weighted $C_{\text{monthly}2019}$ sample in Figure 11b. The maximum is at January 2024 and the minimum at November 2031.

Cycle 25 began on October 2019. The ISES panel gave no g_{13} prediction between October 2019 and May 2020. Their prediction begins from June 2020. At the moment, the last available observed y_{13} value is from April 2024.⁶ The ISES prediction for the cycle 25 maximum is July 2025. Their prediction for the cycle minimum is vague because the prediction fades extremely slowly, $0 \leq g_{13} \leq 1$ between July 2034 and April 2037 (Figure 5). Their prediction is “safe” because the next minimum is bound to occur sooner or later. Their predicted long fading period begins three years after our predicted cycle 25 minimum at the end of the year 2031.

In Figures 6-10, we can compare our predictions only to the five year ISES limit $s_{\text{ISES}} = |\epsilon|_{\text{max}} = 52$ (Equation 42). The ISES cycle 25 predictions between June 2020 and April 2024 allow us to compare the three parameters $|\epsilon|_{\text{max}}$, $|\epsilon|_{\text{mean}}$ and R (Equations 10 and 11). The ISES prediction values are $|\epsilon|_{\text{max}} = 52.0$, $|\epsilon|_{\text{mean}} = 30.6$ and $R = 54448$ (Figure 12a). Our DCM model prediction for the $R_{\text{monthly}2019}$ sample gives smaller values $|\epsilon|_{\text{max}} = 49.8$, $|\epsilon|_{\text{mean}} = 25.9$ and $R = 42555$ (Figure 12b). All three parameters indicate that our prediction is more accurate than the ISES prediction. Our DCM model prediction for the $C_{\text{monthly}2019}$ sample gives $|\epsilon|_{\text{max}} = 57.8$, $|\epsilon|_{\text{mean}} = 24.0$ and $R = 36842$ (Figure 12c). The small $|\epsilon|_{\text{mean}}$ and R values indicate that our prediction is better than the ISES prediction. However, our prediction $|\epsilon|_{\text{max}} = 57.8$ is larger than the ISES prediction $|\epsilon|_{\text{max}} = 52.0$. For the last y_{13} value in April 2024, our prediction for the $C_{\text{monthly}2019}$ sample exceeds the five year ISES limit (Figures 11b and 12c). Statistically, this prediction of ours is better than the ISES prediction because only *one* y_{13} value gives $|\epsilon|_{\text{max}}$, but *all* y_{13} values give $|\epsilon|_{\text{mean}}$ and R .

7. Discussion

In time series analysis, the detected periods are usually considered real if they have an accepted physical cause, like in the DCM analysis by Jetsu (2021). Here, such a widely accepted cause for the detected strictly periodic, extremely significant and predictive signals is missing. There must be an astrophysical mechanism that causes these signals in the sunspot data, unless both DCM and DFT give the same misleading results. Whatever this astrophysical mechanism may be, why would both of these statistical methods detect the same unreal signals? What other solar system physical mechanism can cause these signals, except the planets? This would mean that the solar cycle is not generated only by the physical mechanisms inside the Sun. The only possible external cause can be the gravitational tidal forces of planets.

Parker (1955) formulated the dynamo model, where the interaction of differential rotation and convective motion drives the solar magnetic field. The first models for a dynamo generated sunspot cycle were presented by Babcock (1961) and Leighton (1969). All dynamo model physical mechanisms causing the solar cycle are not yet fully understood (Charbonneau, 2010). As stated in our H_{Dynamo} hypothesis, it is widely accepted that the solar cycle is stochastic and unpredictable beyond one solar cycle (Petrovay, 2020). For example, the ISES panel predictions cover only the ongoing cycle (Figure 5). If these predictions were made for several cycles in a row, the prediction errors would certainly exceed the five year ISES limit (Equation 42).

⁶Accessed SILSO on 21 November 2024

Table 11. Relative tidal forces of planets (Equation 43). (1) Planet. (2) Major axis. (3) Mass. (4) Relative tidal force (Equation 43).

(1) Planet	(2) a (a_{Earth})	(3) m (m_{Earth})	(4) R_{Tidal} (-)
Mercury	0.39	0.055	0.95
Venus	0.72	0.82	2.16
Earth	1.00	1.00	1.00
Mars	1.52	0.11	0.030
Jupiter	5.20	318	2.26
Saturn	9.53	95.3	0.11
Uranus	19.2	14.5	0.0020
Neptune	30.1	17.3	0.00063

Recently, several attempts have been made to model an internal solar dynamo influenced by external gravitational tidal forces of planets. Stefani, Giesecke, and Weier (2019) presented a solar dynamo, where the planetary tidal forcing causes periodic 11.07 and 22.14-year magnetic field oscillations. Scafetta and Bianchini (2022) reviewed the possible physical mechanisms that could explain how the weak planetary tidal forces can alter the solar structure and cause the sunspot cycle. Charbonneau (2022) showed that if the external planetary signal is not constantly amplified, the internal solar dynamo mechanism fluctuations can mask this external signal. More recently, Cionco, Kudryavtsev, and Soon (2023) argued that the combined tidal forcing of Venus, the Earth and Jupiter can not cause the 11-years solar cycle.

The mass m_E and the major axis a_E of Earth give the dimensionless relative tidal force

$$R_{\text{Tidal}} = \frac{m}{m_E} \left(\frac{a_E}{a} \right)^3, \quad (43)$$

exerted by each planet to the Sun, where the planet's mass is m and its major axis is a . The tidal forces of Venus and Jupiter are much stronger than those of the Earth and Mercury (Table 11). The tidal forces of Mars, Saturn, Neptune and Uranus are negligible. Therefore, we will search for the orbital periods of Mercury (P_M), Venus (P_V), Earth (P_E) and Jupiter (P_J), the synodic periods of two planets ($P_{M,V}$, $P_{M,E}$, $P_{M,J}$, $P_{V,E}$, $P_{V,J}$, $P_{E,J}$), and the synodic periods of three planets ($P_{M,V,E}$, $P_{M,V,J}$, $P_{V,M,J}$). Only one of these periods, P_J , is inside the period interval between 5 and 200 years, where DCM detects periodicity (Section 4.1). All other orbital periods are shorter than 5 years. DCM detects no such shorter periods (Section 4.2).

The S_{11y} , S_{10y} , $S_{11.y86}$, S_{110y} and $S_{10.y6}$ signals are the strongest ones (Table 6). Since these five signals are clearly connected (Table 8), their interference is repeated indefinitely, as long as the orbital periods of the involved planets remain constant. For example, the R_{monthly} sample $n = 3287$ observations have $m = 81.6$ and $s = 67.7$. Only twenty y_i values exceed $m + 3s = 285$. The best model for this sample, the sum of five pure sine signals, has the mean level $M_0 = 81.3 \pm 0.8$. The sum of the peak to peak amplitudes for these five strongest S_{11y} , S_{10y} , $S_{11.y86}$, S_{110y} and $S_{10.y6}$ signals is $A_{11y} + A_{10y} + A_{11y.86} + A_{110y} + A_{10y.6} = 331$ (Table 6: column 2). These five signals alone can reproduce the whole range of observed y_i changes. No additional signals are needed. The interference of S_{11y} and S_{10y} signals can cause the S_{110y} signal (Table 8). After this, the interference of $S_{11.y86}$ and S_{110y} signals can cause the $S_{10.y6}$ signal. Hence, the

Table 12. Three strongest signals in all data samples. (1) Sample: $K_2 = 1$ or 2 model. (2) Signal S_{11y} : Period P_{11y} and amplitude A_{11y} . (3-4) Same for S_{10y} and $S_{11,y86}$ signals. Lowest line gives period and amplitude weighted means. Note that S_{10y} signal in Rmonthly: $K_2 = 2$ is a double sinusoid^{2×}.

	(1)	(2)	(3)	(4)
Sample: K_2		S_{11y} P_{11} (y) A_{11} (-)	S_{10y} P_{10} (y) A_{10} (-)	$S_{11,y86}$ $P_{11.86}$ (y) $A_{11.86}$ (-)
Rmonthly: $K_2 = 1$		11.0033 ± 0.0064 101.5 ± 2.5	10.0001 ± 0.0081 65.5 ± 2.1	11.807 ± 0.012 56.4 ± 2.4
Rmonthly: $K_2 = 2$		10.9878 ± 0.0051 104.6 ± 2.3	$10.0031 \pm 0.0044^{2\times}$ 75.2 ± 2.7	11.770 ± 0.011 62.7 ± 2.6
Cmonthly: $K_2 = 1$		10.8585 ± 0.0048 117.5 ± 2.9	10.0658 ± 0.0077 59.3 ± 2.8	11.863 ± 0.021 43.3 ± 2.0
Ryearly: $K_2 = 1$		10.981 ± 0.020 98.3 ± 7.8	9.975 ± 0.017 62.8 ± 6.1	11.820 ± 0.027 40.5 ± 3.3
Cyearly: $K_2 = 1$		10.863 ± 0.022 119.3 ± 7.5	10.058 ± 0.026 61.0 ± 9.6	11.856 ± 0.068 43.8 ± 7.9
Weighted mean		10.938 ± 0.066 107.0 ± 6.8	10.014 ± 0.026 66.3 ± 5.8	11.799 ± 0.031 50.5 ± 8.6

S_{11y} , S_{10y} and $S_{11,y86}$ signals may be the only real ones. We give the weighted mean periods and amplitudes of these three strongest signals in Table 12.

7.1. Integer multiples of one planet orbital period

The third strongest $S_{11,y86}$ signal has $P_{11,y86} = 11.799 \pm 0.031$ years weighted mean period. It differs 1.9σ from the $1 \times P_J = 11.857$ years period. The orbital periods P_M , P_V and P_E are shorter than 5 years. These periods can not be found *directly* from the monthly sunspot data (Section 4.2). This does not, however, mean that we can not search for multiples of these periods above the five year limit $P_{\max} = 5$. These periods iP_{Planet} are called “integer multiple orbital periods”, where P_{Planet} is planet’s orbital period and $i = 1, 2, 3\dots$ is the “integer multiplier”. The aim is to find those integer multipliers that give the detected signal periods. The weighted mean $P_{11y} = 10.938 \pm 0.066$ years period of the strongest S_{11y} signal differs 0.94σ from $11 \times P_E$. The weighted mean $P_{10y} = 10.014 \pm 0.026$ years period of the second strongest S_{10y} signal differs 0.54σ from $10 \times P_E$.

We use the known planet orbital period $P_{\text{Planet}} = P_M, P_V, P_E$ and P_J in Earth years to compute four dimensionless parameters

$$\mathcal{P} = P/P_{\text{Planet}} \quad (44)$$

$$\sigma_{\mathcal{P}} = \sigma_P/P_{\text{Planet}} \quad (45)$$

$$\Delta\mathcal{P} = \mathcal{P} - \mathcal{P}_0 \quad (46)$$

$$\Delta\mathcal{P}_{\text{rel}} = \frac{|\Delta\mathcal{P}|}{\sigma_{\mathcal{P}}}, \quad (47)$$

where \mathcal{P}_0 is the integer value closest to \mathcal{P} . The two first parameters $\sigma_{\mathcal{P}}$ and \mathcal{P} are hereafter called “rounds error” and “rounds” (number of planet revolutions around the Sun). The next two parameters $\Delta\mathcal{P}$ and $\Delta\mathcal{P}_{\text{rel}}$ are called “rounds deviation” and “relative rounds deviation”.

Table 13. Synodic period integer multiples. (1) Synodic period P_{Syn} . (2-5) Signal S_{11y} : \mathcal{P} (Equation 44), \mathcal{P}_0 (Equation 46), $\mathcal{P}_0 P_{\text{Syn}}$ and $\sigma = (\mathcal{P}_0 P_{\text{Syn}} - P)/\sigma_P$. (6-9) Signal S_{10y} values. (10-13) Signal $S_{11,y86}$ values.

P_{Syn} (y)	(1) S_{11y} ($P = 10.938 \pm 0.066$)				(6) S_{10y} ($P = 10.014 \pm 0.026$)				(10) $S_{11,y86}$ ($P = 11.799 \pm 0.031$)			
	\mathcal{P}	\mathcal{P}_0	$\mathcal{P}_0 P_{\text{Syn}}$	σ	\mathcal{P}	\mathcal{P}_0	$\mathcal{P}_0 P_{\text{Syn}}$	σ	\mathcal{P}	\mathcal{P}_0	$\mathcal{P}_0 P_{\text{Syn}}$	σ
	(-)	(-)	(y)	(σ_P)	(-)	(-)	(y)	(σ_P)	(-)	(-)	(y)	(σ_P)
$P_{M,V} = 0.3957$	27.6	28	11.079	2.1	25.3	25	9.892	4.7	29.8	30	11.870	2.3
$P_{M,E} = 0.3172$	34.5	34	10.784	2.3	31.6	32	10.150	5.2	37.2	37	11.736	2.0
$P_{M,J} = 0.2458$	44.5	45	11.061	1.9	40.7	41	10.077	2.4	48.0	48	11.798	0.0
$P_{V,E} = 1.5988$	6.8	7	11.191	3.8	6.3	6	9.593	16.2	7.4	7	11.191	19.6
$P_{V,J} = 0.6489$	16.9	17	11.031	1.4	15.4	15	9.733	10.8	18.2	18	11.680	3.9
$P_{E,J} = 1.0921$	10.0	10	10.921	0.3	9.2	9	9.829	7.1	10.8	11	12.013	6.9

Note that we introduce a new letter “ \mathcal{P} ” to highlight the difference from the period letter “ P ”. We present the tedious search for the integer multiple orbital periods in the Appendix (Section A). The two main results are

1. The P_E and P_J integer multiples are easier to detect than the P_M and P_V integer multiples.
2. The $S_{11,y86}$ signal can be connected to Jupiter’s orbital motion (Section A.6.2).

7.2. Integer multiples of two planet synodic period

The strongest S_{11y} signal period of $P_{11y} \pm \sigma_P = 10.938 \pm 0.066$ years differs only 0.3σ from the synodic period multiple $10 \times P_{E,J} = 10.921$ years (Table 13). The ratio $P_{E,J}/\sigma_P = 16.5$ indicates that this $\sigma = 0.3$ for $P_{E,J}$ is significant. The ratio $P_{V,J}/\sigma_P = 9.8$ indicates that the $\sigma = 1.4$ value for $17 \times P_{V,J}$ can be significant. These two results indicate that $P_{E,J}$ and $P_{V,J}$ periods can be connected to the strongest S_{11y} signal. However, the ratios $P_{M,V}/\sigma_P = 6.0$, $P_{M,E}/\sigma_P = 4.8$ and $P_{M,J}/\sigma_P = 3.7$ mean that the respective $\sigma = 2.1, 2.3$ and 1.9 values for $P_{M,V}$, $P_{M,E}$ and $P_{M,J}$ multiples are not significant. This illustrates the effect that short period multiples are more difficult to detect (Appendix: Equations 50 and 54).

For the second strongest S_{10y} signal, the $P_{10y} \pm \sigma_P = 10.014 \pm 0.026$ years period differs 2.4σ from $41 \times P_{M,J}$ (Table 13). The ratio $P_{M,J}/\sigma_P = 9.4$ indicates that this result may be significant. All integer multiples for the other synodic periods $P_{M,V}$, $P_{M,E}$, $P_{V,E}$, $P_{V,J}$ and $P_{E,J}$ differ more than $\pm 3\sigma$ from the S_{10y} signal period.

The third strongest $S_{11,y86}$ signal period of $P_{11,y86} \pm \sigma_P = 10.938 \pm 0.031$ years differs 2.3σ , 2.0σ and 0.0σ from $30 \times P_{M,V}$, $37 \times P_{M,E}$ and $48 \times P_{M,J}$, respectively. The ratios $P_{M,V}/\sigma_P = 12.8$, $P_{M,E}/\sigma_P = 10.2$ and $P_{M,J}/\sigma_P = 7.9$ indicate that all these the synodic period multiples may be connected to the $S_{11,y86}$ signal period.

7.3. Synodic periods for three planets

We use the algorithm formulated by Borisov (2012) to search for the synodic periods of three planets. The periods of these three planets are $P_1 < P_2 < P_3$. Their synodic periods are P_{12} , P_{13} and P_{23} . The resonance of these three planets requires

$$\frac{P_{12}}{P_{23}} = \frac{i}{j}, \quad (48)$$

Table 14. Three planet synodic periods. (1-2) Integers i and j (Equations 48 and 49). (3-5) Two planet synodic periods P_{12} , P_{13} and P_{23} (Equations 48 and 49). (6) Three planet synodic period P_{123} (Equation 49)

(1)	(2)	(3)	(4)	(5)	(6)
i	j	P_{12}	P_{13}	P_{23}	P_{123}
(-)	(-)	(y)	(y)	(y)	(y)
Mercury, Venus, Earth					
7	28	$P_{M,V} = 0.396$	$P_{M,E} = 0.317$	$P_{V,E} = 1.599$	$P_{M,V,E} = P_{7,28} = 11.101$
Mercury, Venus, Jupiter					
8	13	$P_{M,V} = 0.396$	$P_{M,J} = 0.246$	$P_{V,J} = 0.649$	$P_{M,V,J} = P_{8,13} = 5.162$
11	18	$P_{M,V} = 0.396$	$P_{M,J} = 0.246$	$P_{V,J} = 0.649$	$P_{M,V,J} = P_{11,18} = 7.128$
14	23	$P_{M,V} = 0.396$	$P_{M,J} = 0.246$	$P_{V,J} = 0.649$	$P_{M,V,J} = P_{14,23} = 9.094$
17	28	$P_{M,V} = 0.396$	$P_{M,J} = 0.246$	$P_{V,J} = 0.649$	$P_{M,V,J} = P_{17,28} = 11.061$
19	31	$P_{M,V} = 0.396$	$P_{M,J} = 0.246$	$P_{V,J} = 0.649$	$P_{M,V,J} = P_{19,31} = 12.290$
Venus, Earth, Jupiter					
6	4	$P_{V,E} = 1.599$	$P_{V,J} = 0.649$	$P_{E,J} = 1.092$	$P_{M,V,J} = P_{6,4} = 6.489$
9	6	$P_{V,E} = 1.599$	$P_{V,J} = 0.649$	$P_{E,J} = 1.092$	$P_{M,V,J} = P_{9,6} = 9.733$
13	9	$P_{V,E} = 1.599$	$P_{V,J} = 0.649$	$P_{E,J} = 1.092$	$P_{M,V,J} = P_{13,9} = 14.275$
16	11	$P_{V,E} = 1.599$	$P_{V,J} = 0.649$	$P_{E,J} = 1.092$	$P_{M,V,J} = P_{16,11} = 17.519$
19	13	$P_{V,E} = 1.599$	$P_{V,J} = 0.649$	$P_{E,J} = 1.092$	$P_{M,V,J} = P_{19,13} = 20.764$

where $i, j = 1, 2, 3, \dots$ are integers. The synodic period of these three planets is

$$P_{i,j} = (i + j)P_{13}. \quad (49)$$

Borisov (2012) presented the algorithm for solving the best values for the integers i and j . We compute the three planet synodic periods $P_{i,j} > 5$ years for $i \leq 20$ (Table 14).

The only suitable three planet synodic period for Mercury, Venus and the Earth is $P_{M,V,E} = P_{7,28} = 11.101$, which differs 2.5σ from $P = 10.938 \pm 0.066$ of S_{11y} signal.

For Mercury, Venus and Jupiter, the $P_{M,V,J} = P_{17,28} = 11.061$ period differs 1.9σ from signal S_{11y} period $P = 10.938 \pm 0.066$. None of the other three planet synodic periods $P_{M,V,J} = P_{8,13}$, $P_{11,18}$, $P_{14,23}$ and $P_{19,31}$ is close to the S_{11y} , S_{10y} or $S_{11,y86}$ signal periods.

For Venus, the Earth and Jupiter, all five synodic periods $P_{V,M,J} = P_{6,4}$, $P_{9,6}$, $P_{13,3}$, $P_{16,11}$ and $P_{19,13}$ are far from the S_{11y} , S_{10y} and $S_{11,y86}$ signal periods.

In short, the S_{11y} signal connects to eight (P_E , $P_{M,V}$, $P_{M,E}$, $P_{M,J}$, $P_{V,J}$, $P_{E,J}$, $P_{M,V,E}$, $P_{M,V,J}$), the S_{10y} signal to two (P_E , $P_{M,J}$) and the $S_{11,y86}$ signal to four (P_J , $P_{M,V}$, $P_{M,E}$, $P_{M,J}$) periods. This would explain why the S_{11y} signal is stronger than the S_{10y} and $S_{11,y86}$ signals.

The two strongest S_{11y} and S_{10y} signal periods are close to P_J , and the third strongest $S_{11,y86}$ signal period is nearly equal to P_J . This indicates that Jupiter's role is pronounced.

We present direct observational evidence that these detected signals in the sunspot data can be connected to the planetary motions. It is possible that the planetary motions can influence the solar cycle, but it is impossible that the solar magnetic field can influence the planetary motions. As far as we know, ours would be the first *direct* detection of planets from the sunspot data.

Astrophysical theories are used to construct models of astronomical phenomena. Observations are used to test these models. Statistical methods are not confined to any particular phenomenon. The same statistical method can be applied to different phenomena. No phenomenon can fool statistics. Our statistical DCM can detect combinations of phenomena that are repeated (Equation 6: $h(t)$) and not repeated (Equation 8: $p(t)$). Phenomena are not stochastic only

because they appear unpredictable. Phenomena may appear stochastic because we can not yet predict them. Both DCM and DFT detect the same extremely significant and strictly periodic signals that can predict sunspot data. This does not support the mainstream dynamo-influence-theory H_{Dynamo} hypothesis of a stochastic sunspot cycle. From the time series analysis point of view, this is a clear-cut case. Our results support the deterministic planetary-influence-theory H_{Planet} hypothesis.

8. Conclusions

The sunspot cycle is claimed to be stochastic according to the mainstream dynamo models. Our Discrete Chi-square Method (DCM) and the Discrete Fourier Transform (DFT) detect the same extremely significant and strictly periodic signals from the sunspot data. These signal detections are absolutely certain. This confirms that the sunspot cycle is deterministic, not stochastic. The three strongest detected S_{11y} , S_{10y} and $S_{11.y86}$ signals, together with their interference S_{110y} and $S_{10.y6}$ signals, can reproduce the full scale of all observed sunspot number variations.

Our DCM models give better sunspot cycle predictions than the official Solar Cycle Panel. Although the analysed sunspot data does not cover the past prolonged activity minima, the DCM models can predict some of these events, like the Maunder minimum. The predictability of solar activity will allow us to prepare better for the climate change on the Earth and the catastrophic geomagnetic storms, like the Carrington event in the year 1859.

The detected strictly periodic signals show connections to the orbital motions of Mercury, Venus, the Earth and Jupiter. If the planets cause the sunspot cycle, the starspot cycles observed in other chromospherically active stars may represent indirect evidence for the presence of exoplanets.

Appendix

A. Statistics for planetary signal identification

This Appendix describes the statistics of integer multiple orbital period identification. We will show that it is difficult to identify the integer multiple orbital periods of Mercury and Venus from the sunspot data. These identifications are easier for the Earth and Jupiter. The connections between these integer multiple orbital periods and the planetary motions are also discussed.

Before we begin the search for integer multiple orbital periods, the following possible misunderstandings must be corrected. Firstly, all detected signals are already given in Table 6. We are not fitting multiples of planetary signals into the data. Secondly, the identification of these multiples is not numerology. We are only trying to identify the most obvious multiples that could be connected to the planets.

We have introduced the following nine signal abbreviations S_{11y} , S_{10y} , $S_{11.y86}$, S_{110y} , $S_{10.y6}$, $S_{8.y4}$, S_{53y} , S_{8y} and S_{66y} in Table 6, where these signals were arranged in the order of decreasing strength, or equivalently, decreasing signal amplitude. The numerical value given in the signal subscript refers to the approximate signal period in Earth years.

These nine signals are now rearranged into the order of increasing periods S_{8y} , $S_{8.y4}$, S_{10y} , $S_{10.y6}$, S_{11y} , $S_{11.y86}$, S_{53y} , S_{66y} and S_{110y} in our next Tables 15 and 16. We study only the signals detected in all data samples, because we get the same results for the predictive data samples (i.e., the subsets of all data samples). We select only those all data samples, where DCM detects more than two signals. The period (P), the primary minimum epoch ($t_{\min,1}$) and the primary

Do the exoplanets cause the starspot cycles?

Table 15. Signals detected in all data samples. (1) Signal parameters. (2-6) Samples: pure sine model ($K_2 = 1$) and double wave models ($K_2 = 2$). Three double sinusoid signals are denoted with “ $2\times$ ”. Notes below give detailed instructions of how to read column (1) signal parameters.

(1)	(2) Rmonthly: $K_2 = 1$	(3) Rmonthly: $K_2 = 2$	(4) Cmonthly: $K_2 = 1$	(5) Ryearly: $K_2 = 1$	(6) Cyearly: $K_2 = 1$
Signal $S_{8y} \cong 13 \times P_V \cong 8 \times P_E$					
Rank	(7)	(8)	(5)		(5)
P	8.1087 ± 0.0076	8.169 ± 0.014	8.009 ± 0.017		8.005 ± 0.058
$t_{\min,1}$	1751.29 ± 0.14	1750.90 ± 0.51	1818.07 ± 0.24		1826.09 ± 0.68
$t_{\max,1}$	1755.34 ± 0.14	1754.37 ± 0.26	1822.08 ± 0.24		1822.09 ± 0.70
P/P_M	33.674 ± 0.032	33.924 ± 0.058	33.260 ± 0.070		33.24 ± 0.24
P/P_V	13.180 ± 0.012	13.279 ± 0.023	13.018 ± 0.028		13.012 ± 0.094
P/P_J	0.68359 ± 0.00064	0.6887 ± 0.0012	0.6752 ± 0.0014		0.6748 ± 0.0049
Signal $S_{8,y4} \cong 35 \times P_M$					
Rank		(6)		(7)	
P		$16.753 \pm 0.027^{2\times}$		8.466 ± 0.016	
$t_{\min,1}$		1759.19 ± 0.23		1707.10 ± 0.35	
$t_{\max,1}$		1754.70 ± 0.26		1702.86 ± 0.35	
P/P_M		$69.57 \pm 0.11^{2\times}$		35.158 ± 0.066	
P/P_V		$27.232 \pm 0.044^{2\times}$		13.761 ± 0.026	
P/P_J		$1.4123 \pm 0.0023^{2\times}$		0.7137 ± 0.0013	
Signal $S_{10y} \cong 41.5 \times P_M \cong 10 \times P_E$					
Rank	(2)	(2)	(2)	(2)	(2)
P	10.0001 ± 0.0081	$20.0062 \pm 0.0088^{2\times}$	10.0659 ± 0.0077	9.975 ± 0.017	10.058 ± 0.026
$t_{\min,1}$	1754.16 ± 0.11	1754.284 ± 0.063	1823.52 ± 0.12	1704.63 ± 0.35	1823.55 ± 0.25
$t_{\max,1}$	1749.16 ± 0.11	1749.282 ± 0.067	1818.48 ± 0.12	1709.62 ± 0.34	1818.52 ± 0.26
P/P_M	41.529 ± 0.034	$83.082 \pm 0.036^{2\times}$	41.802 ± 0.032	41.424 ± 0.070	41.77 ± 0.11
P/P_V	16.255 ± 0.013	$32.520 \pm 0.014^{2\times}$	16.362 ± 0.012	16.214 ± 0.028	16.349 ± 0.042
P/P_J	0.84304 ± 0.00068	$1.68658 \pm 0.00074^{2\times}$	0.84858 ± 0.00065	0.8409 ± 0.0014	0.8479 ± 0.0022
Signal $S_{10,y6} \cong 44 \times P_M$					
Rank	(5)	(5)		(3)	
P	10.569 ± 0.020	10.5407 ± 0.0060		10.659 ± 0.031	
$t_{\min,1}$	1753.03 ± 0.27	1754.40 ± 0.13		1709.27 ± 0.44	
$t_{\max,1}$	1758.31 ± 0.26	1758.307 ± 0.091		1703.94 ± 0.46	
P/P_M	43.891 ± 0.083	43.774 ± 0.025		44.26 ± 0.13	
P/P_V	17.180 ± 0.032	17.1338 ± 0.0098		17.326 ± 0.050	
P/P_J	0.89100 ± 0.0017	0.88861 ± 0.00050		0.8986 ± 0.0026	
Signal $S_{11y} \cong 11 \times P_E$					
Rank	(1)	(1)	(1)	(1)	(1)
P	11.0033 ± 0.0064	10.9878 ± 0.0051	10.8585 ± 0.0048	10.981 ± 0.020	10.863 ± 0.022
$t_{\min,1}$	1755.897 ± 0.076	1756.678 ± 0.077	1823.580 ± 0.053	1700.86 ± 0.24	1823.56 ± 0.20
$t_{\max,1}$	1750.395 ± 0.078	1750.262 ± 0.087	1818.150 ± 0.055	1706.35 ± 0.23	1828.99 ± 0.19
P/P_M	45.695 ± 0.026	45.630 ± 0.021	45.093 ± 0.020	45.602 ± 0.083	45.112 ± 0.091
P/P_V	17.886 ± 0.010	17.8605 ± 0.0083	17.6504 ± 0.0078	17.849 ± 0.032	17.658 ± 0.036
P/P_J	0.92761 ± 0.00054	0.92630 ± 0.00043	0.91540 ± 0.00040	0.9257 ± 0.0017	0.9158 ± 0.0018
Signal $S_{11,y86} \cong 49 \times P_M \cong 1 \times P_J$					
(3)	(4)	(4)	(5)	(4)	
P	11.806 ± 0.012	11.770 ± 0.011	11.863 ± 0.021	11.820 ± 0.027	11.856 ± 0.068
$t_{\min,1}$	1760.33 ± 0.13	1749.51 ± 0.15	1818.92 ± 0.20	1701.01 ± 0.41	1818.95 ± 0.69
$t_{\max,1}$	1754.42 ± 0.14	1754.40 ± 0.21	1824.85 ± 0.19	1706.92 ± 0.41	1824.88 ± 0.66
P/P_M	49.028 ± 0.050	48.879 ± 0.046	49.265 ± 0.087	49.09 ± 0.11	49.24 ± 0.28
P/P_V	19.190 ± 0.020	19.132 ± 0.018	19.283 ± 0.034	19.213 ± 0.044	19.27 ± 0.11
P/P_J	0.9953 ± 0.0010	0.99224 ± 0.00093	1.0001 ± 0.0018	0.9964 ± 0.0023	0.9995 ± 0.0057
Signal $S_{53y} \cong 4.5 P_J$					
Rank	(6)			(6)	
P	52.66 ± 0.27			53.83 ± 0.76	
$t_{\min,1}$	1759.63 ± 0.70			1704.5 ± 2.7	
$t_{\max,1}$	1785.94 ± 0.60			1731.4 ± 2.3	
P/P_M	218.7 ± 1.1			223.5 ± 3.2	
P/P_V	85.60 ± 0.44			87.5 ± 1.2	
P/P_J	4.439 ± 0.023			4.538 ± 0.064	
Signal $S_{66y} \cong 5.5 \times P_J$ or $6.0 \times P_J$					
Rank		(7)		(8)	
P		$143.39 \pm 0.99^{2\times}$		66.7 ± 1.4	
$t_{\min,1}$		1887.84 ± 0.80		1753.0 ± 3.8	
$t_{\max,1}$		1784.2 ± 1.1		1719.6 ± 4.4	
P/P_M		$595.5 \pm 4.1^{2\times}$		277.0 ± 5.8	
P/P_V		$233.1 \pm 1.6^{2\times}$		108.4 ± 2.3	
P/P_J		$12.088 \pm 0.083^{2\times}$		5.62 ± 0.12	
Signal $S_{110y} \cong \text{Synodic periods of Equation 40 (Table 8)}$					
(4)	(3)	(3)	(4)	(3)	
P	99.92 ± 0.57	104.23 ± 0.68	116.7 ± 1.3	101.4 ± 2.4	115.6 ± 3.6
$t_{\min,1}$	1811.99 ± 0.84	1811.37 ± 0.68	1911.02 ± 0.74	1710.5 ± 3.4	1910.4 ± 2.1
$t_{\max,1}$	1762.0 ± 1.1	1844.00 ± 0.48	1852.7 ± 1.1	1761.2 ± 2.5	1852.6 ± 2.6
P/P_M	415.0 ± 2.4	432.8 ± 2.8	484.6 ± 5.4	421 ± 10	480 ± 15
P/P_V	162.42 ± 0.93	169.4 ± 1.1	189.7 ± 2.1	164.8 ± 3.9	187.9 ± 5.8
P/P_J	8.424 ± 0.048	8.787 ± 0.057	9.84 ± 0.11	8.55 ± 0.20	9.74 ± 0.30

Notes. Column 1 specifies seven parameters for each sample. For example, seventh strongest “(7)” signal S_{8y} for Rmonthly ($K_2 = 1$) has period $P \pm \sigma_P = 8.1087 \pm 0.0076$ in Earth years. Primary minima and maxima of this signal are at years $t_{\min,1} = 1751.29 \pm 0.14$ and $t_{\max,1} = 1755.34 \pm 0.14$. Rounds $P \pm \sigma_P$ values are $(P \pm \sigma_P)/P_M = 33.674 \pm 0.032$, $(P \pm \sigma_P)/P_V = 13.180 \pm 0.012$ and $(P \pm \sigma_P)/P_J = 0.68359 \pm 0.00064$.

Table 16. Detected planetary signal candidates. (1) Sample ($K_2 = 1 \equiv$ pure sine model, $K_2 = 2 \equiv$ double wave model), (2) Time span. (3) Period. (4) Rounds (Equations 44 and 45). (5) Rounds deviation (Equation 46). (6) Relative rounds deviation (Equation 47). (7) Mean anomaly migration $\Delta M/360^\circ$ (Equation 54). (8) Planet revolutions during ΔT . (9) Relative mean anomaly migration $\Delta M/360^\circ$ (Equation 55). (10) Displaying figure and symbol colour.

(1) Sample (K_2)	(2) ΔT (y)	(3) $P \pm \sigma_P$ (y)	(4) $\mathcal{P} \pm \sigma_{\mathcal{P}}$ (-)	(5) $\Delta \mathcal{P}$ (-)	(6) $\Delta \mathcal{P}_{\text{rel}}$ (-)	(7) $\frac{\Delta M}{360^\circ}$ (-)	(8) $\frac{\Delta T}{P_{\text{Planet}}}$ (-)	(9) $\frac{\Delta M_{\text{rel}}}{360^\circ}$ (-)	(10) Figure
Signal $S_{8y} : \cong 13 \times P_V$									
Rmonthly($K_2 = 1$)	273.8	8.1087 ± 0.0076	13.180 ± 0.012	0.180	15.0	6.1	445	0.014	13a: red
Rmonthly($K_2 = 2$)	273.8	8.169 ± 0.014	13.279 ± 0.023	0.279	12.1	9.4	445	0.021	13a: blue
Cmonthly($K_2 = 1$)	204.8	8.009 ± 0.017	13.018 ± 0.028	0.018	0.90	0.46	333	0.0014	13a: green
Cyearly($K_2 = 1$)	203.0	8.005 ± 0.058	13.012 ± 0.094	0.012	0.13	0.30	330	0.00092	13a: cyan
Signal $S_{8y} : \cong 8 \times P_E$									
Rmonthly($K_2 = 1$)	273.8	8.1087 ± 0.0076	8.1087 ± 0.0076	0.1087	14.3	3.7	273.8	0.013	13b: red
Rmonthly($K_2 = 2$)	273.8	8.169 ± 0.014	8.169 ± 0.014	0.169	12.1	5.7	273.8	0.021	13b: blue
Cmonthly($K_2 = 1$)	204.8	8.009 ± 0.017	8.009 ± 0.017	0.009	0.53	0.23	204.8	0.0011	13b: green
b Cyearly($K_2 = 1$)	203.0	8.005 ± 0.058	8.005 ± 0.058	0.005	0.086	0.13	203.0	0.00062	13b: cyan
Signal $S_{8,y4} : \cong 35 \times P_M$									
Ryearly($K_1 = 1$)	321.0	8.466 ± 0.16	35.158 ± 0.066	0.158	2.4	6.0	1333	0.0045	None
Signal $S_{10y} : 41.5 \times P_M$									
Rmonthly($K_2 = 1$)	273.8	10.0001 ± 0.0081	41.529 ± 0.034	0.029	0.85	0.79	1137	0.00070	13c: red
Cmonthly($K_2 = 1$)	204.8	10.0659 ± 0.0077	41.802 ± 0.032	0.302	9.4	6.2	851	0.0072	13c: green
Ryearly($K_2 = 1$)	321.0	9.975 ± 0.017	41.424 ± 0.070	-0.076	1.1	-2.4	1333	0.0018	13c: yellow
Cyearly($K_2 = 1$)	203.0	10.058 ± 0.026	41.77 ± 0.11	0.27	2.4	5.4	843	0.0065	13c: cyan
Signal $S_{10y} : \cong 10.0 \times P_E$									
Rmonthly($K_2 = 1$)	273.8	10.0001 ± 0.0081	10.0001 ± 0.0081	0.0001	0.012	0.0027	273.8	0.000010	13d: red
Cmonthly($K_2 = 1$)	204.8	10.0659 ± 0.0077	10.0659 ± 0.0077	0.0659	8.6	1.3	204.8	0.0065	13d: green
Ryearly($K_2 = 1$)	321.0	9.975 ± 0.017	9.975 ± 0.017	-0.025	1.5	-0.80	321	0.0025	13d: yellow
Cyearly($K_2 = 1$)	203.0	10.058 ± 0.026	10.058 ± 0.026	0.058	2.3	1.2	203	0.0058	13d: cyan
Signal $S_{10,y6} : \cong 44 \times P_M$									
Rmonthly($K_2 = 1$)	273.8	10.569 ± 0.020	43.891 ± 0.083	-0.109	1.3	-2.8	1137	0.0025	14a: red
Rmonthly($K_2 = 2$)	273.8	10.5407 ± 0.0060	43.774 ± 0.025	-0.226	9.0	-5.9	1137	0.0052	14a: blue
Ryearly($K_2 = 1$)	321.0	10.659 ± 0.031	44.26 ± 0.13	0.26	2.0	7.8	1333	0.0059	14a: yellow
Signal $S_{11y} : \cong 11.0 \times P_E$									
Rmonthly($K_2 = 1$)	273.8	11.0033 ± 0.0064	11.0033 ± 0.0064	0.0033	0.52	0.082	273.8	0.00030	14b: red
Rmonthly($K_2 = 2$)	273.8	10.9878 ± 0.0051	10.9878 ± 0.0051	-0.0122	2.4	-0.30	273.8	0.0011	14b: blue
Cmonthly($K_2 = 1$)	204.8	10.8585 ± 0.0048	10.8585 ± 0.0048	-0.1415	29	-2.7	204.8	0.013	14b: green
Ryearly($K_2 = 1$)	321.0	10.981 ± 0.020	10.981 ± 0.020	-0.019	0.95	0.56	321.0	0.0017	14b: yellow
Cyearly($K_2 = 1$)	203.0	10.863 ± 0.022	10.863 ± 0.022	-0.137	6.2	-2.6	203.0	0.013	14b: cyan
Signal $S_{11,y6} : \cong 49.0 \times P_M$									
Rmonthly($K_2 = 1$)	273.8	11.806 ± 0.012	49.028 ± 0.050	0.028	0.56	0.65	1137	0.00057	14c: red
Rmonthly($K_2 = 2$)	273.8	11.770 ± 0.011	48.879 ± 0.046	-0.121	2.6	-2.8	1137	0.0025	14c: blue
Cmonthly($K_2 = 1$)	204.8	11.863 ± 0.021	49.265 ± 0.087	0.265	3.0	4.6	850	0.0054	14c: green
Ryearly($K_2 = 1$)	321.0	11.820 ± 0.027	49.09 ± 0.11	0.09	0.82	2.4	1333	0.0018	14c: yellow
Cyearly($K_2 = 1$)	203.0	11.856 ± 0.068	49.24 ± 0.28	0.24	0.86	4.1	843	0.0049	14c: cyan
Signal $S_{11,y86} : \cong 1.0 \times P_J$									
Rmonthly($K_2 = 1$)	273.8	11.806 ± 0.012	0.9953 ± 0.0010	-0.0047	4.7	-0.11	23	0.0047	14d: red
Rmonthly($K_2 = 2$)	273.8	11.770 ± 0.011	0.99224 ± 0.00093	-0.0078	8.3	-0.18	23	0.0078	14d: blue
Cmonthly($K_2 = 1$)	204.8	11.863 ± 0.021	1.0001 ± 0.0018	0.00010	0.056	0.0017	17	0.00010	14d: green
Ryearly($K_2 = 1$)	321.0	11.820 ± 0.027	0.9964 ± 0.0023	-0.0036	1.6	-0.098	27	0.0036	14d: yellow
Cyearly($K_2 = 1$)	203.0	11.856 ± 0.068	0.9995 ± 0.0057	-0.00050	0.088	-0.0086	17	0.00050	14d: cyan
Signal $S_{53y} : \cong 4.5 \times P_J$									
Rmonthly($K_2 = 1$)	273.8	52.66 ± 0.27	4.439 ± 0.023	-0.061	2.6	-0.32	23	0.014	None
Ryearly($K_2 = 1$)	321.0	53.83 ± 0.76	4.538 ± 0.064	0.038	0.59	0.23	27	0.0084	None
Signal $S_{66y} : \cong 5.5 \times P_J$									
Ryearly($K_2 = 1$)	321.0	66.7 ± 1.4	5.62 ± 0.12	0.12	1.0	0.57	27	0.021	None

maximum epoch ($t_{\min,1}$) of all S_{8y} , $S_{8.y4}$, S_{10y} , $S_{10.y6}$, S_{11y} , $S_{11.y86}$, S_{53y} , S_{66y} and S_{110y} signals are given in Table 15. The units of these three parameters are Earth years.

We are accustomed to measuring time and periodicity in Earth years. The Earth year signal periods detected in all data samples are transformed into Mercury, Venus and Jupiter year signal periods in Tables 15 and 16. It is easier to identify integer multiple periods from these values. The known planet period P_{Planet} in Earth years is used to compute four dimensionless parameters \mathcal{P} , $\sigma_{\mathcal{P}}$, $\Delta\mathcal{P}$ and $\Delta\mathcal{P}_{\text{rel}}$ (Equations 44 -47).

For any detected period $P \pm \sigma_{\mathcal{P}}$, the rounds error is $\sigma_{\mathcal{P}} \propto \sigma_{\mathcal{P}}/P_{\text{Planet}}$. This rounds error $\sigma_{\mathcal{P}}$ is larger for the inner planets Mercury and Venus having having $P_{\text{Planet}} < P_E = 1$, and smaller for Jupiter having $P_{\text{Planet}} > P_E = 1$. For example, the period $P = 8.1087 \pm 0.0076$ gives the following $\sigma_{\mathcal{P}} = 0.032$ (Mercury), $\sigma_{\mathcal{P}} = 0.012$ (Venus), $\sigma_{\mathcal{P}} = 0.0076$ (Earth) and $\sigma_{\mathcal{P}} = 0.000064$ (Jupiter) rounds error values (Table 15: R_{monthly}, $K_2 = 1$ model, signal S_{8y}). This means that the period of Jupiter is easiest to identify from the \mathcal{P} rounds values. On the other hand, the identifications of Mercury and Venus from the \mathcal{P} rounds values are the most difficult ones, and especially in this order. Furthermore, the correct \mathcal{P}_0 rounds value becomes uncertain, if the round error $\sigma_{\mathcal{P}}$ exceeds 1/2, i.e. half a revolution around the Sun. This complication effect is strongest for the longest detected periods P , which have the largest $\sigma_{\mathcal{P}}$ errors in Tables 15 and 16.

The larger rounds error $\sigma_{\mathcal{P}}$ values of Mercury and Venus cause another effect that makes the identification of their signals even more difficult. If the rounds deviation $\Delta\mathcal{P}$ values are drawn from a Gaussian distribution having a mean \mathcal{P}_0 and a standard deviation $\sigma_{\mathcal{P}}$, the probability

$$P(|\Delta\mathcal{P}| \geq |\Delta\mathcal{P}'|) \quad (50)$$

for $|\Delta\mathcal{P}|$ exceeding any fixed large rounds deviation $|\Delta\mathcal{P}'|$ value increases for larger rounds error $\sigma_{\mathcal{P}}$ values. In other words, large $|\Delta\mathcal{P}|$ values are more probable for Mercury and Venus than for the Earth and Jupiter. This increases the probability of stronger mean anomaly migration ΔM for Mercury and Venus (see Equation 54).

The primary minima and the primary maxima of the signals in Table 15 occur at multiples

$$T_{\min,k} = t_{\min,1} + kP \quad (51)$$

$$T_{\max,k} = t_{\max,1} + kP, \quad (52)$$

where $k = 1, 2, \dots$ are integers. The units of P , $t_{\min,1}$ and $t_{\max,1}$ are Earth years. The relation $P = (\mathcal{P}_0 + \Delta\mathcal{P})P_{\text{Planet}}$ gives

$$T_{\min,k} = t_{\min,1} + kP = t_{\min,1} + k(\mathcal{P}_0 + \Delta\mathcal{P})P_{\text{Planet}} = t_{\min,1} + k\mathcal{P}_0P_{\text{Planet}} + k\Delta\mathcal{P}P_{\text{Planet}}$$

$$T_{\max,k} = t_{\max,1} + kP = t_{\max,1} + k(\mathcal{P}_0 + \Delta\mathcal{P})P_{\text{Planet}} = t_{\max,1} + k\mathcal{P}_0P_{\text{Planet}} + k\Delta\mathcal{P}P_{\text{Planet}}$$

The last term

$$\Delta t = k\Delta\mathcal{P}P_{\text{Planet}} \quad (53)$$

is the time difference between the multiples $t_{\min,1} + kP$ and $t_{\min,1} + k\mathcal{P}_0P_{\text{Planet}}$, and between the multiples $t_{\max,1} + kP$ and $t_{\max,1} + k\mathcal{P}_0P_{\text{Planet}}$.

The data time span ΔT contains $\Delta T/P$ multiples of P . Using $k = \Delta T/P$ in Equation 53 gives

$$\Delta t = \frac{\Delta\mathcal{P}\Delta T}{P}P_{\text{Planet}}$$

time difference during ΔT . We convert time difference Δt into planet “mean anomaly migration”

$$\Delta M = \frac{\Delta t}{P_{\text{Planet}}} \times 360^\circ = \frac{\Delta\mathcal{P}\Delta T}{P} \times 360^\circ, \quad (54)$$

where the units of ΔM are degrees. For all ΔT and P combinations, this relation shows that larger mean anomaly ΔM migration occurs for larger $\Delta\mathcal{P}$ values, which are most probable for Mercury and Venus (Equation 50). The “relative mean anomaly migration” during each P_{Planet} revolution is

$$\Delta M_{\text{rel}} = |\Delta M| / \left(\frac{\Delta T}{P_{\text{Planet}}} \right) \times 360^\circ = |\Delta\mathcal{P}| \frac{P_{\text{Planet}}}{P} \times 360^\circ. \quad (55)$$

For any particular signal, the period P detected in each sample determines the linear mean anomaly migration ΔM during the ΔT time span of the data (Equation 54). The slope of this linear $M(t)$ mean anomaly migration is $(\Delta\mathcal{P}/P) \times 360^\circ$ (Equation 54). Let us assume that these mean anomaly migration lines

$$\frac{\Delta\mathcal{P}}{P} (t - t_C) \times 360^\circ = M(t) - M_C \quad (56)$$

of different samples intersect close to a “convergence point” (t_C, M_C) . This means that the mean anomaly value of each line is $M(t) \approx M_C$ at epoch $t = t_C$. The slope of all these $M(t)$ lines approaches zero, if $\Delta\mathcal{P} \rightarrow 0 \equiv \mathcal{P} \rightarrow \mathcal{P}_0 \equiv P \rightarrow P_{\text{planet}}$. In this case, all lines fulfil

$$M(t) \approx M_C \quad (57)$$

for all t values. If the mean anomaly $M(t)$ lines for the same signal are detected in different samples, and these lines show a convergence point (t_C, M_C) , then the periods P , the minimum epochs $t_{\min,1}$ and the maximum epochs $t_{\max,1}$ of all these signals can be connected to each other. The presence of this convergence point confirms that the individual signals detected in different samples can represent the same real signal having the same period, and the same phase. The statistical fluctuation of $|\Delta\mathcal{P}|$ rounds deviations (Equation 50) complicate the detection of this “convergence point connection”. We have already shown that the probability for larger $|\Delta\mathcal{P}|$ values increases when $\sigma_{\mathcal{P}}$ increases for smaller P_{Planet} periods. These $|\Delta\mathcal{P}|$ fluctuations are largest for Mercury and Venus. Therefore, the mean anomaly migration ΔM lines of these inner planets are “messier”, and their convergence point locations are more difficult to detect. Hence, the detection of Jupiter and the Earth from the *same* sunspot data is easier than the detection of Venus and Mercury.

The relations of Equations 54 - 57 are formulated for the mean anomaly M , because this parameter has a linear connection to time. We compute the true anomaly ν_{\min} and ν_{\max} values from the mean anomaly values M for the minimum epochs $t_{\min,1}$ and the maximum epochs $t_{\max,1}$ (Equations 51 and 52) given in Table 15. The mean anomaly M and the true anomaly ν value differences are small for Venus, the Earth and Jupiter, which have nearly circular orbits. The large Mercury’s orbit eccentricity $e = 0.20$ can cause clear ν deviations from the linear M trend (e.g. Figure 14c).

We search for signatures of Mercury, Venus, the Earth and Jupiter from the S_{8y} , $S_{8,y4}$, S_{10y} , $S_{10,y6}$, S_{11y} , $S_{11,y86}$, S_{53y} , S_{66y} and S_{110y} signals. The results for this “wide search” of 36 alternatives are given in Table 15. We summarise the most promising planetary signal candidate detections in Table 16. The three double sinusoid signals “ $2\times$ ” are given in Table 15. We exclude these double sinusoids from Table 16, because the minor asymmetries of these double sinusoid $2 \times P$ period curves can mislead the identification of convergence points (Equation 56).

In our next figures, we plot the ν_{\min} and ν_{\max} values for numerous sample, signal and planet combinations. In every figure, we use the same symbol colour for the signals detected in the same sample. All samples end in the same year 2022, but they begin at different years between 1700 and 1815. This complicates the detection of convergence points, if they are located outside some

sample(s). We solve this problem by computing the ν_{\min} and ν_{\max} values of all samples for the whole time interval between the years 1700 and 2022. The symbols for the ν_{\min} and ν_{\max} values *inside* each sample are highlighted with a black circle around the coloured symbol. This black circle is missing from the symbols representing ν_{\min} and ν_{\max} values *outside* each sample. We can use these outside values to check, if the signals detected in each sample can predict the presence of a convergence point before the beginning of this sample.

The detected signals are the $h_i(t)$ functions (Equation 7) in the sum $h(t)$ of all signals (Equation 6). For the symmetric pure sine model $h_i(t)$ functions, the separation between the primary minimum epoch $t_{\min,1}$ and the primary maximum epoch $t_{\max,1}$ is exactly $P/2$. If the period of the detected signal P is an *even* multiple of the planet's period P_{Planet} , the mean anomaly M values are equal at all minima $T_{\min,k}$ and maxima $T_{\max,k}$ (Equations 51 and 52). Except for the possible deviations caused by the planetary orbit eccentricity, the ν_{\min} and ν_{\max} values will also be equal. This “overlapping effect” occurs in Figures 13b, 13d and 14a. If the detected period P is an *uneven* P_{Planet} multiple, the differences between the mean anomaly M values of all minima $T_{\min,k}$ and maxima $T_{\max,k}$ are equal to 180 degrees. The planetary orbit eccentricity can, again, cause deviations from this 180 degrees difference between the true anomalies ν_{\min} and ν_{\max} . This 180 degrees “separation effect” occurs in Figures 13a, 14b, 14c and 14d. The asymmetries of double wave models can also cause deviations from the overlapping effect and 180 degrees separation effect, like those seen in the blue circles of Figures 13b, 14a, 14b and 14d.

A.1. Signal S_{8v}

The shortest period S_{8v} signal is close to $13 \times P_V$ and $8 \times P_E$ (Tables 15 and 16). The known period ratio is $8 \times P_E/P_V = 13.0039$. Due to statistical $\Delta\mathcal{P}$ fluctuations (Equations 50 and 54), the true anomaly migration curves of Venus in Figure 13a should appear less regular than those of Earth in Figure 13b. This is indeed the case.

A.1.1. Signal $S_{8v} \cong 13 \times P_V$

The two rounds $\mathcal{P} = 13.018 \pm 0.028$ and 13.012 ± 0.094 values for the **Cmonthly** and **Cyearly** samples differ $\Delta\mathcal{P}_{\text{rel}} = 0.90$ and 0.13 from $13 \times P_V$ (Table 16: Signal S_{8v}). The mean anomaly migration is $\Delta M/360^\circ = 0.46$ and 0.30 revolutions during 205 and 203 years, respectively. The green and cyan circles highlighted with black circles show this weak positive upwards ν_{\min} and ν_{\max} true anomaly migration of Venus inside these **Cmonthly** and **Cyearly** samples (Figure 13a).

The other two rounds values for sample **Rmonthly** (pure sine and double wave models) are $\mathcal{P} = 13.180 \pm 0.012$ and 13.279 ± 0.023 . They differ $\Delta\mathcal{P}_{\text{rel}} = 15.0$ and 12.1 from $13 \times P_V$ (Table 16: Signal S_{8v}). For these two \mathcal{P} rounds values, the strong positive upwards mean anomaly migration $\Delta M/360^\circ$ is 6.1 and 9.4 revolutions during 274 years $\equiv 445$ Venus revolutions. These values are equal to the relative mean anomaly migration $\Delta M_{\text{rel}}/360^\circ = 0.014$ and 0.021 during one revolution of Venus. We show the respective true anomaly ν_{\min} and ν_{\max} migration in Figure 13a (red and blue circles).

The uneven $13 \times P_V$ multiple causes the 180 degree separation effect of ν_{\min} and ν_{\max} . The migration lines of large circles denoting the ν_{\max} values show a convergence point (Equation 56), which is highlighted with a large dotted blue circle at $t_C = 1820$ years and $\nu_C = 315$ degrees. The migration lines of smaller circles denoting the ν_{\min} values converge at $t_C = 1820$ years and $\nu_C = 135$ degrees in the centre of the red large dotted circle. These two convergence points are at the beginning of **Cmonthly** and **Cyearly** samples, where the black circles begin to highlight the green and cyan circles. The detection of the two convergence points confirms that all four S_{8v} signals in Table 16 can be connected, regardless of the large true anomaly ν migration of the

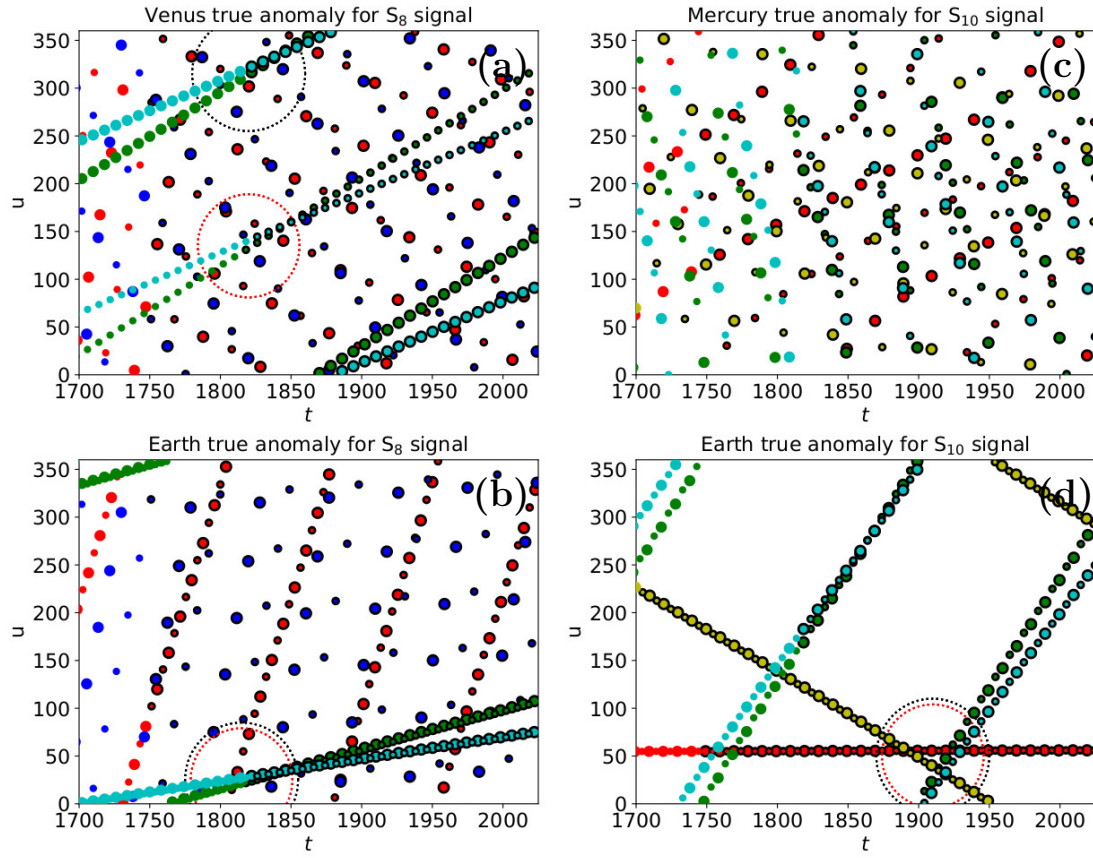


Figure 13. True anomalies ν_{\min} (small circles) and ν_{\max} (large circles) for time point multiples $T_{\min,k}$ and $T_{\max,k}$ (Equations 51 and 52). We compute these multiples from periods (P), primary minimum epochs ($t_{\min,1}$) and primary maximum epochs ($t_{\max,1}$) given in Table 15. Symbol colours for different samples are red (Rmonthly : pure sines), blue (Rmonthly : double waves), green (Cmonthly : pure sines), yellow (Yearly : pure sines), and cyan (Cyearly : pure sines). Symbols for ν_{\min} and ν_{\max} values inside each sample are highlighted with a black circle. (a) Venus' true anomalies for signal S_{8y} . (b) Earth's true anomalies for signal S_{8y} . (c) Mercury's true anomalies for signal S_{10y} . (d) Earth's true anomalies for signal S_{10y} . Units of X-axis and Y-axis are years and degrees, respectively.

two signals detected in Rmonthly (pure sine and double wave models). The apparently messy migration of red and blue circles in Figure 13a can arise, as expected, from the statistical $\Delta\mathcal{P}$ fluctuations caused by the short orbital period of Venus (Equation 50).

A.1.2. Signal $S_{8y} \cong 8 \times P_E$

The two $P \pm \sigma_P = 8.009 \pm 0.017$ and 8.005 ± 0.058 Earth year periods detected in the Cmonthly and Cyearly samples are equal to $8 \times P_E$ comfortably within $\pm 1\sigma_P$ (Table 16: Signal S_{8y}). The mean anomaly migration $\Delta M/360^\circ$ is only 0.23 and 0.13 revolutions in over two centuries (Figure 13b: green and cyan highlighted circles).

For the other two periods (Rmonthly : pure sine and double wave models), the rounds values $\mathcal{P} = 8.1087 \pm 0.0076$ and 8.169 ± 0.014 differ $\Delta\mathcal{P}_{\text{rel}} = 14.3$ and 12.1 from $8 \times P_E$ (Table 16: Signal S_{8y}). The respective ΔM_{rel} relative mean anomaly migration values are 0.013 and 0.021 during one revolution of Earth. Hence, these true anomaly ν_{\min} and ν_{\max} values of Earth migrate about 3.7 and 5.7 revolutions during 274 years (Figure 13b: red and blue highlighted circles).

For the three symmetric pure sine models, the true anomaly ν_{\min} and ν_{\max} lines show the overlapping effect, because $8 \times P_E$ in an even number multiple (Figure 13b: red, green and cyan symbols). Due to the asymmetric signal S_{8y} shape of the double wave model for sample **Rmonthly**, the lines of small and large blue circles do not overlap.

The true anomaly ν_{\min} and ν_{\max} migration curves of Earth converge in the centre of the blue and red dotted circles at $t_C = 1815$ years and $\nu = 25$ degrees (Figure 13b). Due to the aforementioned double wave signal asymmetry, the line of large blue circles deviates from the converging line of small blue circles. Although the convergence point is *outside* samples **Cmonthly** and **Cyearly**, it is nicely covered by the “predictive” green and cyan symbols not highlighted with black circles. We can identify this convergence point regardless of the large true anomaly migration of the pure sine model and the double wave model for sample **Rmonthly**. This means that all four S_{8y} signals’ period (P), primary minimum ($t_{\min,1}$) and primary maximum ($t_{\max,1}$) values for different samples in Table 15 can be connected to the same signal.

We detect the convergence points for the signal candidates of both Venus and the Earth. This indicates that the repetitive relative motions of these two planets may cause this S_{8y} signal.

A.2. Signal $S_{8,y4} \cong 35 \times P_M$

This sixth-strongest signal is detected only in sample **Ryearly** (Table 16: Signal $S_{8,y4}$). The rounds value $\mathcal{P} = 35.158 \pm 0.066$ deviates $\Delta\mathcal{P}_{\text{rel}} = 2.4$ from $35 \times P_M$. We want to draw attention to this $S_{8,y4}$ signal, because the $\mathcal{P} = 69.57 \pm 0.11$ rounds value of another signal, the double sinusoid signal for sample **Rmonthly** ($K_2 = 2$), is quite close to $2 \times 35 \times P_M$ (Table 15: Signal $S_{8,y4}$). We show no figure for this $S_{8,y4}$ signal candidate of Mercury, because one migration line can not have a convergence point.

A.3. Signal S_{10y}

The second-strongest signal S_{10y} period is approximately $41.5 \times P_M$ and $10 \times P_E$. The known ratio is $10 \times P_E/P_M = 45.528$. Considering the statistical $|\Delta\mathcal{P}|$ fluctuations (Equations 50 and 54), the expected migration curves of Mercury should be much messier than those of the Earth. These expectations are “amply rewarded” when Figures 13c and 13d are compared.

A.3.1. Signal $S_{10y} \cong 41.5 \times P_M$

For clarity, as well as to avoid possible misunderstandings, we define \mathcal{P}_0 in Equation 46 as the integer closest to \mathcal{P} . The combined tidal forces of two planets are strongest when they are aligned to the same line with respect to the Sun. This can happen when these planets are at the same side, or at opposite sides, of the Sun. Therefore, the connection $\mathcal{P}_0 \cong 41.5 \times P_M$ draws our attention.

The true anomaly ν_{\min} and ν_{\max} migration curves for Mercury appear truly messy (Figure 13c). These true anomaly migration curves are not fully linear due to the large eccentricity of Mercury’s orbit. However, the reason for the messy impression is not eccentricity or strong migration, because even the largest relative mean anomaly migration is only $\Delta M_{\text{rel}} = 6.2$ revolutions in a total of 851 revolutions during over two centuries (Table 16: Sample **Cmonthly**). The $41.5 \times P_M$ value divides all ν_{\min} and ν_{\max} true anomaly curves into two parts. First part contains uneven multiples of $41.5 \times P_M$ revolutions, and the second part contains even multiples of $83 = 2 \times 41.5 \times P_M$ revolutions. The true anomaly difference between these two parts is about half a revolution. This division effect causes the messy impression in Figure 13c. It would make no sense to search for a convergence point (Equation 56) from this mixture of true anomaly lines.

For one sample **Cmonthly**, this planetary signal candidate can be questioned, because the rounds $\mathcal{P} = 41.802 \pm 0.032$ value having $\Delta\mathcal{P}_{\text{rel}} = 9.4$ differs strongly from $41.5 \times P_M$ (Table 16: Signal S_{10y}). However, the relative rounds deviation values for the other three samples, $0.85 \leq \Delta\mathcal{P}_{\text{rel}} \leq 2.4$, support the $41.5 \times P_M$ relation. The signal detection $\mathcal{P} = 41.529 \pm 0.034$ for sample **Rmonthly** is extremely accurate, only $\Delta M_{\text{rel}} = 0.00070$ during one revolution of Mercury. The mean anomaly migration of the respective highlighted red circles is only 0.79 revolutions during 1137 revolutions (Figure 13c).

A.3.2. Signal $S_{10y} \cong 10 \times P_E$

The relative rounds deviation $\Delta\mathcal{P}_{\text{rel}} = 0.012, 1.5$ and 2.3 values of three samples support the $10 \times P_E$ relation for S_{10y} signal (Table 16: **Rmonthly**, **Ryearly**, **Cyearly**). For the fourth sample **Cmonthly**, the rounds $\mathcal{P} = 10.0659 \pm 0.0077$ value has a large relative rounds deviation $\Delta\mathcal{P}_{\text{rel}} = 8.6$. However, the mean anomaly migration $|\Delta M/360^\circ|$ values for all four samples are smaller than 1.3 revolutions during two, or even three, centuries.

The true anomaly ν_{\min} and ν_{\max} migration curves of Earth are exceptionally clear (Figure 13d). The lines of small and large circles of every sample show the overlapping effect caused by the even number $10 \times P_E$ multiple. This overlapping effect is even more pronounced than in Figure 13b, because the results for all four samples are based on pure sine models. The true anomaly ν_{\min} and ν_{\max} migration convergence point of all four signals is at $t_C = 1910$ years and $\nu \approx M_C = 50$ degrees (Figure 13d: centre of blue and red dotted circles). This convergence point is *inside* all four samples. All these four S_{10y} signals in different samples can undoubtedly originate from one and the same signal.

A.4. Signal $S_{10,y6} \cong 44 \times P_M$

The signal $S_{10,y6}$ period is close to $44 \times P_M = 10.595$ years. The identification of the convergence point of this signal is quite complicated. It is not easy to perceive the correct true anomaly migration directions of the signals detected in three different samples (Figure 14a). The mean anomaly migration values $\Delta M/360^\circ = -2.8, -5.9$ and 7.8 reveal that the red and the blue circles migrate downwards, and the yellow circles migrate upwards (Table 16, Signal $S_{10,y6}$). The large and small circles of each sample show the overlapping effect, because this signal is an even number multiple $44 \times P_M$. The red and yellow circles of the symmetric pure sine model for samples **Rmonthly** and **Ryearly** follow this regularity. However, the blue small circles for the asymmetric double wave model of sample **Rmonthly** break this regularity. Using all the above-mentioned information, we identify the convergence points of both ν_{\min} and ν_{\max} true anomalies at $t_C = 1855$ years and $\nu \approx M_C = 255$ degrees (Figure 14a: centre of blue and red dotted lines). Due to the strong migration, the same pattern is repeated at the approximate year and degree coordinates (1760,220) and (1940,280).

The rounds values $\mathcal{P} = 43.891 \pm 0.083$ and 44.26 ± 0.13 differ only $\Delta\mathcal{P}_{\text{rel}} = 1.3$ and 2.0 from $44 \times P_M$ (Table 16: Signal $S_{10,y6}$). The $\mathcal{P} = 43.774 \pm 0.0824$ value for sample **Rmonthly** double wave model has a large $\Delta\mathcal{P}_{\text{rel}} = 9.0$ relative rounds deviation. However, all three relative mean anomaly migration ΔM_{rel} values $0.0025, 0.0052$ and 0.0059 are nearly the same.

A.5. Signal $S_{11y} \cong 11 \times P_E$

This strongest S_{11y} signal is close to $11 \times P_E$. The non-weighted DCM analysis gives the rounds values $\mathcal{P} = 11.0033 \pm 0.0064, 10.9878 \pm 0.0051$ and 10.981 ± 0.021 (Table 16: **Rmonthly**, **Ryearly**). The respective relative rounds deviation $\Delta\mathcal{P}_{\text{rel}} = 0.52, 0.24$ and 0.95 values support the $11 \times P_E$

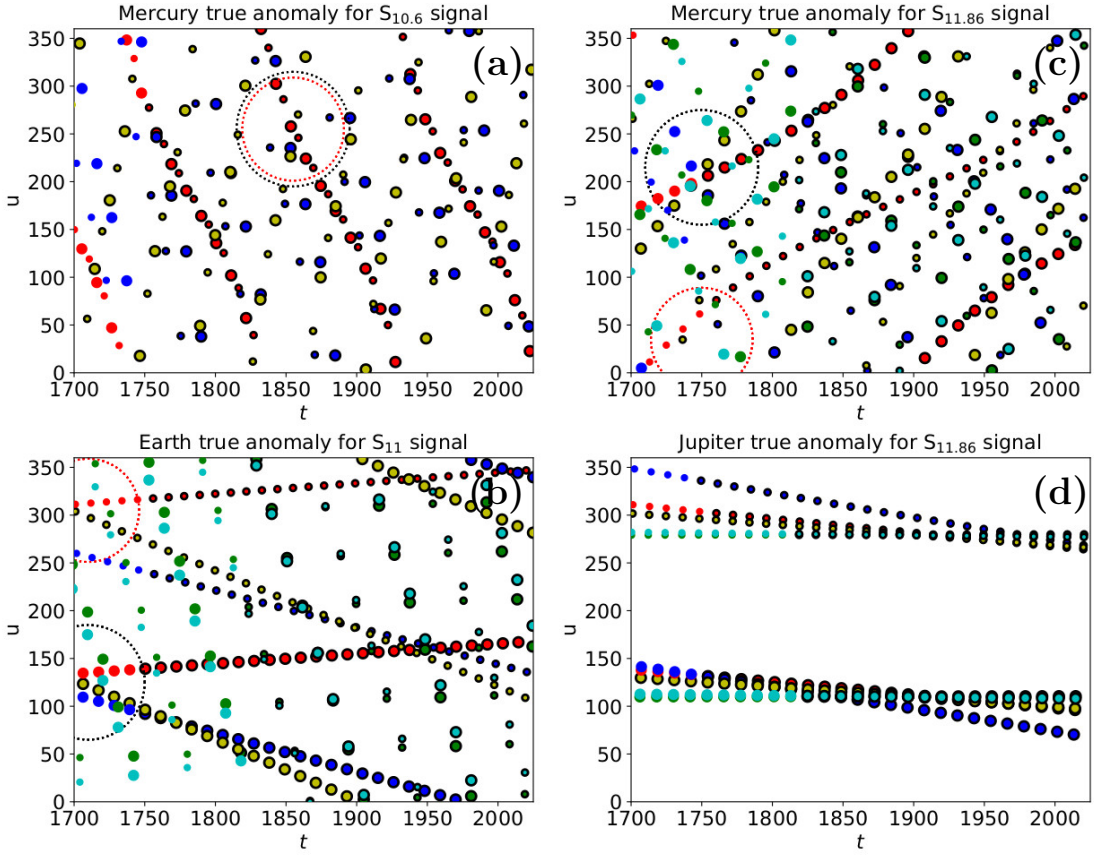


Figure 14. (a) Mercury's true anomalies for signal $S_{10.6}$. (b) Earth's true anomalies for signal S_{11y} . (c) Mercury's true anomalies for signal $S_{11.86}$. (d) Jupiter's true anomalies for signal $S_{11.86}$. Otherwise as in Figure 13.

relation. The rounds values $\mathcal{P} = 10.8585 \pm 0.0048$ and 10.863 ± 0.022 obtained from the weighted DCM analysis, however, show large $\Delta\mathcal{P}_{\text{rel}} = 29$ and 6.2 relative rounds deviations (Table 16: $\text{C}_{\text{monthly}}$, C_{yearly}).

The uneven $11 \times P_E$ multiple causes the 180 degrees separation effect of the ν_{\min} and ν_{\max} true anomalies. Regardless of the above-mentioned large $\Delta\mathcal{P}_{\text{rel}}$ values for samples $\text{C}_{\text{monthly}}$ and C_{yearly} , we obtain very convincing estimates for the convergence points of the true anomaly ν_{\min} and ν_{\max} migration curves (Figure 14b). The maxima converge at $t_C = 1710$ years and $\nu \approx M_C = 125$ degrees. Only the highlighted yellow circles of R_{yearly} reach this convergence point, because it is *outside* samples $\text{R}_{\text{monthly}}$, $\text{C}_{\text{monthly}}$ and C_{yearly} . Yet, the large “predictive” red, blue, green and cyan circles migrate through the large dotted blue circle surrounding this convergence point (Figure 14b). The small circles show that the minima ν_{\min} converge at $t_C = 1710$ and $\nu \approx M_C = 305$ degrees. The small blue circles denoting the asymmetric $\text{R}_{\text{monthly}}$ double wave model, represents the only migration curve that deviates from this convergence point. Both convergence points in the year 1710 are located about 50 years before the beginning of $\text{R}_{\text{monthly}}$ and $\text{C}_{\text{monthly}}$ samples (the highlighted red and blue circles) and about 100 years before the beginning of $\text{C}_{\text{monthly}}$ and C_{yearly} samples (the highlighted green and cyan circles). The successful convergence of the “predictive” red, blue, green and cyan circles (not highlighted with black circles) indicates that all five detected S_{11y} signals can represent one and the same real signal.

A.6. Signal $S_{11,y86}$

The $S_{11,y86}$ signal period is close to $49.0 \times P_M$ and $1.0 \times P_J$. The known period ratio is $P_J/P_M = 49.2608$. This pair of $S_{11,y86}$ signal multiples displays the most dramatic statistical $|\Delta\mathcal{P}|$ fluctuation effect (Equations 50 and 54). The messy Mercury's migration curves (Figure 14c) have exceptionally regular Jupiter's migration curve counterparts (Figure 14d).

A.6.1. Signal $S_{11,y86} \cong 49.0 \times P_M$

None of the five \mathcal{P} rounds values differs more than $3\Delta\mathcal{P}_{\text{rel}}$ from $49.0 \times P_M$ (Table 16: Signal $S_{11,y86}$). No other planetary signal candidate shows this degree of regularity. All relative mean anomaly migration values fulfil $\Delta M_{\text{rel}} \leq 0.0054$. For this particular ΔM_{rel} parameter, this is also the best result among all planetary signal candidates. Even the largest mean anomaly migration $\Delta M/360^\circ$ is only 4.6 revolutions during 850 revolutions of Mercury. The smallest mean anomaly migration for sample **Rmonthly** ($K_2 = 1$) is only $\Delta M/360^\circ = 0.65$ during 1137 revolutions. The twisted large and small red circle curves of this sample nicely illustrate Mercury's orbit eccentricity effect (Figure 14c).

The uneven $49 \times P_M$ multiple causes the 180 degrees separation effect of ν_{min} and ν_{max} values (Figure 14c). The red, green, yellow and cyan circles of four samples show positive upwards migration. The blue circles denoting the double wave model results for sample **Rmonthly** show the only negative downwards migration. The curves of the large highlighted red and yellow circles denoting the ν_{max} values *inside* samples **Rmonthly** ($K_2 = 1$) and **Ryearly** intersect at the convergence point $t_C = 1750$ and $\nu \approx M_C = 215$ degrees. The respective large "predictive" blue, green and cyan circle curves, which are *outside* samples **Rmonthly** ($K_2 = 2$), **Cmonthly** and **Cyearly**, also intersect at the centre of the large blue dotted circle surrounding this convergence point. The respective ν_{min} convergence point is at $t_C = 1750$ and $\nu \approx M_C = 35$ degrees. The two detected convergence points indicate that all five $S_{11,y86}$ signals detected in different samples can represent one and the same signal.

A.6.2. Signal $S_{11,y86} \cong 1.0 \times P_J$

Three rounds $\mathcal{P} = 1.0001 \pm 0.0018$, 0.9964 ± 0.0023 and 0.9995 ± 0.0057 values support the $1 \times P_J$ relation (Table 16: Signal $S_{11,y86}$). Two rounds values for **Rmonthly**, $\mathcal{P} = 0.9953 \pm 0.0010$ and 0.99224 ± 0.00093 , differ $\Delta\mathcal{P}_{\text{rel}} = 4.7$ and 8.3 from this relation. However, all mean anomaly migration values fulfil $|\Delta M| \leq 0.18$ revolutions.

The uneven $1 \times P_J$ multiple causes the 180 degree separation effect between Jupiter's true anomaly ν_{min} and ν_{max} values (Figure 14b). All true anomaly migration curves are so regular that there is no need to search for convergence points. The small blue circles, which denote the ν_{min} values of the asymmetric double wave model for sample **Rmonthly**, show the largest deviation from the general migration trends. The regular convergence of Jupiter's true anomalies definitely indicates that one and the same signal is detected in all five different samples. The strongest amplification of the $S_{11,y86}$ sunspot signal occurs close to true anomaly $\nu = \nu_{\text{max}} = 120^\circ$. The damping of this signal occurs about 6 years ($11.86/2$) later, close to true anomaly $\nu = \nu_{\text{min}} = 300^\circ$.

The detection of the convergence points for the signal candidates of Mercury and Jupiter indicates that the relative motions of these two planets can cause this $S_{11,y86}$ signal.

The maxima of all five $S_{11,y86}$ signals in Table 16 occur between Jupiter's perihelion and aphelion, which are denoted with dotted and continuous vertical lines in Figure 15. All $S_{11,y86}$ signal minima are between Jupiter's aphelion and perihelion. The phases of all five $S_{11,y86}$ signals are

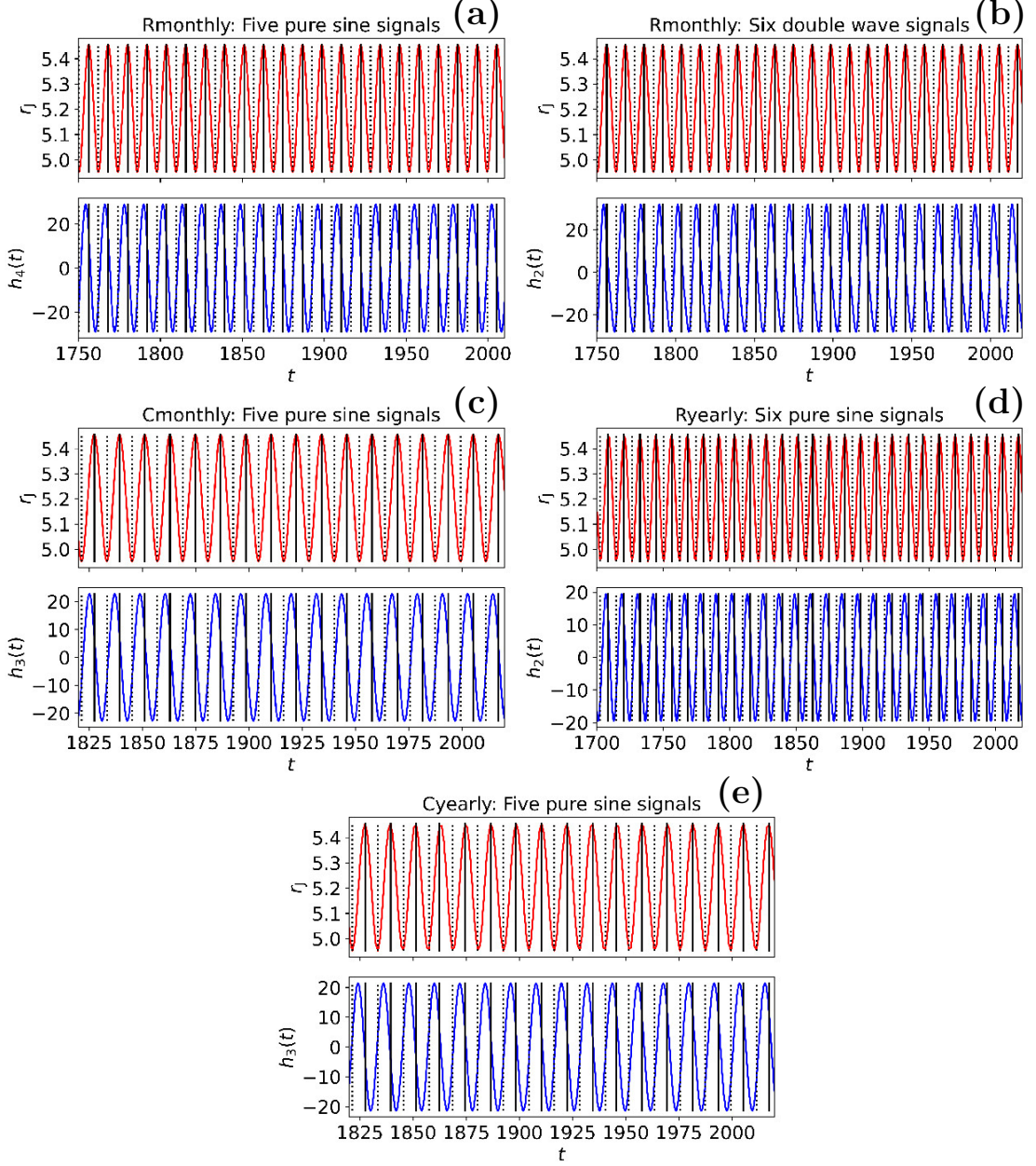


Figure 15. Signal S11,y86 connection to Jupiter's distance r_J from the Sun. (a) Upper panel: Red curve shows distance between the Sun and Jupiter. Aphelion and perihelion epochs are denoted with vertical black continuous and dotted lines, respectively. Units are x-axis $[t]$ = years and y-axis $[r_J]$ = AU. Lower panel: Blue curve shows simultaneous $h_4(t)$ pure sine 11.807 year signal in Rmonthly (DCM-manual: Table 7). Aphelion and perihelion notations are as in upper panel. Units are x-axis $[t]$ = years and y-axis $[h_4(t)]$ = dimensionless. (b) $h_2(t)$ double wave 11.770 year signal in Rmonthly (DCM-manual: Table 9). Otherwise as in “a”. (c) $h_3(t)$ pure sine 11.863 year signal in Cmonthly (DCM-manual: Table 11). Otherwise as in “a”. (d) $h_2(t)$ pure sine 11.826 year signal in Ryearly (DCM-manual: Table 15). Otherwise as in “a”. (e) $h_3(t)$ pure sine 11.856 year signal in Cyearly (DCM-manual: Table 17). Otherwise as in “a”.

stable, and stay in phase with Jupiter's orbital motion. The signal amplitudes in the monthly and the yearly samples are nearly the same. This $S_{11,y86}$ signal is clearly connected to the orbital motion of Jupiter. The distance between the Sun and Jupiter modulates the number of sunspots.

All these results confirm an irrefutable deterministic connection between the sunspot cycle and Jupiter's orbital motion. If these results do not represent the *direct* detection of Jupiter from the sunspot data, then, what have we detected? It would be quite a coincidence if we had managed to formulate a flawed statistical method that would accidentally detect Jupiter's period from the sunspot data. We can ask, quite rightly, has anyone else ever made this kind of a direct detection of Jupiter from the sunspot data?

A.7. Signal $S_{53y} \cong 4.5P_J$

The two rounds $\mathcal{P} = 4.439 \pm 0.023$ and 4.538 ± 0.064 differ only $\Delta\mathcal{P}_{\text{rel}} = 2.6$ and 0.59 from $4.5 \times P_J$ (Table 16: S_{53y}). We merely mention this regularity, but we do not search for converge points from the migration of only two curves.

A.8. Signal $S_{66y} \cong 5.5 \times P_J$ or $\cong 6.0 \times P_J$

This weakest one of all detected signals has a rounds value $\mathcal{P} = 5.62 \pm 0.12$ (Table 16: Signal S_{66y}). We mention this S_{66y} signal because the double sinusoid signal period $P = 143.30 \pm 0.99$ (Table 15: Signal S_{66y}) has a rounds value $\mathcal{P} = 12.088 \pm 0.083$, which is close to $2 \times 6 \times P_J$.

Acknowledgements We thank the Finnish Computing Competence Infrastructure (FCCI) for supporting this project with computational resources. We thank Juha Helin, Jani Jaakkola, Sami Maisala and Pasi Vettentranta who helped us utilise parallel computation resources in the High Performance Computing (HPC) platform. Veijo Niinikoski is acknowledged for pointing out that the Earth's and Jupiter's magnetic fields are much stronger than those of Venus and Mercury. We also thank Stefan Ahmala for drawing our attention to the possible electromagnetic interactions between the magnetic fields of solar system bodies. We thank professor Alexis Finoguenov for his insightful comments, as well as for recommending the use of grammar packages. This work has made use of NASA's Astrophysics Data System (ADS) services.

B. Additional statements

Author Contribution L.J. analysed the data, prepared the figures and the tables, wrote the manuscript, as well as revised the manuscript.

Data Availability All analysed data are stored in Zenodo database <https://zenodo.org/uploads/11503698>.

Code Availability The Zenodo database <https://zenodo.org/uploads/11503698> also supplies our Discrete Chi-square Method (DCM) Python code. Our DCM-manual gives full instructions for repeating the DCM analysis.

Declarations

Conflict of interest The author declares no competing interests.

References

Aguilar, L.M., Robledo-Sánchez, C., Carrasco, M.L., Otero, M.M.: 2012, The principle of superposition for waves: The amplitude and phase modulation phenomena. *Applied Mathematics and Information Sciences* **6**, 307.
 Allen, M.P.: 2004, *Understanding Regression Analysis*, Springer US, 113. ISBN 9780306484339. [URL](#).

Asikainen, T., Mantere, J.: 2023, Prediction of even and odd sunspot cycles. *arXiv e-prints*, arXiv:2309.04208. [DOI](#). [ADS](#).

Babcock, H.W.: 1961, The Topology of the Sun's Magnetic Field and the 22-Year Cycle. *Astrophys. J.* **133**, 572. [DOI](#). [ADS](#).

Bhowmik, P., Jiang, J., Upton, L., Lemerle, A., Nandy, D.: 2023, Physical Models for Solar Cycle Predictions. *Space Sci. Rev.* **219**, 40. [DOI](#). [ADS](#).

Biswas, A., Karak, B.B., Usoskin, I., Weisshaar, E.: 2023, Long-Term Modulation of Solar Cycles. *Space Sci. Rev.* **219**, 19. [DOI](#). [ADS](#).

Borisov, B.: 2012, Three-planet resonances in the Solar system. *Bulgarian Astronomical Journal* **18**, 27. [ADS](#).

Breger, M., Garrido, R., Handler, G., Wood, M.A., Shobbrook, R.R., Bischof, K.M., Rodler, F., Gray, R.O., Stankov, A., Martinez, P., O'Donoghue, D., Szabó, R., Zima, W., Kaye, A.B., Barban, C., Heiter, U.: 2002, 29 frequencies for the δ Scuti variable BI CMi: the 1997-2000 multisite campaigns. *Mon. Not. R. Astron. Soc.* **329**, 531. [DOI](#). [ADS](#).

Charbonneau, P.: 2010, Dynamo Models of the Solar Cycle. *Living Reviews in Solar Physics* **7**, 3. [DOI](#). [ADS](#).

Charbonneau, P.: 2022, External Forcing of the Solar Dynamo. *Frontiers in Astronomy and Space Sciences* **9**, 853676. [DOI](#). [ADS](#).

Cionco, R.G., Kudryavtsev, S.M., Soon, W.W.-H.: 2023, Tidal Forcing on the Sun and the 11-Year Solar-Activity Cycle. *Sol. Phys.* **298**, 70. [DOI](#). [ADS](#).

Draper, N.R., Smith, H.: 1998, *Applied Regression Analysis*, John Wiley & Sons, Inc. [DOI](#).

Efron, B., Tibshirani, R.: 1986, Bootstrap Methods for Standard Errors, Confidence Intervals, and Other Measures of Statistical Accuracy. *Statistical Science* **1**, 54.

Feth, L.L.: 1974, Frequency discrimination of complex periodic tones. *Perception & Psychophysics* **15**, 375.

Gleissberg, W.: 1945, Evidence for a long solar cycle. *The Observatory* **66**, 123. [ADS](#).

Gnevyshev, M.N., Ohl, A.I.: 1948, On the 22-year cycle of solar activity. *Astron. Zh.* **25**, 18.

Hale, G.E., Ellerman, F., Nicholson, S.B., Joy, A.H.: 1919, The Magnetic Polarity of Sun-Spots. *Astrophys. J.* **49**, 153. [DOI](#). [ADS](#).

Handler, G.: 2003, Merging Data from Large and Small Telescopes – Good or Bad? And: How Useful is the Application of Statistical Weights to Time-Series Photometric Measurements? *Baltic Astronomy* **12**, 253. [DOI](#). [ADS](#).

Hantzsche, E.: 1978, On the Tidal Theory of Solar Activity. *Astronomische Nachrichten* **299**, 259. [DOI](#). [ADS](#).

Horne, J.H., Baliunas, S.L.: 1986, A Prescription for Period Analysis of Unevenly Sampled Time Series. *Astrophys. J.* **302**, 757. [DOI](#). [ADS](#).

Javaraiah, J.: 2023, Prediction for the amplitude and second maximum of Solar Cycle 25 and a comparison of the predictions based on strength of polar magnetic field and low-latitude sunspot area. *Mon. Not. R. Astron. Soc.* **520**, 5586. [DOI](#). [ADS](#).

Jayalekshmi, G.L., Pant, T.K., Prince, P.R.: 2022, Sunspot-Cycle Evolution of Major Periodicities of Solar Activity. *Sol. Phys.* **297**, 85. [DOI](#). [ADS](#).

Jetsu, L.: 2020, Discrete Chi-square Method for Detecting Many Signals. *The Open Journal of Astrophysics* **3**, 4. [DOI](#). [ADS](#).

Jetsu, L.: 2021, Say Hello to Algol's New Companion Candidates. *Astrophys. J.* **920**, 137. [DOI](#). [ADS](#).

Jetsu, L., Pelt, J.: 1999, Three stage period analysis and complementary methods. *Astron. Astrophys. Suppl.* **139**, 629. [DOI](#). [ADS](#).

Komitov, B., Kaftan, V.: 2004, The Sunspot Activity in the Last Two Millenia on the Basis of Indirect and Instrumental Indexes: Time Series Models and Their Extrapolations for the 21st Century. In: Stepanov, A.V., Benevolenskaya, E.E., Kosovichev, A.G. (eds.) *Multi-Wavelength Investigations of Solar Activity* **223**, 113. [DOI](#). [ADS](#).

Krasheninnikov, I.V., Chumakov, S.O.: 2023, Predicting the Functional Dependence of the Sunspot Number in the Solar Activity Cycle Based on Elman Artificial Neural Network. *Geomagnetism and Aeronomy* **63**, 215. [DOI](#). [ADS](#).

Lassen, K., Friis-Christensen, E.: 1995, Variability of the solar cycle length during the past five centuries and the apparent association with terrestrial climate. *Journal of Atmospheric and Terrestrial Physics* **57**, 835. [DOI](#). [ADS](#).

Lehtinen, J., Jetsu, L., Hackman, T., Kajatkari, P., Henry, G.W.: 2011, The continuous period search method and its application to the young solar analogue HD 116956. *Astron. Astrophys.* **527**, A136. [DOI](#). [ADS](#).

Leighton, R.B.: 1969, A Magneto-Kinematic Model of the Solar Cycle. *Astrophys. J.* **156**, 1. [DOI](#). [ADS](#).

Loumos, G.L., Deeming, T.J.: 1978, Spurious results from Fourier analysis of data with closely spaced frequencies. *Astrophys. Space Sci.* **56**, 285. [DOI](#). [ADS](#).

Murphy, S.J.: 2012, Kepler Fourier concepts: The performance of the Kepler data pipeline. *Astronomische Nachrichten* **333**, 1057. [DOI](#). [ADS](#).

Ohtomo, N., Terachi, S., Tanaka, Y., Tokiwano, K., Kaneko, N.: 1994, New Method of Time Series Analysis and Its Application to Wolf's Sunspot Number Data. *Japanese Journal of Applied Physics* **33**, 2821. [DOI](#). [ADS](#).

Parker, E.N.: 1955, Hydromagnetic Dynamo Models. *Astrophys. J.* **122**, 293. [DOI](#). [ADS](#).

Petrovay, K.: 2020, Solar cycle prediction. *Living Reviews in Solar Physics* **17**, 2. [DOI](#). [ADS](#).

Reegen, P.: 2007, SigSpec. I. Frequency- and phase-resolved significance in Fourier space. *Astron. Astrophys.* **467**, 1353. [DOI](#). [ADS](#).

Rieger, E., Kanbach, G., Reppin, C., Share, G.H., Forrest, D.J., Chupp, E.L.: 1984, A 154-day periodicity in the occurrence of hard solar flares? *Nature* **312**, 623. [DOI](#). [ADS](#).

Rodríguez, E., Costa, V., Handler, G., García, J.M.: 2003, Simultaneous uvby photometry of the new delta Sct-type variable HD 205. *Astron. Astrophys.* **399**, 253. [DOI](#). [ADS](#).

Rutkowski, L.: 2014, Symmetry and asymmetry as a physical and perceptual feature of the complementary pair of bearing sinusoids. Part I. Amplitude and frequency envelope relations. *Archives of Acoustics* **23**, 51.

Scafetta, N., Bianchini, A.: 2022, The Planetary Theory of Solar Activity Variability: A Review. *Frontiers in Astronomy and Space Sciences* **9**, 937930. [DOI](#). [ADS](#).

Scargle, J.D.: 1982, Studies in astronomical time series analysis. II - Statistical aspects of spectral analysis of unevenly spaced data. *Astrophys. J.* **263**, 835. [DOI](#). [ADS](#).

Schuster, A.: 1911, The Influence of Planets on the Formation of Sun-Spots. *Proceedings of the Royal Society of London Series A* **85**, 309. [DOI](#). [ADS](#).

Schwabe, M.: 1844, Sonnenbeobachtungen im Jahre 1843. Von Herrn Hofrat Schwabe in Dessau. *Astronomische Nachrichten* **21**, 233. [ADS](#).

Schwär, S., Müller, M., Schlecht, S.: 2023, Modifying Partials for Minimum-Roughness Sound Synthesis. In: *Proceedings of Timbre 2023, 3rd International Conference on Timbre, Thessaloniki, Greece*, 1.

Stefani, F., Giesecke, A., Weier, T.: 2019, A Model of a Tidally Synchronized Solar Dynamo. *Sol. Phys.* **294**, 60. [DOI](#). [ADS](#).

Usoskin, I.G., Solanki, S.K., Kovaltsov, G.A.: 2007, Grand minima and maxima of solar activity: new observational constraints. *Astron. Astrophys.* **471**, 301. [DOI](#). [ADS](#).

Van Geel, B., Raspovov, O., Renssen, H., Van der Plicht, J., Dergachev, V., Meijer, H.: 1999, The role of solar forcing upon climate change. *Quaternary Science Reviews* **18**, 331.

Vasil, G., Lecoanet, D., Augustson, K., Burns, K., Oishi, J., Brown, B., Brummell, N., Julien, K.: 2024, The solar dynamo begins near the surface. *Nature* **629**, 769. [DOI](#).

Vaughan, S.: 2005, A simple test for periodic signals in red noise. *Astron. Astrophys.* **431**, 391. [DOI](#). [ADS](#).

Wagner, G., Beer, J., Masarik, J., Muscheler, R., Kubik, P.W., Mende, W., Laj, C., Raisbeck, G.M., Yiou, F.: 2001, Presence of the Solar de Vries Cycle (\sim 205 years) during the Last Ice Age. *Geophys. Res. Lett.* **28**, 303. [DOI](#).

Weisshaar, E., Cameron, R.H., Schüssler, M.: 2023, No evidence for synchronization of the solar cycle by a “clock”. *Astron. Astrophys.* **671**, A87. [DOI](#). [ADS](#).

Wolf, R.: 1852, Bericht über neue Untersuchungen über die Periode der Sonnenflecken und ihrer Bedeutung von Herrn Prof. Wolf. *Astronomische Nachrichten* **35**, 369. [DOI](#). [ADS](#).

Wolf, R.: 1859, Extract of a Letter to Mr. Carrington. *Mon. Not. R. Astron. Soc.* **19**, 85. [DOI](#). [ADS](#).

Zhu, F.R., Jia, H.Y.: 2018, Lomb-Scargle periodogram analysis of the periods around 5.5 year and 11 year in the international sunspot numbers. *Astrophys. Space Sci.* **363**, 138. [DOI](#). [ADS](#).